Optimizing the Detection Limit of Micro Ring Resonators

Master Thesis

Hasib Mustafa

Supervisors
Dr. Ir. F. Schreuder
Dr. Sonia Garcia Blanco

OPTIMIZING THE DETECTION LIMIT OF MICRO RING RESONATORS

By

Hasib Mustafa

A Thesis Submitted to the Graduate

Faculty of The University

in Partial Fulfilment of the

Requirements for the Degree of

MASTER OF SCIENCE

Electrical Engineering

Specialization: Integrated Optical MicroSystem

Approved by the
Examining Committee:

Dr. Ir. F. Schreuder, Thesis Supervisor

Dr. Sonia Garcia Blanco, Thesis Supervisor

Prof. Dr. Jennifer Herek, Thesis Advisor

---

dr.ir. C. G. H. Roeloffzen, Committee Member

---

dr.ir. M. J. Bentum, Committee Member

Universiteit Twente
Drienerlolaan 5, 7522 NB Enschede
The Netherlands

August 28, 2014

The research work disclosed in this publication is partially funded by the European Commission under the Seventh (FP7 - 2007-2013) Framework Programme - BIOMONAR, and a micro and nanotechnology innovation programme of the Dutch Government - NanoNextNL Food Diagnostics.

ABSTRACT

The application of Microring Resonators (MRRs) for lab-on-a-chip and environmental detection is an emerging trend in the chemical industry. Advances in technology enable low-cost, high-throughput, cost- and time-saving benefits; thus, the commercial factors of a certain technology rely on early development work. In the recent years, the feasibility of MRRs for biochemical sensing has been realized. However, it is recommended in the majority of the literature that the minimization of the influence of external factors should be given priority for an increased accuracy of the detection system. Since real time diagnostics requires a real time efficient signal processing of the measured data, statistical signal processing can provide robust, efficient and fast computation over the noisy data with significantly accurate and precise results.

This thesis covers the design and implementation of a detection system aimed to provide high accuracy and precision in detecting the resonance peak wavelength of the MRR. The designed curve-fitting algorithm is implemented within the detection software as a subprogram called peak detection. This incorporates most of the mathematical computations required for determining the resonance peak position. The peak detection is designed by means of nonlinear least squares minimization along with dynamic free spectral range calculation, which is proposed in this thesis.

Measurement instruments are calibrated for detecting the limitations in terms of drift and sensitivity. Two VCSELs are characterized and a cubic polynomial relationship between current and wavelength is proposed. Perturbations from external factors are studied and favourable operating conditions based on minimum perturbations are suggested.

Simulation studies as well as real-time experiments are performed to evaluate the performance of the system. The influence of algorithmic parameters on the fitting algorithm and the efficacy of the detection system with respect to measurand concentration is evaluated. The proposed detection system is found to be an optimized system in terms of accuracy and precision for the resonance peak detection of the MRRs without any increased demand for cost and computation time.

SAMENVATTING

De toepassing van Microring Resonators (MRRs) voor lab-on-a-chip en milieudetectie is een toenemende trend in de chemische industrie. Voortgang in technologie zorgt voor lage kosten, grote doorvoer, kosten- en tijdbesparende voordelen; aldus steunen de commerciële factoren van een bepaalde technologie op eerdere ontwikkelingen. Gedurende de afgelopen jaren is de haalbaarheid van MRRs voor biochemische detectie bewezen. In het merendeel van de literatuur wordt echter aanbevolen de minimalisatie van externe factoren te prioriteren om een grotere nauwkeurigheid van het detectiesysteem te behalen. Aangezien realtime diagnostiek een realtime efficiënte signaalverwerking van de gemeten data vereist, kan statische signaalverwerking voorzien in een robuuste, efficiente en snelle berekening van de ruisbevattende data met beduidend nauwkeurigere en preciezere resultaten.

Dit verslag behelst het ontwerp en de implementatie van een detectiesysteem met als doel te voorzien in grote nauwkeurigheid en precizie bij het detecteren van de resonantie golflengtepiek van de MRR. Het gewenste curve-fitting algoritme is geimplementeerd in de detectiesoftware als een subprogramma, genaamd peak detection. Dit omvat het merendeel van de mathematische berekeningen die nodig zijn om de positie van de resonantiepiek te bepalen. De piekdetectie is ontworpen door middel van niet-lineaire kleinste kwadraten methode gecombineerd met een dynamische free spectral range berekening, welke is voorgesteld in dit verslag.

De meetapparatuur is gekalibreerd om de grenzen van verschuiving en gevoeligheid te detecteren. Twee VCSELs zijn gekarakteriseerd en een kubische polynome relatie tussen stroom en golflengte wordt voorgesteld. Er is gekeken naar de invloed van externe verstoringen en suggesties worden gedaan voor gunstig werkende instellingen welke de effecten van de verstoringen minimaliseren.

Zowel simulatiestudies als realtime experimenten zijn uitgevoerd om het functioneren van het systeem te evalueren. De invloed van algoritmische parameters op de uitkomst van het algoritme en de doeltreffendheid van het detectiesysteem met betrekking tot de concentratie van het monster is geëvalueerd. Het voorgestelde detectiesysteem is een geoptimaliseerd systeem betreffende accuraatheid en precisie voor de bepaling van de resonantiepiek van de MRRs gebleken, zonder toenemende kosten en rekentijd.

Allah is the Light of the heavens and the earth.
The example of His light is like a niche within which is a lamp,
the lamp is within glass,
the glass as if it were a pearly (white) star
lit from (the oil of) a blessed olive tree, neither of the east nor of the west,
whose oil would almost glow even if untouched by fire.
Light upon light.
Allah guides to His light whom He wills.
And Allah presents examples for the people,
and Allah is Knowing of all things.

Al Quran (24:35)

ACKNOWLEDGMENTS

It was a quiet Sunday afternoon when I first came to Enschede. At that time, I didn't know that I was going to experience the biggest paradigm shift in my life, ranging from my day-to-day lifestyle to my very own thought pattern. The last twenty-one months, for me, was a time of intense learning and self-evaluation. A simple interest in photonics turned out to be the biggest challenge in my academic life. Updating my knowledge base of electrons with photons was so hard initially that I had to search for motivation in scriptures, documentaries and literatures. And the more persistent I became, the more sources motivated me. This Master thesis project gave me the opportunity to relate my theoretical knowledge of optics and electronics to the practical applications; as if it brought balance in my master studies on integrated optical microsystem.

In his book *The Alchemist*, Paulo Cohelo wrote, "when you really want something to happen, the whole world conspires to help you achieve it." I found it true and there are so many people I want to thank. To begin with, I would like to thank my company supervisor Dr. Ir. F. Schreuder. Without his patience and guidance, I would have been completely lost during the project. I would like to thank my university supervisor, Dr. Sonia Garcia Blanco for her never ending support and kindness. Without her sincere guidance in writing the thesis, it would not been possible to construct a master thesis report of acceptable quality. I am very much indebted to Dr. H.J.W.M. Hoekstra of IOMS group. He was the mentor for my Master studies till his retirement. I will cherish the discussions and guidance I received from him on data presentation and critical thinking. I would also like to express my gratitude to Dr. Ir. Rene Heideman for giving me the opportunity to carry on my Master thesis at LioniX B.V. I would like to thank Dr. Hans van den Vlekkert for his never ending positive feedbacks and immense support towards the accomplishment of my Master degree. I would like to thank Petra Wicherink and Dr. Ir. Jan Bos for translating the abstract of this thesis in Dutch. I would like to express my sincere gratitude to Dr. Geert A.J. Besselink for the motivations when my moral saw its minima. I would like to thank Jörn Epping of LPNO group for letting me borrow the OSA whenever required. I would like to express my sincere gratitude to Sergio Vázquez-Córdova and Yean-Sheng Yong of OS group for the discussions on back reflection from the chip facet and the automation of the VCSEL characterization process. I would like to thank Erwin Bomert for always being the friend in need.

As always, the biggest sources of my inspiration are my parents. It is solely their unimaginable sacrifices that made it possible for me to reach where I am today. My father's relentless push towards excellence and my mother's never-ending love made my academic achievements feasible. I would like to thank Galib, Meem and Labonno for their consistent mental support. I would like to thank Kabir vai, Suraiya vabi, Reza vai, Rezwan vai, Morshed vai, Rubaiya amma and their little Taiyeba (Tab), Kallol vai, Mahua vabi and their little Kushal (Kabul), Zubair vai, Mahdin vai, Ashif vai, Fatema vabi, Azreen apu, Nabila apu, Siddique, Mahmud, Khaleq, Paul, Jacqueline, Anouk, Guled, Akwa, Naser and Vignesh for being my family in abroad.

Knowledge is a never-ending process, and the physics of light makes me feel stupid everytime I feel like I understood some of its complicacies. Light mesmerizes me. It opens the eyes of an individual, both literally and figuratively, to new dimensions and possibilities. Let there be light for everyone!

Hasib Mustafa
Enschede, May 2014

CONTENTS

LIST OF FIGURES

LIST OF TABLES

1

INTRODUCTION

Recent technology advances are rapidly changing the landscape of early detection and identification. The current trend maintains a gradual shift towards optical sensors, mainly because of their intrinsic qualities of being immune towards electromagnetic interference (EMI), and showing high sensitivity and spectral discrimination. Additionally, optical sensors can be operated in the hazardous environment of industrial plants, since electrical signals are not required in the sensing area[1], thus, performing remote sensing. They can provide multiplexed detection within a single device. Following the significant advancement in microsystems technology, the so-called '*Lab-on-a-chip*'(LOC) devices were blessed, not only with a technology push but also a market pull focusing biomedical diagnostics, industrial process monitoring, healthcare, pharmaceuticals, environmental monitoring and defence. The research over the area of optical sensing is going on for more than 30 years[2]. Over this course of time, the sensor platform evolved almost decennially from optical fibers, towards planar waveguides and, for the last decade, photonic crystals[3].

Integrated optical sensors

The optical sensors with planar waveguiding structure are commonly referred to as *integrated optical* (IO) sensors, and almost all of them exploit evanescent wave sensing. Leveraging from optical telecommunications, integrated optical sensors address the issues that impair the glamour of fiber optic as optical sensor, majority of which emerge from the geometry of the fibres themselves. Fibers possess a mechanical rigidity of 69 GPa[4], and their inclusion as sensor head makes them more fragile and restricts the possibilities of miniaturization. Moreover, inaccessibility towards prompt micropattering techniques and complex processing step for selective sensing makes them a less attractive candidate for optical sensor platforms in general. Integrated optical sensors, on the contrary, offers a large freedom of choice for materials, geometry, micropattering[5] and deposition techniques for the production of the sensitive layer[6]. Interrogation of sensitive material by evanescent field changes an optical parameter of the modal field, depending on which the sensors are classified as either refractive, corresponding to the change of real part of the effective index, or absorptive, corresponding to the change in negative part of the effective index, or luminescent as seen from Fig. 1.1. In refractometric optical sensors, changes in the sensitivities to the measurand, i.e. material composition, concentration, temperature etc., induces a change in refractive index difference between the core and the cladding layer resulting in a different effective index. This change is translated in the output power as a change in phase. Depending on the applied principle, we can further segregate optical sensors broadly in two categories - principles that encompass the effective refractive index change and principles that rely on the mode field properties. In 1983, the world observed the first demonstration of *surface plasmon resonanace* (SPR) sensors for biosensing application[3]. Since then, extensive exploration established it as a very powerful label-free bio-recognition tool. Grating couplers also operates on the same principle as SPR. Both are primarily based on the modal coupling

Refractometric optical sensors

of the guided mode. One of the main limitations of the standard SPR transducer arises from the necessity for moving elements to observe the changes in the reflectance angle[7]. Contrarily, varieties of sensors have been developed exploiting the leaky modes at the waveguide-substrate boundary. Depending on the structural geometry, this kind of sensors includes resonant mirror (RM), metal clad waveguide (MCW), reverse symmetry waveguide (RSW), symmetric metal clad waveguide (SMCW) and bend sensors. This is relatively a new field involving the waveguiding property, thus variant shapes are possible to realize[8,9].

Interferrometric optical sensors

On the other end of this spectrum, there are sensors that employ the change in effective refractive index to transduce the physical signal. All of the sensors in this category root on the interference phenomenon, clear example of which lies in all types of interferometers, such as Mach-Zehnder-, Young-, Michelson-, difference, Zeeman-, Hartman- and backscattering interferometers and in resonators such as Fabry-Perot- and ring-resonators. Interference inherently holds a larger expectancy of high resolution in terms of sensitivity towards measurands and perturbation minimization through balanced structure. Integrated Mach-Zehnder interferometer (MZI) for biosensing was first demonstrated by Heideman et al.[10], where a MZI was created on a silicon substrate with a Si_3N_4 waveguide and gratings were etched for input/output coupling. Primarily, the effective interaction length is determined by the physical dimension of the sensors and to be sensitive enough, the interaction length is quite large. Ring resonators (RR), however, facilitates the whispering gallery mode (WGM) propagation by the total internal reflection of light within its boundary curvature. The operating principle, for the greatest part, remains the same. Yet, the effective light-analyte interaction length of a ring resonator sensor is no longer determined by the sensor's physical size, rather by the number of revolutions of the light supported by the resonator, which is characterized by the resonator quality factor, or the Q-factor[11]. First papers on RRs were published in 2002, with a theoretical resolution prediction of $\partial n \approx 10^{-8}$ [12]. After that a number of significant publications followed[13,14,15,16]. Despite its small physical size, a ring resonator can deliver sensing performance similar or superior to devices like MZI while using orders of magnitude less surface area and sample volume. Furthermore, due to the small size of ring resonators, high density sensor integration becomes possible. The detection system, for the work of this thesis, is based on micro ring resonator response which was realized in the work of Heideman et al[17], where a 100×100 micron footprint microring resonator was fabricated on low-loss SiO_2/Si_3N_4, alternatively called TriPleX waveguide technology, and the theoretical resolution limit was calculated to be 1×10^{-6} RIU. To compare with, a silicon-nitride slot waveguide MZI biosensor was reported to have a resolution limit of 1.29×10^{-5} by Tu et al[18]. Despite the immense possibilities, IO-sensors have to compete with many other sensor types both within and outside the optical domain[19]. Fiber optic is the main competitor within its own domain whereas surface acoustic wave (SAW-) and microelectromechanical (MEMS-) sensors are the main competitors from the domain outside. Hence, the importance of focused research at the strong-points of IO sensors is a dominant requirement.

Ring resonators

Looking at Fig. 1.1, it can be perceived quite easily that micro ring resonators are one of the small constituents of the vast field of sensors; nothing but a speckle with progressive expansion in the horizon of optical sensing.

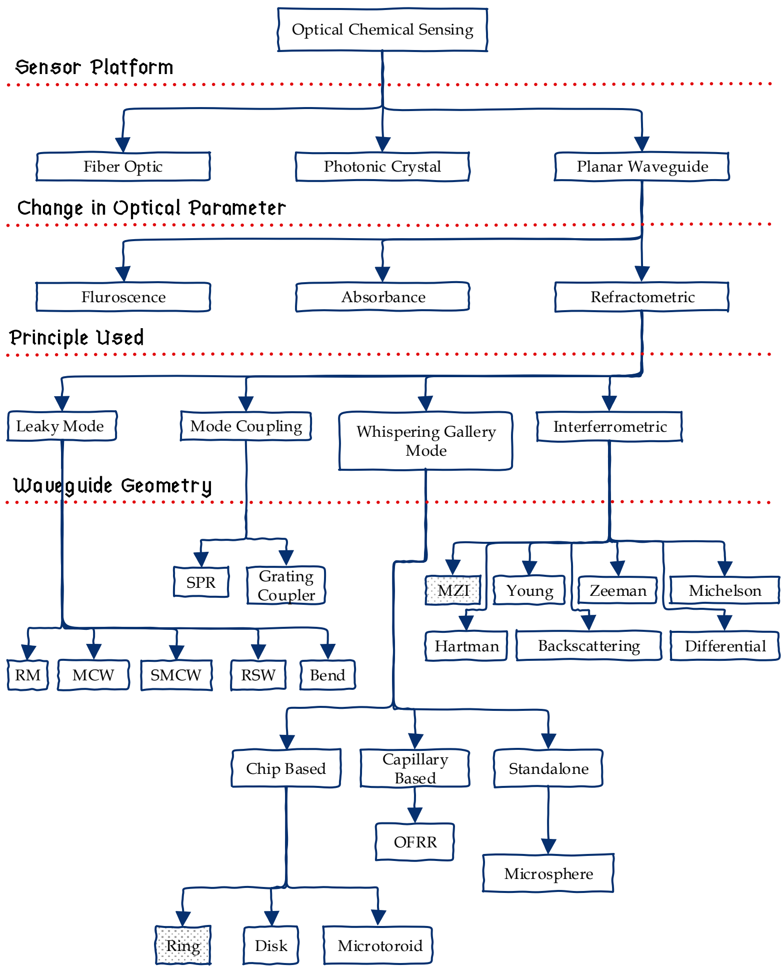

Figure 1.1: Classification of Optical Chemical Sensors

1.1 OPTICAL SENSING AND SIGNAL PROCESSING

In general, the structure of IO-sensors comprises a sequence of light source (*vertical cavity surface emitting laser*, VCSEL in the context of this work), conditioning optics, the sensing region, the read out optics, a power detector and an electronic processing unit. The main task in sensor development is identified as the suppression of influences of perturbations while maximizing the desired primary sensing effect[19]. Here one can try to reduce the magnitude of the perturbing parameters themselves, either by introducing compensating mechanisms (e.g. reference waveguides in physical sensor configuration), or by appropriate modification of the read-out method[20], such that the design shows tolerance towards the uncertainties arising from the imperfect control of the technological processes.

That brings us to our point: signal processing. An appropriate definition of signal processing can very well be the so-called *IEEE* definition[21]:

> *Signal processing is an enabling technology that encompasses the fundamental theory, applications, algorithms, and implementations of processing or transferring information contained in many different physical, symbolic, or abstract formats broadly designated as signals and uses mathematical, statistical, computational, heuristic, and/or linguistic representations, formalisms, and techniques for representation, modelling, analysis, synthesis, discovery, recovery, sensing, acquisition, extraction,learning, security, or forensics.*

Saying that, it can be concurred that signal processing is a broad area that starts as soon as the data acquisition starts. Not to lose our focal point in the vastness of signal processing, the discussion will be concentrated on two of the numerous varieties of signal processing. Fig. 1.2 represents a schematic overview of the complete measurement process. In previous section, the optical sensors were discussed. The output of the sensor chip, for real-time analysis, has to be converted from optical signal to a time series current or voltage signal. This is performed in the read out optics, e.g. photodetectors; and subsequently the analog signal is delivered for further processing. As soon as the signal is received, digital signal processing (DSP) takes place. First, the analog signal is quantized to a discrete time signal by means of an analog-digital converter (ADC). The requirement of smoothing the data further determines whether or not, filtering operation will be performed. This digitized data of the chip response is ready for analysis now. The data can either be saved and processed offline, or so called *statistical signal processing* can be implemented for a real-time accurate analysis of the data. Statistical signal processing treats signal as stochastic process. This is often the case when we intentionally add random noise to the virtual simulations in order to imitate real world situation. On the contrary, the received signal has been already compromised, primarily by shot noise from the laser, thermal noise of the electronics, quantization error of ADC and the attenuation and dispersion in the optical elements. To get accurate data, these perturbations from the external factors have to be minimized as such that the system shows extreme robustness towards influences. Statistical signal processing can help us in this aspect. Since the characteristic response of the sensors is known, we can make use of the *estimation theory*[22], which attempts to approximate the values of the parameters that directly affect the distribution of the measured data under the assumption that the measured data is random with probability distribution dependent on the parameters of interest. These estimated parameters are then delivered for numerical optimization. In the simplest case, an optimization problem consists of maximizing or minimizing a real function by systematically choosing input values from the estimator and computing the value of the function. More generally, optimization includes finding the best available values of some objective function within a set of constraints. Implementing an efficient numerical model can, in one hand, increase the accuracy at current resolution, and in the other hand, suggest on possible ways of resolution enhancement to minimize the fluctuations in physical systems.

Statistical signal processing

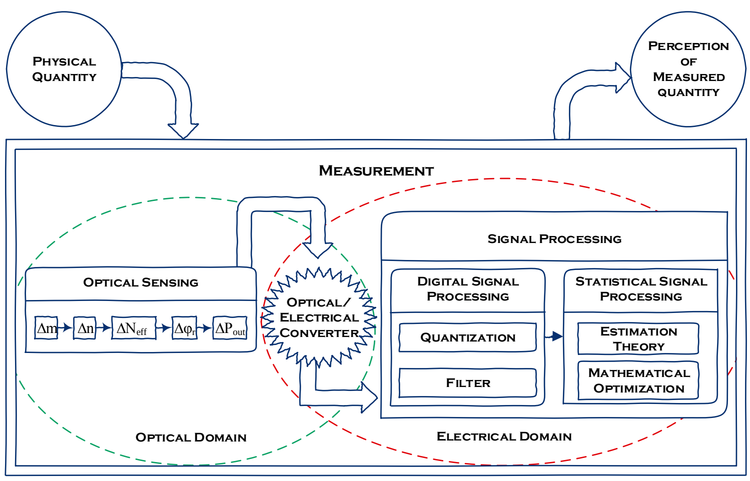

Figure 1.2: Signal processing in the perspective of optical sensing system

1.2 GOAL OF THIS THESIS

In this thesis, the aim is to further develop the existing detection system by implementing an efficient algorithm with optimized parameter estimation as well as investigate and minimize, if possible, the perturbations in the optical and electrical instruments.

To reach such a development goal, the project was divided in six parts following a top down approach. At first, the signal processing part of the measurement will be investigated for further optimization. Secondly, the limits in terms of sensitivity and drift will be determined. Thirdly, the light source will be characterized in order to find the best predicted linear behaviour of driving current and lasing wavelength. Fourthly, the limits of the readout electronics will be determined. Fifthly, influences of external factors will be minimized and the sensing platform will be optimised by including a reference ring. And finally, a market survey for a best alternative VCSEL will be carried out. Attaining optimization with these subgoals requires us to closely examine the complete problem domain, i.e., entities involved in a microring resonator detection system.

1.3 COMPLETE PROBLEM SPACE

At the beginning of the chapter, the optical sensors and signal processing and the combination of these two in a detection system were discussed. Fig. 1.3 depicts, schematically, the complete detection system that is used in the context of this work. Here, the sensor output is read in the read out optics and subsequently sent to the *data acquisition* (DAQ) card which performs digital signal processing on the analog data.

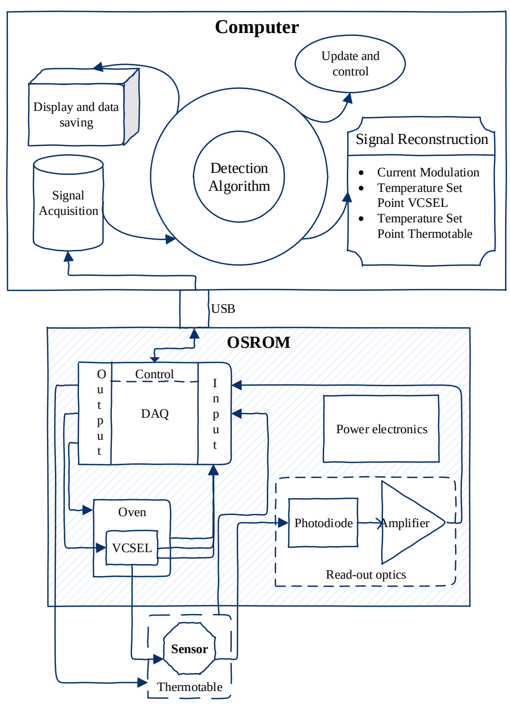

Figure 1.3: Schematic representation of complete micro-ring resonator detection system

The digitized signal is sent to the computer which, in fact, works as the controller of the DAQ. The statistical signal processing and part of digital signal processing takes place in the computer. In the figure, some of the important tasks that the computer performs in the context of sensing system are highlighted. On basis of the goals described in Section 1.2, the recognized problem space can be divided into two parts; where one part consists of the instruments of the measurement, i.e. hardware, and the other part involves the numerical analysis of the digitized data, i.e. software.

1.3.1 Hardware

Except for the sensor chip and the computer, all other instruments of measurement are integrated in a single measurement device referred to as *optical signal read-out module*, or, OSROM, which was primarily designed for using with resonant optical systems. In Fig. 1.4, the hardware that is used in the work of this thesis is presented, components of which will be referred to, from time to time, in the rest of the work. The front panel of the OSROM IV (IV being hardware version number) is shown in Fig. 1.4(a), which consists of several, largely independent functional modules, whereas the rear end features the mains connection with built-in mains switch and fuses, the universal serial bus (USB) connection,and the Bayonet Neill-Concelman (BNC) connectors for all available signals.

In front, the leftmost module is the current source driving the VCSEL diode. This current source is capable of supplying both a constant current and a periodically varying current. In the latter case, the upper and lower current limits can be independently set, with four different scan times of $0.1, 0.2, 0.5$, and 1 second periods. The current source can also be modulated with a voltage signal from either the built-in DAQ unit or the BNC input at the rear end. At any given time, the LED display shows the actual current through the VCSEL diode.

The second module from the left offers precise temperature control of the VCSEL diode. The LED display can either show the actual temperature, or the temperature set point. This set point is determined by the control knob at the front, or by a voltage from either the built-in DAQ unit or the BNC input. The VCSEL diode's optical output is featured at the bottom of this module. During measurements, it is essential to keep the VCSEL diode and the external optical chip at precisely regulated temperature. To this end, OSROM is equipped with an advanced thermal controller system. The VCSEL diode is embedded in a thermally insulated oven with a Peltier element for heating and cooling. For the sensor, the third module is a temperature controller for an external thermotable, as shown in Fig. 1.4(b), the control of which is similar to that of the VCSEL temperature. The thermotable is an external accessory, featuring a temperature-controlled surface with the possibility of mounting large variety of components. The thermotable is supplied with a thermally insulating cover and four sets of retainer posts and retainer clips.

The right hand side of the OSROM IV front panel is occupied by four independent dual optical signal amplifiers with variable input and display gain. Keeping the design of a resonant optical circuit in mind, the optical input amplifiers are arranged in pairs of two complementary inputs namely Through and Drop respectively. The gain of each input signal can be set independently in six levels. The LED bar display provides an approximate indication of the signal strength, with a display gain that is controlled independently from the input gain, albeit for both the Through and the Drop channels simultaneously.

Finally, the OSROM IV features a built-in NI USB − 6353 Data Acquisition unit (DAQ). This DAQ is connected and configured in the measurement and analysis software through USB connection.

In the hardware scheme, the VCSEL as well as the temperature controller both for VCSEL and the sensor are the primary sources of perturbation. Besides, the read-out optics, amplifiers and the DAQ contributes to the *additive white Gaussian noise* (AWGN) that is observed in the response signal.

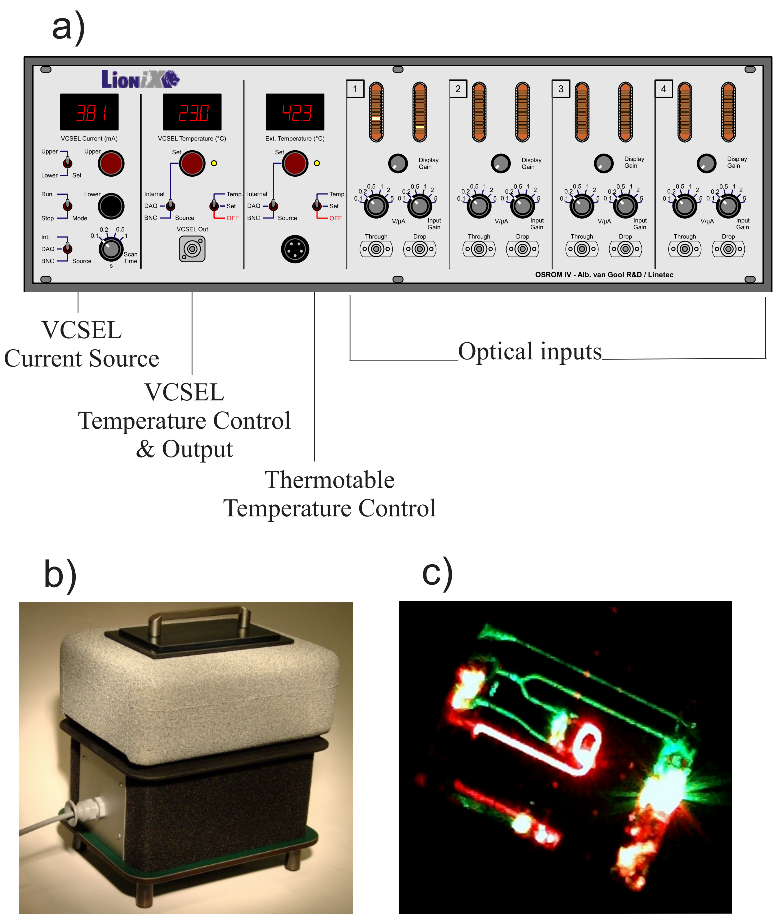

Figure 1.4: Phyical systems used in the work of theis. a) Front panel of OSROM, b) Thermotable with isolation cover on, c) A micro ring resonator illuminated with $532nm$ (green) and $635nm$ (red) laser source.

1.3.2 Software

For the control of the OSROM through the DAQ card, the very popular software for automation, National Instruments LabVIEW 8.5.3 is used. The Labview program written for this DAQ operation, whose runtime version is called 'MRR vX.0 ', uses more than 300 separate functions, termed 'VI' (Virtual Instrument) in Labview context, to provide the desired data. Peak Detection VI employs the detection algorithm to facilitate the measurement of resonant peak position of the MRR chip.It is noteworthy to mention that MRRv10.0 was the starting point for this work and referred to as *mother application*.

1.4 RESEARCH QUESTION

Based on the problem space described in Section 1.3, the following research question needs to be answered that is, in fact, the center of investigation in this thesis.

> *Research Question (RQ): How to optimize the resonance peak detection limit of a micro ring resonator in terms of accuracy and precision utilizing mathematical programming without compromising cost and time?*

1.5 RESEARCH DESIGN

The optical response of the MRR chip is read and analysed electronically. The detection scheme is in temporal domain whereas the interest lies in knowing the spectral shift in the resonance peak of the MRR. Localization in time and frequency is limited by Heisenberg's rule of uncertainty. However, within this limit the information on both dimensions is obtained at once. If we have a signal, we know the exact value of it in a given time, but we know nothing about the frequency. Of course, the Fourier transform of this signal can be performed, and then frequencies of the signal is known, yet the values of signal at a given time remains unknown. From the theoretical output power response equation of MRR, it is known that how the Drop response is with respect to input signal wavelength. The input signal wavelength is determined by the peak wavelength of the coherent emission of VCSEL at certain driving current. The VCSEL can be characterized and the current to wavelength response can be obtained. At this point, an empirical relationship can be drawn between the driving current and the lasing wavelength. Therefore, the part of Fourier analysis can be skipped and the data in time domain can be analysed by fitting a curve corresponding to the mechanistic model of the output power response. Since the knowledge of current value at each time is available, the peak value in time can be determined and related with the characterized knowledge of current to wavelength. The optimization process requirement thus becomes,

FIRST
: Implementation of an efficient curve fitting procedure in terms of accuracy and computation time.

SECOND
: Derivation of a simple, yet accurate empirical relationship between the driving current and the lasing wavelength of the VCSEL.

THIRD
: Determination of the limitations in terms of drift and sensitivity.

Fulfilling these requirements will shine light on the question of this research for the optimized detection limit of micro ring resonators.

1.6 THESIS CONTRIBUTIONS

The primary contribution of this thesis is to develop a detection system that optimizes the resonance peak detection limit of a micro ring resonator in terms of accuracy and precision utilizing mathematical programming and without compromising cost and time. The primary contribution is realized by achieving the following contributions satisfying the research question mentioned in Section 1.4.

- A Lorentzian fit approximation with an standard error of fit value $< 7 \times 10^{-5}$ with ≈ 0.11 sec computation time .
- Detection of 1 pm shift for the presence of 1.0% CO_2 in the ambient environment.
- A detection system with the measurement resolution limit of ≈ 0.04 pm, scanning resolution of 0.11 pm and a signal drift of ≈ 1 pm/h under temperature stabilized conditions.

In sum, a generic optimized system is proposed in terms accuracy and precision. Moreover, the framework is cost-efficient in terms of budget and time.

1.7 THESIS STRUCTURE

The thesis is organised from a perspective of process modelling. Optimization of the detection system is defined as the development process and modelled thereby, as shown in Fig. 1.5. In Chapter 2, the existing system and research along with their pros and cons and mathematical formulations are discussed. This is the estimation phase of this work. Based on this discussion, it is concluded that the development goals stated in Section 1.2 should be addressed in two phases. Chapter 3 presents the design schemes of the implemented algorithm in the mother application. This chapter also presents the prediction phase that was formulated on the knowledge of the estimation theory. The designs were envisioned first on basis of the theoretical background and later fine-tuned based on the trial and error analysis. The step afterwards is the calibration phase. In Chapter 4, the fluctuations observed in the physical system was explained and, simultaneously, a countermeasure towards either minimization, or avoidance is proposed. All these works sum up the complete detection system and the system evaluation in terms of algorithmic parameters and efficacy observed in bulk and surface sensing is presented in Chapter 5. Finally with a short overview of results along with the main findings on research question, the thesis concludes addressing the recommendations and future works.

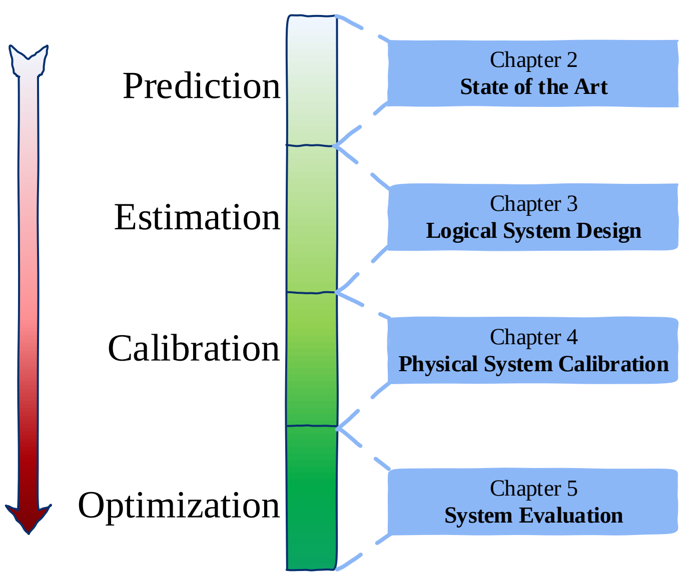

Figure 1.5: Thesis Organization

.

2

STATE OF THE ART

2.1 INTRODUCTION

To optimize the detection system, knowledge comprising multiple disciplines is required, so that adjoining different concepts results in a sound development. This chapter introduces the theories required for the optimization process alongside the overview of existing literature. It starts with the fundamental premise of the nonlinear least square curve fitting and the methods used in the literature for peak detection (Section. 2.2). The mathematical formulations of the fit algorithm, statistical concepts for fitting function and the detection methodologies reported in various publications are discussed here. Next, Section. 2.3 explains the physics of the light source and reviews briefly the reported behaviour of the fabricated VCSELs. The theories for the optical sensors and the photodetectors are reviewed, followed by the discussion of the light source, in Section. 2.4. This section also makes provision for a brief discussion on the terminologies used in the data acquisition electronics. Then, in Section. 2.5, the concepts behind thermoelectric components for temperature control, and the systemic study of deviations from the target, i.e. error analysis is introduced. A brief summary in Section. 2.6 puts an end to the theoretical discussion.

2.2 PEAK DETECTION ALGORITHM

For fitting the response curve of MRR, the resonant peak position is determined as the position where the derivative of the response curve amplitude is zero. In the context of this work, this position is termed as the peak amplitude position of the detected signal. For a quantitative measure of the performance of the system under study, the peak amplitude position is identified as the *objective*. This objective depends on certain characteristics of the system. This characteristics are referred to as *variables*. Therefore, finding the variables, for which the objective is optimized, becomes the goal towards increased accuracy and resolution of the detection system. The variables have constraints in various ways. Hence, *modelling* of a process constitutes of identifying the objective, the variables and the constraints associated with it. The first step of the optimization process is building a convenient model because a too simple model will be unsuccessful to help to understand the problem. Again, a very complex model will make the solving procedure very difficult. After the formation of the model, the succeeding step becomes implementing an optimization algorithm. An appropriate choice from a set of algorithm has to be made since algorithm universality is not a feasible option. The capability of attaining a solution and the corresponding computation time requirement will be determined by the chosen algorithm. Therefore, this is an important choice. Next, the requirement becomes to investigate whether or not a solution is found by the implemented algorithm. In spite of the failure to meet the optimality conditions, the algorithm will suggest for possible improvements

Objective, Variables & Modelling

towards current estimate for converging to a solution. This can be accomplished by means of sensitivity analysis. For a change in the variables and model, this analysis will demonstrate the responsiveness of the solution. The interpretation of the solution with regard to its applications and the incorporation of the paramount changes in the model can be performed afterwards. Finally, the optimization process commences over again provided that the model underwent some changes.

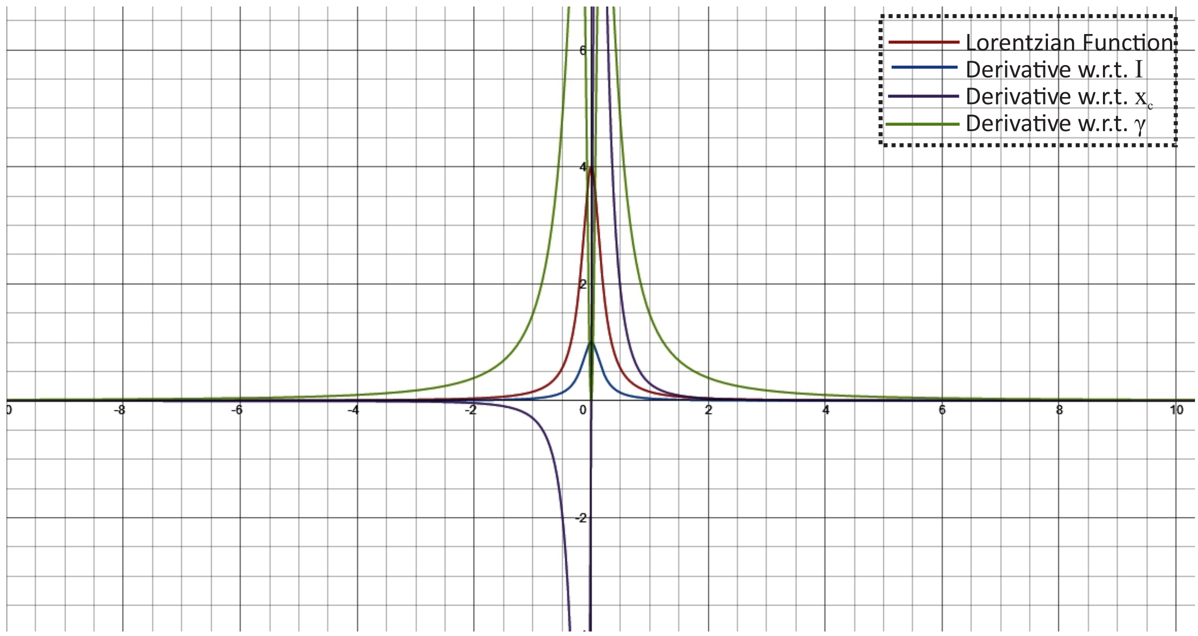

Figure 2.1: Lorentzian function and its derivatives

Simply stating, the Drop port response of the MRR chip has the form[23]

$$y_{drop} = \frac{A}{1 + B\sin^2(x)} \tag{2.1}$$

where A and B are constants. Eq. 2.1 can be well approximated by a three parameter Lorentzian function[24],[25]. The probability density function of Lorentzian distribution is given by,

$$y_{lorentzian} = I[\frac{\gamma^2}{(x - x_c)^2 + \gamma^2}] \tag{2.2}$$

Derivatives of Lorentzian w.r.t its parameters

where, the position and amplitude of the peak is x_c and I respectively, and γ is the width of the function. These constants are defined as the *parameters* of the equation. Table. 2.1 summarizes the values of these parameters in terms of the detected signal. In Eqn. 2.2, x is the independent variable and $y_{lorentzian}$ is the dependent variable of the equation. Since the lorentzian is not linear in the derivative of any of its parameters, i.e. $y_{lorentzian}$ is non linear in the derivatives with respect to I, x_c and γ, conclusion can be drawn that the relationship between them is non linear[26] as seen from Fig. 2.1. Also, for all values of x, there exists a value for y without imposing any constraints. Therefore, the model for the optimization process, in the context of this work, is nonlinear and unconstrained. Thus, the fit function of an independent variable t and a vector of n parameters $\mathbf{p}$ for the optimization process can be expressed as follows,

$$\hat{y}(t, \mathbf{p}) = y_{lorentzian}(x, [x_c, \gamma, I]) \tag{2.3}$$

PARAMETER SYMBOL	MEANING IN CONTEXT OF EQUATION	MEANING IN CONTEXT OF PROGRAMMING
x_0	Location Parameter	Value of X at the index of $max(Y)$
γ	Half Width Half Maximum	$\frac{FWHM}{2}$
I	Height of the Peak	$max(Y)$

Table 2.1: Initial Parameters for Lorentzian Distribution

The differences between the measured data, $y(t_i)$ and the fit function $\hat{y}(t_i;\mathbf{p})$ are the residuals, r_i and are expressed as

$$r_i = y(t_i) - \hat{y}(t_i;\mathbf{p}) \tag{2.4}$$

At each instance t_i, the measured data $y(t_i)$ is expressed as y_i. If a function $\hat{y}\,(t;\mathbf{p})$ is fitted to a m data points set of (t_i, y_i), where t is the independent variable and $\mathbf{p}$ is a vector of n parameters, the weighted residuals are minimized between the function $\hat{y}\,(t_i;\mathbf{p})$ and the data $y\,(t_i)$. This minimized weighted residuals act as a measure of the goodness-of-fit and subsequently defined as the *chi-squared error criterion* which is given as follows[27]

Chi-squared error criterion

$$\begin{aligned}
\chi^2(\mathbf{p}) &= \sum_{i=1}^{m}\left[\frac{r_i}{w_i}\right]^2 && (2.5)\\
&= \frac{1}{2}(y-\hat{y}(\mathbf{p}))^T\mathbf{W}((y-\hat{y}(\mathbf{p}))) && (2.6)\\
&= \frac{1}{2}y^T\mathbf{W}y - y^T\mathbf{W}\hat{y} + \frac{1}{2}\hat{y}^T\mathbf{W}\hat{y} && (2.7)
\end{aligned}$$

where, w_i is the weight and the weight matrix W_{ii} is equal to $\frac{1}{w_i^2}$. Thus, χ^2 is minimized with respect to the parameters $\mathbf{p}$ iteratively if the function is nonlinear in its vector parameters. To find the perturbation $\mathbf{h}$ in the parameters that effectively decreases χ^2 becomes the aim of each iteration. The sequential generation of improved estimates is termed *iterates* and the process continues prior to finding a solution.

The prediction for the minimizer, $\mathbf{h}$ cannot be global because our knowledge of χ^2 is usually only local to the chip response and does not take into account the noises that is present in the signal. Most algorithms are able to find only a local minimizer. Formally, a local minimizer is defined as[28]:

> A point x^* is a *local minimizer* if there is a neighbourhood N of x^* such that $f(x^*) \leqslant f(x)$ for all $x \in N$.

Local Minimizer

The usage of the strategy for iterate to iterate movement draws the distinction between the algorithms. In most of the cases, the objective function, $\hat{y}(t_i;\mathbf{p})$, its first and second derivatives and associated constraints are considered for determining the strategy. Robustness, efficiency and accuracy are the primary characteristics of good algorithms despite of the minutiae. There exists two fundamental strategies for iterate to iterate movement, namely *line search* method and *trust-region* method[29]. Though both the methods generate steps using a quadratic model of the objective function, the use of the quadratic model draws the contrast between them. In the line search method, a search direction is generated using the quadratic model with a focus on attaining a suitable step length, α along this direction. On the contrary, a region is construed around the current iterate in the trust-region method inside which the trustworthy representation of the objective function exists. This results in the choice of the approximate minimizer of

Line search & Trust region method

the model as the step[29]. Here, the recognition of the step is determined by both its direction and length. If a step turns out to be unacceptable, the size of the trust region is reduced and the search for a new minimizer starts anew. In general, reshaping the trust region size modifies the direction of the step.

The steepest descent method

In the steepest descent method, also known as *gradient descent method* and *error back-propagation* (EBP) algorithm, parameter values are updated in the opposite direction of the objective function gradient[30]. It is recognized as a highly convergent algorithm for finding the minimum of simple objective functions[31] when the number of parameters is large . For gradient descent method, the gradient of the chi-squared objective function with respect to the parameters is given by[27]

$$\begin{aligned}
\frac{\partial}{\partial \mathbf{p}}\chi^2 &= (y - \hat{y}(\mathbf{p}))^T \mathbf{W} \frac{\partial}{\partial \mathbf{p}}(y - \hat{y}(\mathbf{p})) && (2.8)\\
&= -(y - \hat{y}(\mathbf{p}))^T \mathbf{W} \left[\frac{\partial \hat{y}(\mathbf{p})}{\partial p}\right] && (2.9)\\
&= (y - \hat{y}(\mathbf{p}))^T \mathbf{WJ} && (2.10)
\end{aligned}$$

where, $\frac{\partial \hat{y}}{\partial \mathbf{p}}$ is the $m \times n$ Jacobian matrix, J. The objective function's local sensitivity to the parameter variation is represented by the Jacobian matrix. Thus, the perturbation h influencing the parameters in the steepest descent direction is given by[27]

$$h_{gd} = \alpha \mathbf{J}^T \mathbf{W} (y - \hat{y}) \tag{2.11}$$

where, α is the length of the step in the steepest-descent direction.

The EBP algorithm is also known as an inefficient algorithm because of its slow convergence arising from two aspects. Firstly, its step sizes are not adaptive to the gradients as seen from Fig. 2.2. If the step size is constant and the gradient is too steep, small step sizes should be taken so that the required minima is not lost due to the oscillation around it. Again, if the step size is constant and the gradient is gentle, the algorithm will take more time for computation redundantly. Secondly, if the error valley problem exists, the algorithm will converge slowly since the curvature of error surface will not be the same. The issue with the slow convergence of the steepest descent method can be addressed by the Gauss-Newton algorithm[32].

The Gauss-Newton Method

In the Gauss-Newton method, the sum-of-squares objective function is minimized assuming that the objective function, near the optimal solution, is proximally quadratic in the parameters. This method usually converges much faster than the gradient-descent method for average size problems[27]. The perturbed parameters are used for the function evaluation and through a first order Taylor series expansion, it is estimated as follows[27],

$$\hat{y}(p+h) \approx \hat{y}(p) + \left[\frac{\partial \hat{y}}{\partial p}\right] h = \hat{y} + Jh \tag{2.12}$$

Substituting the approximation for the perturbed function, $\hat{y} + \mathbf{Jh}$, for $\hat{y}$ in equation 2.7 results in[27],

$$\chi^2(\mathbf{p}+\mathbf{h}) \approx \frac{1}{2} y^T \mathbf{W} y + \frac{1}{2}\hat{y}^T \mathbf{W}\hat{y} - \frac{1}{2} y^T \mathbf{W}\hat{y} - (y - \hat{y})^T \mathbf{WJh} + \frac{1}{2}\mathbf{h}^T \mathbf{J}^T \mathbf{WJh} \tag{2.13}$$

It can be seen from Eqn. 2.13 that, in the perturbation $\mathbf{h}$, the chi-squared fit criterion is almost quadratic . It is also observable that the Hessian of χ^2 is approximately $\mathbf{J}^T\mathbf{WJh}$. Hessian is the

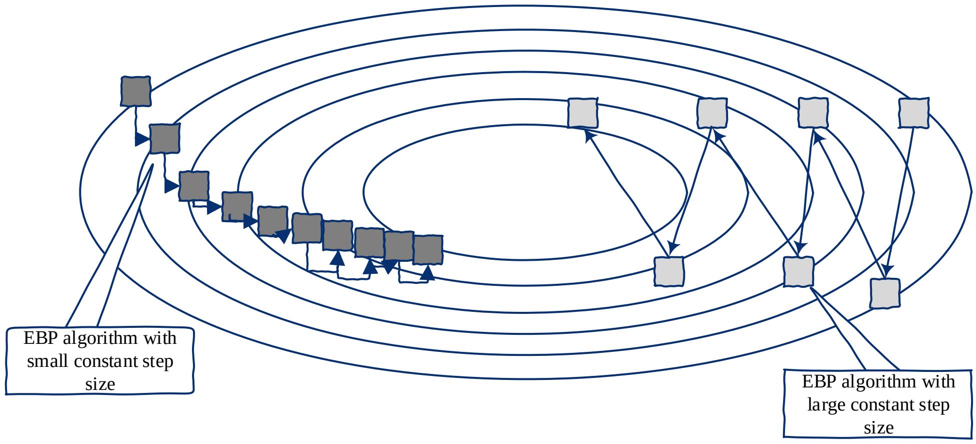

Figure 2.2: Searching process of the gradient descent method with different slope values: the trajectory for the dark squares corresponds to the small slope values that leads to slow convergence; the trajectory for the lightened squares is for large slope values that causes divergence[30]

Hessian matrix

matrix of second derivatives of the residuals. This matrix will be denoted by **H** and is equal to[33]:

$$\mathbf{H} = \begin{bmatrix} \frac{\partial r_i^2}{\partial w_1^2} & \frac{\partial r_i^2}{\partial w_1 \partial w_2} & \cdots & \frac{\partial r_i^2}{\partial w_1 \partial w_N} \\ \frac{\partial r_i^2}{\partial w_2 \partial w_1} & \frac{\partial r_i^2}{\partial w_2^2} & \cdots & \frac{\partial r_i^2}{\partial w_2 \partial w_N} \\ \cdots & \cdots & \cdots & \cdots \\ \frac{\partial r_i^2}{\partial w_N \partial w_1} & \frac{\partial r_i^2}{\partial w_N \partial w_2} & \cdots & \frac{\partial r_i^2}{\partial w_N^2} \end{bmatrix}.$$

The tangent to the graph of χ^2 at the point $(\mathbf{p};\mathbf{J})$ is horizontal when $\mathbf{J} = 0$ making $\mathbf{p}$ the critical point of χ^2. The meaning of Hessian can then be seen best. At this instant, a quadratic polynomial becomes the best approximate for the values of χ^2 near $\mathbf{p}$, which is a parabola with vertex $\mathbf{p}$. Its arms goes down if $\mathbf{H} < 0$ confirming $\mathbf{p}$ as a local maximum. Conversely, its arms goes up if $\mathbf{H} > 0$ establishing $\mathbf{p}$ as a local minimum. In both cases, the requirement is that χ^2 stays close to the parabola. However, the behaviour of χ^2 near $\mathbf{p}$ is uncertain if $\mathbf{H} = 0$. As in the case of the best approximant of first degree, it is the best approximant of second degree, but it would mean that the convergence is not achieved in the context of the algorithms. Therefore if $\mathbf{J} = 0$, then, in case[33]

$$\mathbf{H} = \begin{cases} <0 & \text{means } \mathbf{p} \text{ is a local maximum for } \chi^2\text{, thus not acceptable;} \\ >0 & \text{means } \mathbf{p} \text{ is a local minima for } \chi^2\text{, thus acceptable;} \\ =0 & \text{means the convergence was not achieved.} \end{cases}$$

Setting the derivative of χ^2 to zero, the minima in the perturbation **h** is found to be[27]

$$\frac{\partial}{\partial h}\chi^2(\mathbf{p}+\mathbf{h}) \approx -(y-\hat{y})^T \mathbf{W}\mathbf{J} + \frac{1}{2}\mathbf{h}^T\mathbf{H} \tag{2.14}$$

For the Gauss-Newton perturbation, the resulting normal equation becomes[27]

$$[\mathbf{H}]h_{gn} = \mathbf{J}^T\mathbf{W}(y-\hat{y}) \tag{2.15}$$

Point to be noted in this aspect, the improvement of fast convergence of the Gauss-Newton algorithm takes place at the instance of a reasonable quadratic approximation of the error function. Otherwise, it will result in being divergent[30].

The Levenberg-Marquardt Method

The Levenberg-Marquardt (Lev-Mar) algorithm is a combination of two minimization methods discussed previously: the gradient descent method and the Gauss-Newton method. In the direction towards the greatest reduction of the least squares objective, the EBP algorithm minimizes the sum of the squared errors through the update of the parameters. On the contrary, the sum of the squared errors are decreased by the Gauss-Newton method via searching the minimum under the assumption of a quadratic least squares function. The Levenberg-Marquardt method behaves like a gradient-descent method when the estimated parameters are far from their optimal value, and when the estimation is close to the optimal value, this method behaves like the Gauss-Newton method. So, the Lev-Mar algorithm adaptively updates the parameter values between the gradient descent update and the Gauss-Newton update as follows[27],

$$[\mathbf{H} + \lambda \mathbf{I}]h_{lm} = \mathbf{J}^T \mathbf{W}(y - \hat{y}) \tag{2.16}$$

where, λ is the algorithmic parameter. If λ is large, the perturbation $\mathbf{h}$ is updated using gradient descent method, whereas a smaller value results in a Gauss-Newton update. Lev-Mar utilizes the EBP algorithm at greater distances from the function minimum for maintaining a steadfast convergent progress toward the solution. This results in a rapid and steady convergence to the solution. However, Eqn. 2.16 has the disadvantage that the calculated Hessian matrix is completely unused for larger values of λ. Even in cases like this, the second derivative can provide some advantages through the scaling of each component's gradient conforming to the curvature. The error valley problem ceases to exist for a larger movement along the smaller gradient direction as a result. Marquardt administered this important observation. The diagonal of the Hessian became the substitute for the identity matrix, $\mathbf{I}$ in Eq. 2.16 emerging as the Levenberg-Marquardt update rule[34] as follows,

$$[\mathbf{H} + \lambda \mathrm{diag}(\mathbf{H})]h_{lm} = \mathbf{J}^T \mathbf{W}(y - \hat{y}) \tag{2.17}$$

The curvature of χ^2 and the Hessian are proportional to each other. Eqn. 2.17 thus implements that in the high and low curvature direction, a small and a large step will be taken accordingly.

However there are some disadvantages of this algorithm. First of all, it needs matrix inversion as part of the update. Albeit the implementation of clever pseudo-inverse methods to compute the inverse, the excessive update cost culminates for a model size of few thousand parameters[35]. Secondly, the Lev-Mar is extremely dependent on the initial guess for the parameters[27]. Either convergence to a local minima or no convergence at all by the algorithm depends on the initial weights of the network. Besides that, it is an extremely fast method and works extremely well in practice.

2.3 LIGHT SOURCE - VCSEL

Vertical Cavity Surface-Emitting Laser (VCSEL) emits beam in the perpendicular direction to the surface of the wafer. VCSELs are laser diodes. Its monolithic resonator is created by sandwiching the active region by either two highly reflective multilayer reflectors, or distributed Bragg reflectors (DBRs). The reflectors are composed of alternating layers of high and low refractive index and are quarter wavelength thick. The required gain is obtained by the injection of carriers into the active region through a p-n junction. The VCSEL starts to lase at a current when the round trip gain readjusts the round trip loss. This defines the threshold current. Stimulated emission produces coherent light above the threshold current. The lowest reflective DBR outcouples this emission from the top side. In case where bottom emission is preferred, either substrate removal or transparent substrate is required. The DBRs are based on either semiconductors or dielectric materials. Doped semiconductor DBRs can support conducive current injection. However, DBRs with suitable index contrast are not always feasible. Moreover, DBRs are the source of optical losses from free carrier absorption and electrical resistance. To address this issue, intracavity contacts are used for current injection. If dielectric DBRs are used with intracavity contact, they pare down the optical loss and the electrical resistance as well as exhibit their remarkable intrinsic thermal conductivity. This combination thus results in improved performance and efficiency[36].

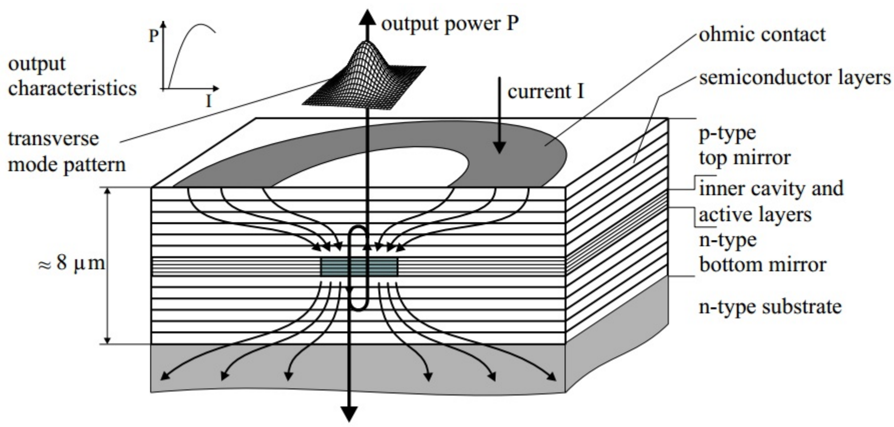

Figure 2.3: Schematic layer structure and operation principle of a VCSEL taken from Michalzik et al.[37]

Fig. 2.3 illustrates the typical layout of a VCSEL. The inner cavity incorporates the amplifying layer of the VCSEL. Electrically conductive layer stacks envelops this amplifying layer. To yield the optical feedback, these electrically conductive layer stacks serve as the laser mirrors. VCSELs designed for 850 to 980 nm wavelength emission need about 8 μm of epitaxially grown material with some ten nm thick active region[37]. Metal organic chemical vapour deposition (MOCVD), or molecular beam epitaxy (MBE) is used for the crystal growth during the process of fabrication. *Structure of VCSEL*

The ohmic contacts in the top and the bottom side serves as the input for current injection in a simplest device layout. To confine current at the predefined active area, implementation of several methods (e.g. US7026178B2, US6876687B2, US6589805B2) have seen remarkable success. In contrast, reduction of the optical losses in the cavity is introduced by selective oxidation. The active diameter of the VCSEL can be as small as a few micrometers for attaining the lowest threshold currents in the sub$-100\ \mu A$ range. For attaining high output powers beyond $100\ mW$, this diameter can also outstrip $100\ \mu m$. In absence of extended cavity, planar, selectively oxidized VCSELs emit in a single transverse mode pragmatically, as indicated in Fig. 2.3, up to active diameters of about $4\ \mu m$[37]. As the device gets larger in size, it starts to lase at several higher radial and azimuthal order modes around the threshold. Though the optical power-current curve has a constant slope above threshold, it shows a characteristic roll-over for higher currents due to internal heating. In contrast with EELs, operating VCSELs up to their maximum output powers is not critical because of the lower kW/cm^2 power density[37]. The semiconductor material or the laser facet does not experience any optical damage due to this sparse power density. Moreover, the gain peak of the resonator in the conventional EELs determines the emission wavelength, λ_0, whereas the emission wavelength of a VCSEL is determined by the cavity resonance due to its short optical resonator. Therefore a shift in the emission wavelength is *Temperature behaviour of VCSEL* seen due to the thermal fluctuation. This thermal shift results from the change in the refractive index of the resonator predominantly, and from the thermal expansion of the semiconductor layers to a smaller extent. For VCSELs emitting at 800-1000 nm, the modal wavelength shift is found to be $\frac{\partial\lambda}{\partial T} \approx 0.07$ nm/K[37].

2.4 DETECTION AND DATA ACQUISITION ELECTRONICS

In this section, the theory of the optical sensors (i.e. micro ring resonator (MRR) and Mach-Zender Interferrometer (MZI)) used in this work, the operating principle of photodiodes and the general concepts of data acquisition are discussed.

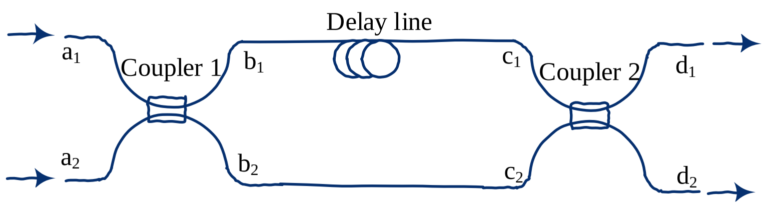

Figure 2.4: Schematic representation of a Mach-zehnder interferometer with two inputs and two outputs.

Mach-Zehnder Interferometer

To start with, a Mach Zehnder interferrometer can be formed using the basic components like two directional couplers and a delay line as shown in Fig. 2.4. The transfer matrix of the first coupler in this figure can be written as[38]

$$\begin{bmatrix} b_1 \\ b_2 \end{bmatrix} = \begin{bmatrix} s_{11} & s_{12} \\ s_{21} & s_{22} \end{bmatrix} \cdot \begin{bmatrix} a_1 \\ a_2 \end{bmatrix} \tag{2.18}$$

where a_i and b_i are the electrical fields at the input and output ports, respectively. It is assumed from here on that the couplers are reciprocal and lossless. This assumption, in terms of mathematics, means that[38]

$$s_{12} = s_{21} \tag{2.19}$$

and

$$|b_1|^2 + |b_2|^2 = |a_1|^2 + |a_2|^2 \tag{2.20}$$

Energy conservation law suggests that[38]

$$|s_{11}|^2 + |s_{12}|^2 = 1 \tag{2.21}$$

$$|s_{21}|^2 + |s_{22}|^2 = 1 \tag{2.22}$$

$$s_{11}s_{12}^* + s_{21}s_{22}^* = 0 \tag{2.23}$$

Therefore, using Eqn. 2.19, 2.21 and 2.22, we get

$$|s_{11}|^2 + |s_{12}|^2 = |s_{21}|^2 + |s_{22}|^2 \tag{2.24}$$

$$|s_{11}|^2 = |s_{22}|^2 \tag{2.25}$$

Let, ϵ be the fraction of power that is coupled from input port 1 to output port 2. This coupling ratio becomes $\sqrt{\epsilon}$ for the optical field[38]. Since s_{11} and s_{22} are symmetrical, a real valued $s_{11} = \sqrt{1-\epsilon}$ will indicate an equal real value for s_{22}. Considering a phase shift due to the cross coupling term, s_{12} and s_{21} will be equal to $\sqrt{\epsilon}e^{j\phi}$. Replacing the values of s_{11}, s_{12}, s_{21} and s_{22} in Eqn. 2.18, we get[38]

$$\begin{bmatrix} b_1 \\ b_2 \end{bmatrix} = \begin{bmatrix} \sqrt{1-\epsilon} & \sqrt{\epsilon}e^{j\phi} \\ \sqrt{\epsilon}e^{j\phi} & \sqrt{1-\epsilon} \end{bmatrix} \cdot \begin{bmatrix} a_1 \\ a_2 \end{bmatrix} \tag{2.26}$$

and in Eqn. 2.23

$$\sqrt{1-\epsilon}\sqrt{\epsilon}e^{-j\phi} + \sqrt{\epsilon}e^{j\phi}\sqrt{1-\epsilon} = 0 \tag{2.27}$$

$$e^{-j\phi} + e^{j\phi} = 0 \tag{2.28}$$

The solution of Eqn. 2.28 is $\phi = \frac{\pi}{2}$ resulting in $e^{j\phi} = j$. Finally, Eqn. 2.26 becomes[38]

Transfer matrix of lossless symmetric coupler

$$\begin{bmatrix} b_1 \\ b_2 \end{bmatrix} = \begin{bmatrix} \sqrt{1-\epsilon} & j\sqrt{\epsilon} \\ j\sqrt{\epsilon} & \sqrt{1-\epsilon} \end{bmatrix} \cdot \begin{bmatrix} a_1 \\ a_2 \end{bmatrix} \tag{2.29}$$

representing the transfer matrix of a 2×2 coupler. Next, we look for the transfer matrix of the delay line. It simply becomes[38]

$$\begin{bmatrix} c_1 \\ c_2 \end{bmatrix} = \begin{bmatrix} e^{j\phi_1} & 0 \\ 0 & e^{j\phi_2} \end{bmatrix} \cdot \begin{bmatrix} b_1 \\ b_2 \end{bmatrix} \tag{2.30}$$

where, $\phi_i = \dfrac{2\pi}{\lambda} n_i L_i$ is the phase delays of the i-th delay line resulting from the corresponding optical path length difference. At the end, a similar coupler is placed which combines the output of the delay lines and passes to the two output ports. The overall transfer matrix of a MZI can now be written as follows[38]

Transfer matrix of MZI

$$\begin{bmatrix} d_1 \\ d_2 \end{bmatrix} = \begin{bmatrix} \sqrt{1-\epsilon} & j\sqrt{\epsilon} \\ j\sqrt{\epsilon} & \sqrt{1-\epsilon} \end{bmatrix} \begin{bmatrix} e^{j\phi_1} & 0 \\ 0 & e^{j\phi_2} \end{bmatrix} \begin{bmatrix} \sqrt{1-\epsilon} & j\sqrt{\epsilon} \\ j\sqrt{\epsilon} & \sqrt{1-\epsilon} \end{bmatrix} \begin{bmatrix} a_1 \\ a_2 \end{bmatrix} \tag{2.31}$$

For maximum extinction ratio, majority of the MZIs uses a power splitting ratio of 50% implying $\epsilon = 0.5$. Eqn. 2.31 then reduces to the following form[38],

$$\begin{bmatrix} d_1 \\ d_2 \end{bmatrix} = \frac{1}{2} \begin{bmatrix} (e^{-j\phi_1} - e^{-j\phi_2}) & j(e^{-j\phi_1} + e^{-j\phi_2}) \\ j(e^{-j\phi_1} + e^{-j\phi_2}) & -(e^{-j\phi_1} - e^{-j\phi_2}) \end{bmatrix} \begin{bmatrix} a_1 \\ a_2 \end{bmatrix} \tag{2.32}$$

If the second input port is disconnected, we can write d_1 and d_2 as[38]

$$d_1 = \frac{1}{2}(e^{-j\phi_1} - e^{-j\phi_2})a_1 = e^{-j\phi_0}\sin(\frac{\Delta\phi}{2})a_1 \tag{2.33}$$

and

$$d_2 = \frac{j(e^{-j\phi_1} + e^{-j\phi_2})}{2}a_1 = je^{-j\phi_0}\cos(\frac{\Delta\phi}{2})a_1 \tag{2.34}$$

where, $\phi_0 = \dfrac{(\phi_1 + \phi_2)}{2}$ is the average phase delay and $\Delta\phi = (\phi_1 - \phi_2)$ is the differential phase shift of the two MZI arms. Then, the optical power transfer function from input port 1 to output port 1 is given by[38]

Optical power transfer function of MZI

$$T_{11} = \left.\frac{d_1}{a_1}\right|_{a_2=0} = \sin^2\left[\frac{\pi f}{c}(n_2L_2 - n_1L_1)\right] \tag{2.35}$$

and the optical power transfer function from input port 1 to output port 2 is given by[38]

$$T_{12} = \frac{d_2}{a_1}\bigg|_{a_2=0} = \cos^2\left[\frac{\pi f}{c}(n_2L_2 - n_1L_1)\right] \tag{2.36}$$

where, $f = \dfrac{c}{\lambda}$ is the frequency and c is the speed of light. Obviously, the optical powers coming out of the two output ports are complementary such that $T_{11} + T_{22} = 1$. The transmission efficiencies T_{11} and T_{12} of an MZI are the functions of both the wavelength λ and the differential optical path length $\Delta l = n_2L_2 - n_1L_1$ between the two arms. For checking the current to wavelength linearization in Section. 4.2, Eqn. 2.36 was used.

Micro ring resonator

As seen for MZI, most optical sensors are two port devices with input and output ports. A microring resonator (MRR) is also a two port device. However, a four port MRR is realised by adding an additional port waveguide to a two port MRR. The power transfer at the added port waveguide is only possible at discrete wavelengths. Fig. 2.5 depicts a four port MRR schematically. Inside the ring, the power build up occurs in three steps; namely, the initial, the transient and the equilibrium stage. Initially, the incoming light, I_{in} propagates along one of the port waveguides. As the light reaches the coupler, a small fraction of light goes into the ring as $\kappa_1^2.I_{in}$. Most of the light will pass as $I_{through}$. The fraction of light that is coupled inside the ring resonator (RR), termed I_{cav1}, eventually reaches the second coupler. Like the previous case, a small fraction $\kappa_2^2.I_{cav1}$ will couple out as I_{drop}, while most of I_{cav1} will propagate inside the ring as I_{cav2}. After completing a successful roundtrip, light inside the ring reaches the first coupler again. In transient stage, I_{cav2} will interfere with the incoming light if the phase of the incoming light is a integer multiple of 2π. In this case, the steady power build up can follow. As a result, I_{drop} will increase while $I_{through}$ experiences a decrease. Power inside the resonator cannot increase infinitely, therefore, it reaches a state of equilibrium when the power level of I_{in} and I_{drop} is in equilibrium. Thus, no additional power is transferred from input port to drop port implying that I_{drop} is at its maxima, while $I_{through}$ is at its minima.

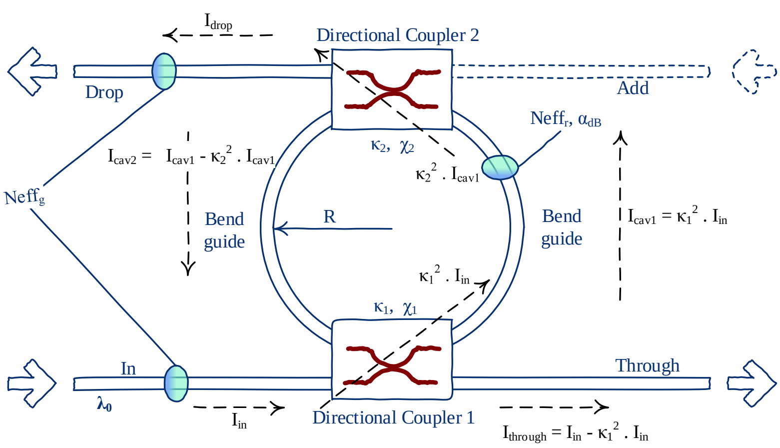

Figure 2.5: Micro-resonator model components and parameters. Dotted black arrows shows light coupling into the microresonator in the initial phase.

Transfer matrix of asymmetric coupler

For MZI, the transfer matrix of symmetric couplers was shown. In case of asymmetric coupler, the transfer matrix can be written as[39],

$$M_A = \sqrt{1-\chi_c^2}\begin{bmatrix} \cos(\phi_A) - jA.\sin(\phi_A) & -jB.\sin(\phi_A) \\ -jB.\sin(\phi_A) & \cos(\phi) + jA.\sin(\phi_A) \end{bmatrix} \tag{2.37}$$

where, χ_c is the coupler loss, ϕ_A is the phase given by $\Delta.L_{eff}$, L_{eff} being the effective coupling length between the ring and the waveguides, A and B are the degree of asymmetric strength in a coupler at a given wavelength and mathematically[39]

$$\begin{aligned} A^2 + B^2 &= 1\,;\; 0 \leqslant A < 1,\, 0 < B \leqslant 1 && (2.38)\\ A &= \frac{(\beta_r - \beta_g)}{2\Delta} && (2.39)\\ B &= \frac{\sqrt{\epsilon}}{\Delta} && (2.40)\\ \Delta &= \sqrt{\left[\frac{(\beta_r - \beta_g)}{2} + \epsilon\right]} && (2.41) \end{aligned}$$

In the above equations, β_r and β_g are the propagation constants of the ring and the waveguide respectively. The effective refractive index is introduced through the propagation constant as follows

Propagation constant

$$\beta = k.n_{eff} = \frac{2\pi}{\lambda}.n_{eff} \qquad (2.42)$$

where, k is the vacuum wavenumber related to λ by $\frac{2\pi}{\lambda}$. Therefore, the device asymmetry arises mainly from the difference between the effective refractive indices n_{eff-g} and n_{eff-r}, also known as *phase mismatch*. This mismatch affects the coupling of the light between the ring and the bus waveguide. For strong coupling, the mismatch should be kept to minimum. Else, it will negatively influence the device performance. However, the device symmetry can be implemented by setting $n_{eff-g} = n_{eff-r}$. Eqn. 2.39, 2.40 and 2.41 then becomes

$$\begin{aligned} A &= 0 && (2.43)\\ B &= 1 && (2.44)\\ \Delta &= \sqrt{\epsilon} && (2.45) \end{aligned}$$

For the symmetry assumption, the phase, ϕ_A takes the value of $\sqrt{\epsilon}.L_{eff}$. Replacing the values of A, B, Δ and ϕ_A in Eqn. 2.37, we get the transfer matrix of the symmetric coupler as follows[39],

Transfer matrix of lossy symmetric coupler

$$M_S = \sqrt{1-\chi_c^2}\begin{bmatrix} \cos(\sqrt{\epsilon}.L_{eff}) & -j\sin(\sqrt{\epsilon}.L_{eff}) \\ -j\sin(\sqrt{\epsilon}.L_{eff}) & \cos(\sqrt{\epsilon}.L_{eff}) \end{bmatrix} \qquad (2.46)$$

In analogy with Eqn. 2.29, for a lossless coupler we can write[23]

$$M = \begin{bmatrix} \mu & -j\kappa \\ -j\kappa & \mu \end{bmatrix} \qquad (2.47)$$

where, $\mu = \sqrt{[1-\kappa^2]}$. Eqn. 2.47 implies that $\mu = \cos(\sqrt{\epsilon}.L_{eff})$ and $\kappa = \sin(\sqrt{\epsilon}.L_{eff})$. The straightforward approach to calculate $\sqrt{\epsilon}$ for straight directional coupler is to use 2D modesolver. This approach becomes insufficient when it comes to the couplers of a ring resonator[23]. On the other hand, 3D simulation using couple mode theory (CMT) or beam propagation method (BPM) can directly calculate the field coupling coefficient, κ of the ring resonator couplers. Thus, using Eqn. 2.46 over Eqn. 2.47 is advantageous from the design point of view[23].

We can simplify Fig. 2.5 by expressing it in a control engineering diagram with feedback loop as shown in Fig.2.6. In analogy with s_{12} and s_{21} of MZI, the field propagation term of the ring resonator can be written as[40],

$$s_r = e^{-j\phi_r}.\alpha_r \qquad (2.48)$$

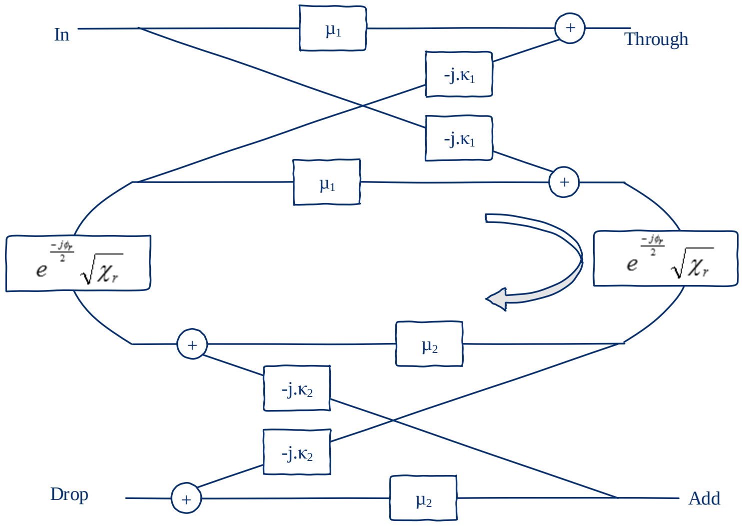

Figure 2.6: Control engineering representation of a unidirectional four port micro-resonator[23].

where, α_r is the roundtrip loss coefficient and ϕ_r is the roundtrip phase related to the circumference of the ring by[40]

$$\phi_r = \frac{\omega L}{c} \tag{2.49}$$

where, $L = 2\pi r$ is the circumference of the ring, r is the radius of the ring, c is the modal phase velocity of the ring given by $\frac{c_0}{n_{eff}}$ and the angular frequency, ω is the product of wavenumber, k and the vacuum speed of light c_0. Therefore, Eqn. 2.49 can be rewritten as[40]

$$\phi_r = \frac{kc_0 \times 2\pi r}{c_0/n_{eff}} \tag{2.50}$$

$$= 4\pi^2 n_{eff} \frac{r}{\lambda} \tag{2.51}$$

For a resonator, the effective overall distributed loss coefficient, α_r accounts for the diffraction losses of the mirrors and the losses due to the absorption and scattering in the guiding medium[41]. However, for ring resonators, these losses are incorporated in the modal loss, α_{dB} and the roundtrip loss coefficient is given by[23]

$$\alpha_r = 2\pi r \alpha_{dB} \tag{2.52}$$

In case of calculating electric field, we can introduce the roundtrip loss factor as[23]

$$\alpha_r = 20 \log_{10} \chi_r \tag{2.53}$$

$$\chi_r = 10^{\frac{-\alpha_r}{20}} \tag{2.54}$$

From Fig. 2.6, the two halves of the ring, thus have a field propagation term[23]

$$s_{\frac{r}{2}} = e^{-j\frac{\phi_r}{2}} \sqrt{\chi_r} \tag{2.55}$$

In spectral domain, the ring resonator has through and drop response. The power fraction that goes from the input port IN to the DROP port is termed as *drop* response, whereas the remaining power that transfers from IN port to the THROUGH port is known as *through* response. Since the focus of this work was on drop response, we can further simplify Fig. 2.6 to Fig. 2.7. For a signal flow graph like this, we can apply Mason's rule to determine the transfer

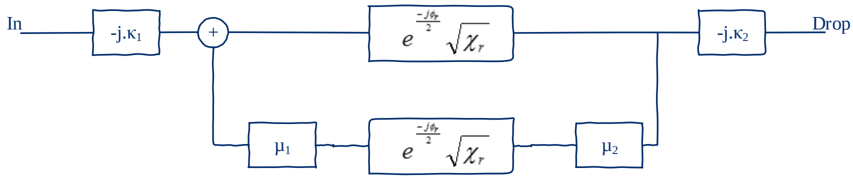

Figure 2.7: Simplified resonator model used to obtain the drop response[23].

function. The rule states that, if each node is a variable, the transfer function of a linear system H_{ij} between two nodes x_i and x_j can be expressed as[23],

Mason's rule

$$H_{ij} = \frac{\sum_k P_{ijk}\Delta_{ijk}}{\Delta} \tag{2.56}$$

where, P_{ijk} is the k-th direct path from x_i to x_j, Δ_{ijk} is the cofactor of P_{ijk} and Δ is the determinant of the system given by[23],

$$\begin{aligned}\Delta = 1 - (\text{sum of all individual loop gain}) + (\text{sum of the products of two non} - \text{touching loop})\\ -(\text{sum of the products of three non} - \text{touching loop}) + \dots\end{aligned} \tag{2.57}$$

From Fig. 2.7, only one direct path is available. Thus[23],

$$H_{IN-DROP} = \frac{\kappa_1\kappa_2 e^{\frac{-j\phi_r}{2}}\sqrt{\chi_r} \times (-1)}{1 - (\mu_1\mu_2 e^{-j\frac{\phi_r}{2}}\chi_r \times e^{-j\frac{\phi_r}{2}})} \tag{2.58}$$

$$\frac{E_{drop}}{E_{in}} = \frac{-\kappa_1\kappa_2.e^{-j\frac{\phi_r}{2}}.\sqrt{\chi_r}}{1 - \mu_1\mu_2 e^{-j\frac{\phi_r}{2}}.\sqrt{\chi_r}} \tag{2.59}$$

For power in the drop port, we square the above equation and get[23]

$$\frac{P_{drop}}{P_{in}} = \frac{\left|-\kappa_1\kappa_2.e^{-j\frac{\phi_r}{2}}.\sqrt{\chi_r}\right|^2}{\left|1 - \mu_1\mu_2 e^{-j\frac{\phi_r}{2}}.\sqrt{\chi_r}\right|^2} = \frac{\kappa_1^2\kappa_2^2\chi_r}{(1-\mu_1\mu_2.\chi_r)^2 + 4\mu_1\mu_2.\chi_r\sin^2(\frac{\phi_r}{2})} \tag{2.60}$$

At resonance, $\phi_r = 2\pi m$ leads to the maximum power, H at the drop port as[23]

Maximum drop port power

$$\frac{P_{drop}}{P_{in}} = H = \frac{\kappa_1^2\kappa_2^2\chi_r}{(1-\mu_1\mu_2.\chi_r)^2} \tag{2.61}$$

The key parameters of the ring resonator is similar to an optical filter. Free spectral range (FSR), $\Delta\lambda$ is defined as the distance between two consecutive resoance peak. Therefore, the difference between vacuum wavelength at two consecutive resonance condition is the FSR. From the propagation constant, β in Eqn. 2.42, FSR can be calculated as follows[40],

Free spectral range of MRR

$$\frac{\partial\beta}{\partial\lambda} = -\frac{\beta}{\lambda} + k\frac{\partial n_{eff}}{\partial\lambda} \approx -\frac{\beta}{\lambda} \tag{2.62}$$

$$FSR = \Delta\lambda = -\frac{2\pi/L}{\partial\beta/\partial\lambda} = \frac{\lambda^2}{n_{eff}L} \tag{2.63}$$

where, the wavelength dependency of the refractive index is neglected. If this dependency cannot be neglected, or, more precise calculation is required, the group index, n_g can be used. It is given by,

$$n_g = n_{eff} - \lambda\frac{\partial n_{eff}}{\partial\lambda} \tag{2.64}$$

Therefore, Eqn. 2.62 becomes,

$$\frac{\partial \beta}{\partial \lambda} = -\frac{k}{\lambda} n_g \tag{2.65}$$

resulting in a FSR as follows[40]

$$\Delta\lambda = \frac{\lambda^2}{n_g L} \tag{2.66}$$

The resonance linewidth is another key parameter for the ring resonator. It is defined as the full width half maximum (FWHM) bandwidth, $2\partial\lambda$, where the amplitude is 3 dB lower than the maximum amplitude. From Eqn. 2.60 and 2.61, the power at 3 dB points corresponds to

Full-width half maximum of MRR

$$\frac{\left(-\kappa_1 \kappa_2 e^{-j\frac{\phi_r}{2}} . \sqrt{\chi_r}\right)^2}{1 - 2\mu_1 \mu_2 \chi_r \cos(\phi_r) + (\mu_1 \mu_2 \chi_r)^2} = \frac{1}{2} \frac{(\kappa_1 \kappa_2 \sqrt{\chi_r})^2}{(1 - \mu_1 \mu_2 . \chi_r)^2} \tag{2.67}$$

$$\Rightarrow 2(1 - \mu_1 \mu_2 . \chi_r)^2 = 1 - 2\mu_1 \mu_2 \chi_r \cos(\phi_r) + (\mu_1 \mu_2 \chi_r)^2 \tag{2.68}$$

Euler theorem states that, for small values of θ, $\cos\theta = \left[1 - \frac{\theta^2}{2}\right]$. Therefore, replacing the value of $\cos(\phi_r)$ in Eqn. 2.68, we get[23]

$$\phi_r = \frac{1 - \mu_1 \mu_2 . \chi_r}{\sqrt{\mu_1 \mu_2 . \chi_r}} \tag{2.69}$$

If the couplers are reciprocal and lossless, then Eqn. 2.69 becomes[23]

$$\phi_r = \frac{1 - \mu^2}{\mu} \tag{2.70}$$

Using Eqn. 2.50 and 2.65, we can derive the linewidth as follows[40]

$$2\partial\lambda = \frac{\lambda^2}{\pi L n_{eff}} \frac{1 - \mu^2}{\mu} \tag{2.71}$$

The commonly used form considers weak coupling and $\lambda >> \partial\lambda$; and thus, the FWHM has the following form[40]

$$2\partial\lambda = \frac{\kappa^2 \lambda^2}{\pi L n_{eff}} \tag{2.72}$$

Finesse of MRR

The finesse, F of a ring resonator can now be found using Eqn. 2.66 and 2.71. The ratio between the FSR and FWHM is defined as finesse. A high finesse means a large free spectral range with a small resonator linewidth. Thus it is a measure of the spectral resolution and useful for optical spectrum analysis. Mathematically[23,40],

$$F = \frac{FSR}{FWHM} \tag{2.73}$$

$$= \frac{\pi}{\kappa^2};\ for\,weak\,coupling \tag{2.74}$$

$$= \frac{\pi\sqrt{\mu_1 \mu_2 . \chi_r}}{1 - \mu_1 \mu_2 . \chi_r};\ for\,strong\,coupling \tag{2.75}$$

The finesse factor, F_c is defined as[40]

Finesse factor of MRR

$$F_c = \frac{1}{\sin^2\left(\frac{\pi}{2F}\right)} \tag{2.76}$$

Since, F is a very large number, $\frac{\pi}{2F}$ becomes very small. Using small angle approximation $\sin\theta \approx \theta$ and replacing the value of F in Eqn. 2.76, we get[23]

$$F_c = \frac{4\mu_1\mu_2\chi_r}{(1-\mu_1\mu_2.\chi_r)^2} \tag{2.77}$$

Using Eqn. 2.61 and 2.77, we can rewrite Eqn. 2.60 the output power equation of the drop response as[23]

Output power equation of the drop response

$$\frac{P_{drop}}{P_{in}} = \frac{H}{(1+F_c\sin^2(\frac{\phi_r}{2})} \tag{2.78}$$

Finally, the sharpness of the resonance is measured by Q factor. It can be either regarded as the stored energy per unit power loss per optical cycle, or the ratio of operating wavelength and FWHM. Mathematically[40],

Q factor of MRR

$$Q = \frac{\lambda}{2\partial\lambda} = \frac{n_{eff}L}{\lambda}F \tag{2.79}$$

All these parameters determine the wavelength shift of the peak that results from the change of n_{eff} in the RR itself. A change in the refractive index of the cladding medium induces a change in n_{eff}. Therefore, Δn_{eff} is related to $\Delta\lambda$ as[42]

$$\frac{\partial n_{eff}}{\partial\lambda} = \frac{n_g}{\lambda} \tag{2.80}$$

Once the on resonance wavelength, λ_{on-res} is determined from the power response equation, the bulk sensitivity of the ring resonator for a small change in the cladding layer refractive index, n_c can be calculated as[17]

Bulk & Surface sensitivity of MRR

$$\frac{\partial\lambda_{on-res}}{\partial n_c} = \frac{\partial n_{eff}}{\partial n_c}.\frac{\lambda_{on-res}}{n_g} \tag{2.81}$$

If the cladding layer is a bioreceptor layer, the shift is induced by a small change in the layer thickness, t_{bio}. Analogously, the surface sensitivity can be calculated as[17],

$$\frac{\partial\lambda_{on-res}}{\partial t_{bio}} = \frac{\partial n_{eff}}{\partial t_{bio}}.\frac{\lambda_{on-res}}{n_g} \tag{2.82}$$

Heideman et al.[17] used through port drop response to calculate λ_{on-res} because the through response has sharper slope than the drop response and solving the second order derivative of $P_{through}$ with respect to wavelength ensures λ_{on-res} as a local minima[17]. For bovine serum albumin (BSA) solution, they demonstrated a surface sensitivity of 229 pm.

Now, the operating principle of silicon *photodiodes* are discussed focusing on certain optical characteristics that are relevant to the work in the thesis. To define, silicon photodiodes are semiconductor devices that produces a current in the external circuit proportional to the incident optical power. Photodiodes are capable to detect the presence or absence of minute amount of light ranging from intensities below $1pW/cm^2$ to intensities above $100mW/cm^2$[43]. From a structural point of view, p-n junctions and planar diffused silicon photodiodes are very much comparable. Fig. 2.8(a) shows the schematic of a Si photodiode. In N-type bulk silicon, diffusion of P-type impurity forms a p-n junction. The P-type impurity diffused area is known as the active region of the photodiode. To create ohmic contact, the other end of the photodiode has to be doped with impurity type opposite to the active region, i.e. N^+-type. A channel with metal contact to P^+-type region forms the anode, while the complete back surface is plated

Photodiodes

Structure of Si photodiode

with metal contact to create cathode. Si has bandgap energy of 1.12 eV at room temperature. At absolute zero, the valence band is filled with electrons and the conductance band is empty. As temperature increases, thermal energy excites the electrons of the valence band to jump to the conductance band. This required energy can also be provided by photons. In case of Si, this corresponds to the photons with wavelength smaller than 1100 nm. The electron in the conductance band, thereby, contributes to the current generated by the photodiode. However, the diffusion of electrons from N-type to P^+−type and holes from P^+−type to N-type can develop built-in voltage. This built-in voltage is maximum at the junction interfaces and is absent outside the depletion region. The diffused region, thus, has no free carrier and is referred to as *depletion region*. The photodiodes are operated in reverse bias mode for ensuring a wide depletion region. Any increase in the operating voltage contribute to the built-in potential. When the incident photons are absorbed, the drift in the depletion region sweeps the generated electron towards the undiffused region. The absorption of photons is wavelength dependent. For shorter wavelength, the absorption coefficient is higher than for longer wavelengths. Moreover, the photons should have enough energy to be absorbed.

Depletion region

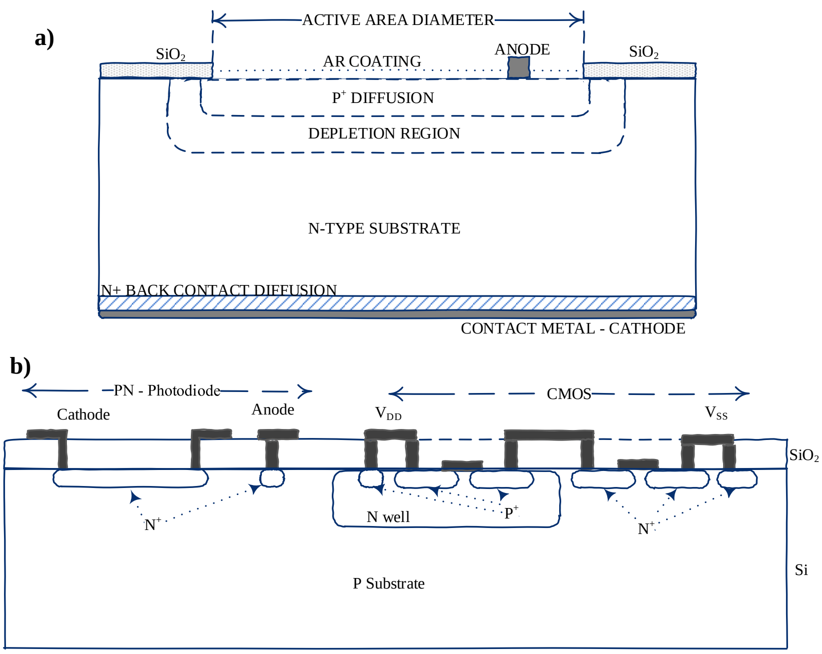

Figure 2.8: Realization of Si photodiode in CMOS technology. a) Schematic Representation of Si photodiode, b) Schematic cross section of a PN photodiode integrated in a one-well CMOS chip

The quantum efficiency, η $(0 < \eta < 1)$ is the probability of a single photon generating photocarrier pair that contributes to the detector current. When light is incident on the photodiode, not all the photons are absorbed. Some photons simply do not get absorbed due to the probabilistic nature of the absorption process. Moreover, the photocarriers generated by the absorbed photons may recombine as soon as they are generated due to the abundance of the recombination sites. The quantum efficiency, thus, can be expressed mathematically as[41],

Quantum efficiency of photodiode

$$\eta = (1 - R)\zeta[1 - e^{-\alpha d}] \tag{2.83}$$

where, R is the reflectivity of the active region surface, ζ is the fraction of photocarrier pair that contribute to the detector current, α is the absorption coefficient of the material and d is the depth of the photodetector. Out of the three multiplicands, only ζ successfully contributes to the detector current. On the other hand, *responsivity* relates the generated current to the incident optical power. If all the incident photons were to generate photcarriers, then a photon flux of ϕ will generate an equal current flux ϕ with an amplitude of $e\phi$. For the optical power, $P = h\upsilon\phi$, the generated current is equal to $\frac{eP}{h\upsilon}$. Therefore, we can write[41]

Responsivity of photodiode

$$i_p = \eta e \Phi = \frac{\eta e P}{h\upsilon} = \Re P \tag{2.84}$$

where, $\Re$ is called the responsivity of the detector and is expressed in A/W and is given by[41]

$$\Re = \frac{\eta e}{h\upsilon} = \eta \frac{\lambda_0}{1.24} \tag{2.85}$$

Responsivity increases with the increasing wavelength, since the same amount of photons with increased wavelength will have more optical energy, P. Exposing photodetectors to excessive optical energy drives the diode into saturation. This phenomenon is known as detector saturation, and at this point, the diode no longer operates in its dynamic linear regime. Nevertheless, the minimum incident power required to produce a photocurrent equal to the total noise current is known as *noise equivalent power* (NEP). Since the incident optical power is different at different wavelength, NEP is always quoted at a certain wavelength. Shot noise due to the dark leakage current and Johnson noise arising from the shunt resistance of the diode at ambient temperature contributes to the total noise current. Shot noise due to the leakage current can be written as follows[41],

Noise equivalent power of photodiode

$$i_s = \sqrt{2ei_d\Delta f} \tag{2.86}$$

where, i_s is the shot noise current, e electronic charge, i_d dark leakage current expressed in amps, and Δf the bandwidth of system. Johnson noise is the thermal noise that is generated at the shunt resistance of the device and is given by[41]

$$i_j = \sqrt{\frac{4kT\Delta f}{R}} \tag{2.87}$$

where, i_j is Johnson noise current, k Boltzmann constant, T absolute temperature in kelvin, and R is the resistance giving rise to noise. The total noise current is then[41]

$$i_N = \sqrt{(i_s^2 + i_j^2)} \tag{2.88}$$

and NEP is given by[41]

$$\text{NEP} = \frac{i_N}{\Re} \tag{2.89}$$

If input power is divided by NEP, it results in Signal to Noise ratio (SNR)[44]. Thus, SNR can be calculated from the value of NEP quoted at certain wavelength and the corresponding input power at that wavelength.

For constructing a simple CMOS optoelectronic integrated circuits (OEIC), one needs to make the use of the available the PN junctions in CMOS processes namely, source/drain-substrate, source/drain-well, and well-substrate diodes[45]. But these PN photodiodes own electric field free regions. The transient behaviour of these kind of PN photodiodes is determined by the slow diffusion of photogenerated carriers in these regions[45]. Fig. 2.8(b) illustrates a N^+/P-substrate photodiode. In spite of being more convenient to detect wavelengths shorter than 600 nm, the well-substrate photodiode is found to be more pragmatic for long wavelengths like

Structure of OEIC

780 nm or 850 nm instead of the source/drain-substrate and source/drain-well photodiodes[43]. However, the dynamic behaviour of the PN photodiode is limited by the carrier diffusion. Furthermore, large junction capacitance as well as the series resistance from lateral anode contacts at the silicon surface curbs the dynamic behaviour. In a N-well process, the anode of the N^+/P-substrate photodiode has to be at V_{SS} potential.

Slew rate

Finally, some definitions of the important terms regarding the data acquisition electronics are presented that will be used frequently in the context of the work. After the optical signal is converted into electrical signal, some internal amplification might be required to adjust the low output of the photodiodes to a desired level. However, there exists a limit beyond which the signal is no longer considered as small signal and the amplifier no longer operates within its dynamic range. This limit is known as the *slew rate* limit of the op-amp. Slew rate generally limits the highest rate of change in the amplifiers output signal. It arises from the capacitors inside the amplifier since there is a finite amount of current available for charging and discharging[46]. If the input signal is sinusoidal, the maximal rate of change happens at the point of zero crossing. The slew rate can then be expressed as[46]

$$V_0 = V_p \sin(2\pi f t) \tag{2.90}$$

$$\frac{dV_0}{dt} = 2\pi f V_p \cos(2\pi f t) \tag{2.91}$$

$$\left.\frac{dV_0}{dt}\right|_{t=0} = 2\pi f V_p \tag{2.92}$$

$$S_r = 2\pi f_{max} V_p \tag{2.93}$$

Here, V_0 is the output voltage and V_p is the peak output voltage. In the context of this work, the slew rate increases with actual photodiode current. The higher the current, the higher the slew rate.

Sampling rate

The amplified signal is then sent to the data acquisition card that samples the incoming signal and converts it to digitized bits for the computer to process. The rate at which the incoming signal is sampled, or the output signal is produced by a device is known as *sampling rate*. A fast sampling rate can acquire more datapoints in a given timeframe and thus can represent the input signal better than a slower sampling rate. Excessively slow sampling will conclude in the inadequate portrayal of the incoming signal. Undersampling will cause the signal to appear having a different frequency than it actually does. This phenomenon is known as aliasing[47]. On the other hand, when the signal reaches Analog to Digital Converter (ADC), the continuous time signal is digitized to a discrete time signal. The transfer function of ADC is staircase shaped and for each output code, the input signal produces a same value for a certain range.

Quantization error

This range is known as *quanta* (Q) and corresponds to the least significant bit (LSB). If the input signal level is within 0 to V_{ref} and the ADC has N number of bits, quanta is then calculated as[47]

$$Q = \frac{V_{ref}}{2^N} \tag{2.94}$$

The difference between the incoming and the outgoing signal of ADC is known as *quantization error*, the rms value of which can be written as[47]

$$i_{qn} = \frac{Q}{\sqrt{12}} \tag{2.95}$$

Therefore, the range of quantization error an ADC can have is $\pm\frac{1}{2Q}$. The input rms voltage can be calculated as[47]

$$V_{RMS} = \frac{2^N Q}{2\sqrt{2}} \tag{2.96}$$

Now, the signal to noise ratio (SNR) can be calculated from the input rms voltage and rms noise as follows[47]

$$SNR = 20\log\left(\frac{V_{RMS}}{i_{qn}}\right) \tag{2.97}$$

Replacing Eqn. 2.95 and 2.96 into Eqn. 2.97 results in

Signal to Noise Ratio of ADC

$$SNR = (6.02N + 1.76)\ \text{dB} \tag{2.98}$$

Eqn. 2.98 is generalized for any system with digital representations.

2.5 ROBUSTNESS TOWARDS DISTURBANCES

Error analysis

Uncertainties are dominant in the measurements of almost all the physical quantities. Accurate and precise approximation of the truest value thus becomes the focal point while performing measurements. Minimizing the uncertainties results in reduced error, which is sought for to the greatest attainable extent. In broad sense, errors can be segregated into two tiers, namely systemic error[48], that impacts the accuracy of the measurement arising from the instruments, procedural and personal bias, and random errors, in the form of white noise affecting the precision of the measurement.

Mean squared error

There are several ways to represent the error. For quantifying the goodness of the detection scheme described in Section. 2.2 (since here, the overall performance of the system is perceived), some of the statistical terms are used. To begin with, in regression analysis, the term *mean squared error* (MSE) is referred to the unbiased estimate of error variance. The computed MSE of a predictor can have diverse meaning when various denominators are exploited. This variety of denominators is generally of two kinds - $(n-p)$ and $(n-p-1)$, where n and p is the size of the sample and the number of parameters in the sample respectively. Out of these two, the former is used for regressors and the later is employed for intercepts. Under the consideration of this work, $\mathbf{p}$ parameter is a vector of n for a model of m datapoints which is estimated for an intercept of a minima. Since, Jacobian represents the local sensitivity of a function, i.e. variance with respect to $\mathbf{p}$, we can express Eqn. 2.6 as follows[27]:

$$\sigma_y^2 = \frac{1}{m-n+1}(y - \hat{y}(\mathbf{p}))^T(y - \hat{y}(\mathbf{p})) \tag{2.99}$$

Parameter covariance matrix

After the determination of the optimum curve-fit parameters p_{fit}, the regression statistics can be gauged with the application of weight values, w_i^2 to see whether or not the parameters are converged to a solution. The value of w_i^2 equal to the predicted square error is assigned as follows[27]:

$$w_i^2 = \sigma_y^2 = \frac{1}{m-n+1}(y - \hat{y}(\mathbf{p}_{fit}))^T(y - \hat{y}(\mathbf{p}_{fit})); \forall i \tag{2.100}$$

Calculation of the parameter covariance matrix follows as such[28]

$$\mathrm{Cov}(\mathbf{p}) = [J^T W J]^{-1} \tag{2.101}$$

where the right hand side of the equation is the inverse of the Hessian. The estimates' covariance matrix is the inverse of the Hessian in an asymptotic manner in cases of likelihood maximization[49]. For real-valued random variables X and Y with means $E(X)$, $E(Y)$ and variances σ_X^2, σ_Y^2, respectively, the covariance of (X, Y) is defined by[28]

$$\mathrm{Cov}[X, Y] = E([X - E(X)][Y - E(Y)]) \tag{2.102}$$

and the correlation of (X, Y) is defined by[28]

$$\mathrm{Cor}(X, Y) = \frac{\mathrm{Cov}(X, Y)}{\sigma_X \sigma_Y} \tag{2.103}$$

Covariance can be considered as being adjusted and expressed as correlation because of the identical sign of the parameters. Depending on the sign, the variables are called either having positive correlation or negative correlation, and uncorrelated if the sign is 0. However, a high sample correlation coefficient does not suggest that the variables are well connected. In fact, it is a method which dictates how strong the linear relationship is between the variables[28]. On the other hand, the asymptotic standard parameter error is a benchmark for measuring the error in the parameters. It tries to find a relationship between the data inconsistency and the parameter irregularity. It is given by[27]

Asymptotic standard error of the parameter and the fit

$$\sigma_p = \sqrt{diag([H]^{-1})} \tag{2.104}$$

Similar to the definition of σ_p is the standard error of the fit. It signifies the effect of parameter inconsistency on the fluctuations observed in the curve-fit. It is given by[27]

$$\sigma_{\hat{y}} = \sqrt{diag(J[H]^{-1}J^T)} \tag{2.105}$$

Predicted square error

Predicted square error, $\sigma_{\hat{y}_p}$ is defined as the total of the squared error of the model under observation and the penalty of overfitting[50]. In the context of this work, Eqn. 2.106 reflects the standard error of the fit as well as the mean square measurement error as follows[27]:

$$\sigma_{\hat{y}_p} = \sqrt{\sigma_y^2 + \sigma_{\hat{y}}^2} \tag{2.106}$$

In this thesis, one systemic error and one random error is investigated and attempts were taken to minimize both of them. The identified systemic error arises from the temperature stabilization process. For controlling the temperature of the VCSEL as well as the MRR chip, a VCSEL oven and a Thermotable is used.

Temperature control system

The purpose of a temperature control system is to maintain a device at a constant temperature. Two types of actuators are commonly used to precisely control the temperature of optics, lasers, biological samples, or other temperature sensitive devices; namely, thermoelectric devices and resistive heaters. The later of the two does not incorporate any cooling function, Regardless of the direction of the current flow, a resistive heater only heats up. Absence of current flow lets the heater to dissipate heat in the ambient atmosphere. In the system, both for the oven and the Thermotable, *thermoelectric coolers* (TEC) are used. A TEC, like all other thermoelectric actuators, are based on peltier effect. Fig. 2.9(a) illustrates a typical TEC system. As the current flows, the heat is pumped from one plate to another. If the direction of the current flow changes, so does the direction of the heat pump. Therefore, a TEC device can heat up and cool down unlike resistive heaters. The TEC is sandwiched between the cooling plate and the heat sink. A temperature sensor is incorporated with the TEC system, which provides the feedback for the TEC to control the temperature. For a TEC device, three parameters have to be set prior to the operation. The first parameter, the maximum temperature, T_{hot} depends on the expected maximum ambient temperature, $T_{ambient}$ along with the heat sink capacity and efficiency, and is expressed in ^0C. The second parameter, the minimum temperature, T_{cold} is also expressed in ^0C but depends on the maximum deviation from the ambient temperature and the cooling plate geometry. The third parameter, heat absorbed at the cooling surface, Q_{cold} is the sum of active and passive heat loads expressed in watts. Active heat load is the power dissipated from the device when it is cooled down and is given by[51],

Thermoelectric coolers

Active & Passive heat load

$$Q_{active} = \frac{V^2}{R} = VI = I^2R \tag{2.107}$$

where, R, V and I are the resistance, voltage and current of the device respectively. On the other hand, passive heat loads refer to the leaky heat losses from either radiative, or convective, or conductive heat transfer. Generally, the passive heat loads are negligible. However, in the worst case scenario, the passive heat load can be calculated as[51]:

$$\begin{aligned} Q_{passive} &= Q_{rad} + Q_{conv} + Q_{cond} \\ &= F\epsilon\sigma A(T_{hot}^4 - T_{cold}^4) + hA(T_{hot} - T_{cold}) + \frac{kW}{L}(T_{hot} - T_{cold}) \end{aligned} \tag{2.108}$$

where, the shape factor is expressed as F, emissivity as ϵ, Stefan-Boltzman constant as σ, area of the cooled surface as A in m^2, convective heat transfer coefficient as h in $\frac{W}{m^{2\,0}C}$, thermal conductivity of the material as k in $\frac{W}{m^0C}$, cross-sectional area of the material as W in m^2 and the length of the heat path as L in m. For the shape factor and emissivity, the worst case value is regarded as unity.

Under usual conditions of the ambience, a positive manifestation of the system performance will be provided by the temperature coefficient of the controller. This measurement is usually specified in $^0C/^0C$ or $ppm/^0C$. The VCSEL temperature control system can be considered in four sections: the current limiter circuit, the error detector, the PID processor, and the output power amplifier as shown in 2.9(b). The limit circuit maintains inputs at a predefined level set by the user that is considered safe for the operation of the device. For the user input, it checks whether the set value is less than 40^0C and adjusts the current accordingly. On the other hand, the VCSEL temperature is passed through a CMOS level shifter circuit. A level shifter connects one digital circuit that uses one logic level to another digital circuit that uses another logic level. Next block is the error detector. Here, a differential amplifier calculates the difference between the setpoint and the sensed temperature, which is known as the *error term*. This error term is fed to the PID controller block. At any given sensor, the temperature range of the controller depends on the setpoint temperature range and the temperature sensor's amplifier gain. This gain along with the sensitivity of the temperature sensor defines the sensitivity of the error

Structure of VCSEL temperature control system

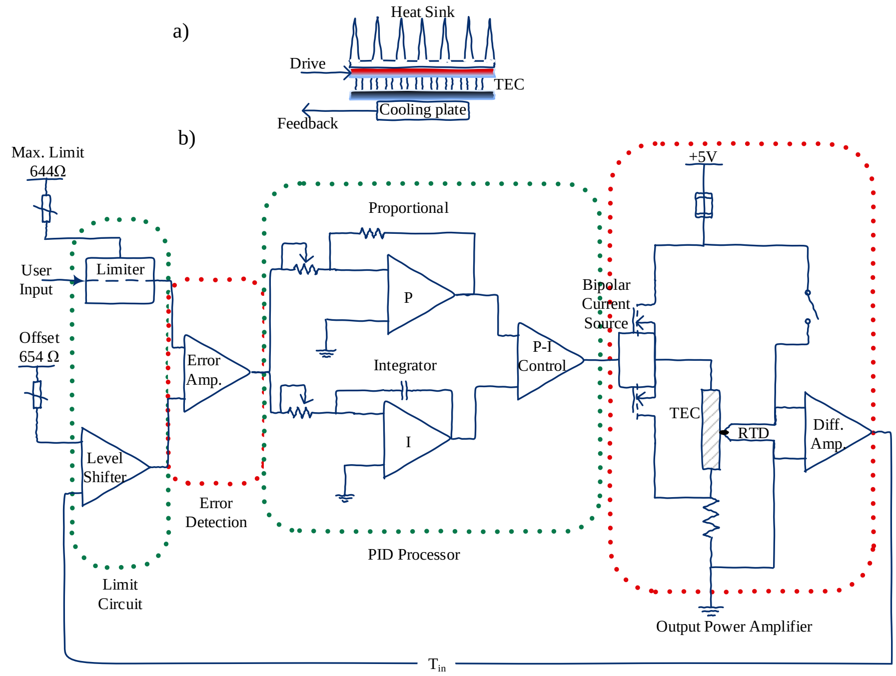

Figure 2.9: Block diagram of VCSEL Temperature Control. a) A simple thermoelectric control system, b) Block diagram of the temperature control system in OSROM

detector. After the error detection block, the next block is the PID processor. In the VCSEL temperature control, the PID processor comprises of proportional (P) gain amplifier and an integrator (I) circuit but excludes differentiator (D) circuitry. Generally, the integral time constant, I and the differentiator time constant, D are kept constant. Only the proportionality constant, K_c is varied. The proportional gain amplifier can operate for low gain with stability. However, a non-zero difference between the output and the error term must be kept since K_c determines and maintains the ratio between the output response and the error term. Increasing K_c will increase the system response time, however, if K_c is too large, output response will start to oscillate. This oscillation can even go out of control depending on the value of K_c. The integrator sums up all the error terms to make the difference between the output ad the error term zero. Even a small error term will make the integrator time constant, I to increase slowly. This time constant will rise until the difference is zero to nullify the steady state error. Steady state error is the difference between the setpoint and the process variable. Thus, inclusion of the integrator circuit makes the steady state error zero but decreases the loop stability. The integrator will produce a finite term even when the steady state error is zero due to its operation on the past error terms. These past error terms keeps the integrator charged up to produce a finite output. This phenomenon is known as *integral windup*[47]. PI or PID controller should be chosen such that it contains adaptive circuitry to compensate for the integral windup. The differentiator, on the other hand, makes the damping coefficient zero and thus increases stability of the loop. The dynamic response as well as the stability of the processor can be set with the constants of P, I and D. Generally, increasing K_c and decreasing I reduces error. On the contrary, increasing both I and D, increases loop stability[52]. The steady state error from the PID processor is then fed to the output power amplifier block. In the system, the TEC is driven by a bipolar current source and thus, the heating and cooling by changing the direction of the current flow is possible. After pumping the heat from the cooling plate to the heat sink, the temperature at the cooling plate is determined by a temperature sensor. These sensors can either have a positive or a negative temperature coefficient based on which, these precision sensors are divided

PID controller

Integral windup

into two categories. The negative temperature coefficient (NTC) sensors, e.g. thermistors, are very sensitive (hundreds of ohm per ^{0}C), and are miniaturized to precisely mount as a bead. However, the relationship between the resistance and the temperature is nonlinear and the temperature range is $\approx 50^0$C for the NTC sensors. These disadvantages of the thermistors can be well addressed by the positive temperature coefficient sensors like platinum and copper resistive temperature detectors (RTDs). RTDs have less sensitivity than the NTC sensors (fraction of an ohm per ^{0}C) and used in the system that requires temperature control no better than 0.05^0C. Typical accuracies for a $100W$ platinum RTD are $\pm 1.3^0$C at the range limits, and $\pm 0.5^0$C within the mid range. Additionally, some systems exhibit an undesirable behaviour called *deadtime*. Deadtime is a delay between when a process variable changes, and when that change can be observed. It can also be caused by a system or output actuator that is slow to respond to the control command[51], for instance, during integral windups, the PI controller responds slowly.

Deadtime

The remaining source of error is the noise present in the signal. For the purpose of denoising the signal, a filter operation was implemented on the input data. Since the data is nonlinear, a running median was implemented as a nonlinear smoother for time-series data. To define a median smoother, let $X(.)$ be a discrete time series data. A median smoother selects n odd consecutive datapoints at instant n for building the observation point $X(n)$. The observation window at instant n will have the following form[53],

Nonlinear median filter

$$X(n) = [X(n - N_L), \dots, X(n), \dots, X(n + N_R)]^T \tag{2.109}$$

where, N_L and N_R are positive integers and the total window length is $N = N_L + N_R + 1$. To maintain symmetry, $N_L = N_R = N_1$ is preferred. The output $Y(n)$, at instant n, then results in[53]

$$\begin{aligned} Y(n) &= \mathrm{MEDIAN}[X(n - N_1), \dots, X(n), \dots, X(n + N_1)] \\ &= \mathrm{MEDIAN}[X_1(n), \dots, X_N(n)] \end{aligned} \tag{2.110}$$

where, $X_i(n) = X(n - N_1 - 1 + i)$ for $i = 1, 2, \dots, N$. So, the median smoother sorts the data first in the observation window and then take the median or the middle value as the output. If $X_{(1)}, X_{(2)}, \dots, X_{(N)}$ are sorted, the output of a median smoother will look like[53]

$$Y(n) = \begin{cases} X_{\frac{N+1}{2}} & \text{if N is odd} \\ \dfrac{X_{\frac{N}{2}} + X_{\frac{N}{2}+1}}{2} & \text{otherwise} \end{cases}$$

For symmetry, the observation window extends equally on the both sides of the observation point. But at the first and the last datapoint, half of the window will be vacant. To address this problem, a median smoother generally adds up N_L datapoints before the first datapoint and N_R datapoints after the last datapoint. Though these appended data points can be arbitrarily chosen, in practice, the appended N_L and N_R datapoints are chosen such that they are equal to the first and last datapoint respectively. A median smoother can be operated at recursive mode as well. In such instance, the output of a recursive median filter is given by[53]

Observation window

$$Y(n) = \mathrm{MEDIAN}[Y(n - N_L), Y(n - N_L + 1), \dots, Y(n - l), X(n), \dots, X(n + N_R)] \tag{2.111}$$

In contrary to the normal median filter, a recursive median filter updates the observation window on the basis of the previously calculated median values. Thus, a recursive median filter shows better noise attenuation than operating in non-recursive mode. Alternatively, recursive

Running vs. Recursive median smoother

median filters require smaller window size to attain desired noise attenuation level[53]. Moreover, for the same level of noise attenuation, a recursive median filter shows less signal distortion. These deterministic properties of the median smoothers, in general, can be verified with their statistical counterparts in terms of optimality and variance of the output distribution. Here, a case of white noise is considered. Generally, it is assumed that the signal is constant and white noise is added to it. Then, the asymptotic mean, μ_{median}, and variance, σ^2_{median}, of the output distribution of a median filter is given by[53],

Statistical properties of median filter

$$\mu_{median} = t_{0.5}, \tag{2.112}$$

and

$$\sigma^2_{median} = \frac{1}{4N(f_x(t_{0.5}))^2} \tag{2.113}$$

where, $t_{0.5}$ is the median parameter of the input distribution. It can be easily deducted from Eqn. 2.112, that the mean, μ_{median} always produces a consistent and unbiased estimate of the median of the input distribution. This satisfies the optimality conditions. In case of output variance, it is not proportional to input variance directly but as $\frac{1}{f_x(t_{0.5})}$. Therefore, the more the variance is observed in the input distribution, the less will be the output variance. However, for heavy tailed noise, output variance becomes proportional to the impulse amplitude but not to $\frac{1}{f_x(t_{0.5})}$.

To conclude, a median filter is a nonlinear smoother in the sense that the superposition theorem does not apply on the output distribution of a median smoother, and impulse analysis is not rigidly relevant[53]. In fact, a median filter has nullified impulse response consistently. Thus, unlike linear filters, median smoothers adhere to their deterministic properties as well as the statistical ones.

2.6 SUMMARY

This chapter discusses, in detail, the theories required for the optimization process, which is carried on consecutively. It starts with the choice of fit algorithm and fit function to optimize the detection algorithm. Next, the operating principle of VCSELs, MRR, MZI and photodiodes are discussed. Following, the terminologies used in the context of data acquisition electronics are defined. Finally, the parametric statistics that will be used to evaluate the system are plotted out and two considered source of noise was analysed. Corresponding literature review was also presented to keep abreast of scientific developments.

3

LOGICAL SYSTEM DESIGN

3.1 INTRODUCTION

In the complete detection system architecture, an application called 'MRR vX.0' performs the complete processing of the acquired data through the DAQ card. This run time engine is built from LabVIEW and coded in G language environment by Dr. Ir. F. Schreuder. According to the National Instruments official website[54], *"LabVIEW is a highly productive development environment for creating custom applications that interact with real-world data or signals in fields like science and engineering"*. The net result of using LabVIEW is higher project quality with less time and man-power. So productivity is the key benefit. Also, the wide range of hardware support makes this program an attractive tool for developing complicated systems involving multiple hardware simultaneously. MRR v10.0 was selected as the starting point for further development through the course of the thesis assignment. This chapter focusses on the design approaches taken, mainly for the peak detection schemes as well as the interdependencies observed.

3.2 PEAK DETECTION ALGORITHM

Real-time peak detection requires high resolution measurements, which involves less computational time. Most of the time required in this aspect arises from the fitting operation. In other words, an efficient fit operation is an attractive choice for determining the peak position in real-time with high accuracy. In the context of this work, the choice for fitting a desired function to a set of acquired data was Levenberg-Marquardt (Lev-Mar) algorithm. This method is used for non-linear least square curve fitting problems.

Complete detection scheme

Fig.3.1 demonstrates the full detection scheme. This is one of the sub-programs within the mother application. It starts by acquiring the data read by the DAQ card at a predefined sample rate and scanning frequency. This data bundle, apart from the Drop port signal data, wavelength and boundary conditions[55], may include timestamps, temperature readings, VCSEL driving current and voltage, modulation information as well as global parameter values. Only the required data for the detection scheme is unbundled and used as variables, both dependent and independent, throughout the process. For faster processing of the data, the complete dataset is divided into two unequal sets named according to their position from the mean of the data-point number. Previously, there was a correction operation on the Left Hand Side (LHS) dataset on the basis of the VCSEL driving current value. It used to crop out the data values in the Drop and Through signal as well as from the wavelength that corresponds to the current values lower than 1.3 mA. Strictly speaking, the correction operation shortened the LHS range because of the former choice of using $\frac{\mathtt{Drop}}{\mathtt{Through}}$ signal for finding the position of the peak. The new approach takes into account two factors that makes this correction operation redundant. Firstly, the whole detection scheme now relies on Drop signal only, the reason of which is validated in the author's internship report[55]. Secondly, the VCSELs used in the OS-ROM have $I_{threshold}$ greater than or equal to 2.0 mA. Properly characterized values, which are determined in Section4.2, assures the absence of incoherent lasing response of the VCSEL. The new approach, on the contrary, applies a median filter to denoise the Drop signal. After these preprocessing steps, the complete dataset is divided according to the unequal range values to get the LHS and RHS data sets. This asymmetrical division rules out the sharp discontinuity that arises from the symmetrical boundary conditions. In other words, it serves the purpose of continuity correction that is required for smooth processing of the data[55].

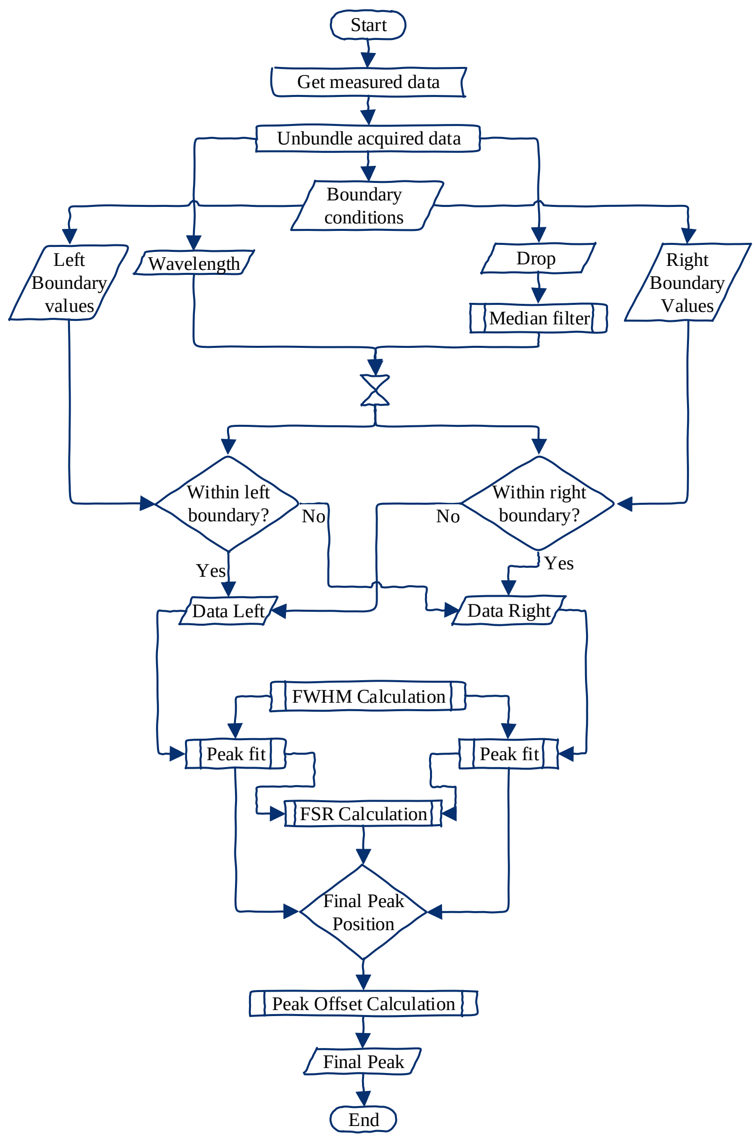

Figure 3.1: Detection Scheme for the Resonance Peak of the Micro Ring Resonator

Next step involves fitting operation. There is a trade-off present in fitting operation: more data points will ensure increased accuracy but with higher computation time. Full Width Half Maximum (FWHM) is found to be optimum in such case[55]. Instead of fitting the complete data set, this approach now fits the $\max(\text{Drop})$ of each dataset within its corresponding FWHM range parallelly. The selection of proper peak within the wavelength range is decided afterwards with the calculated FSR. If the peak(s) is static, FSR and Peak offset calculation does not play any role. On the contrary, when there is either a clockwise or an anti-clockwise shift relative to the static peak position, these two calculations ensure the correct detection of peak position when the peak is moving. The sub program reaches its end after determining the final peak position. This peak position data is used later in other sub programs such as data saving and shift calculation.

Now, let us look deep into the detection scheme described above, explicitly peak fit, FSR calculation and Peak offset calculation. To begin with, the choice for peak fitting operation was Lev-Mar Algorithm.

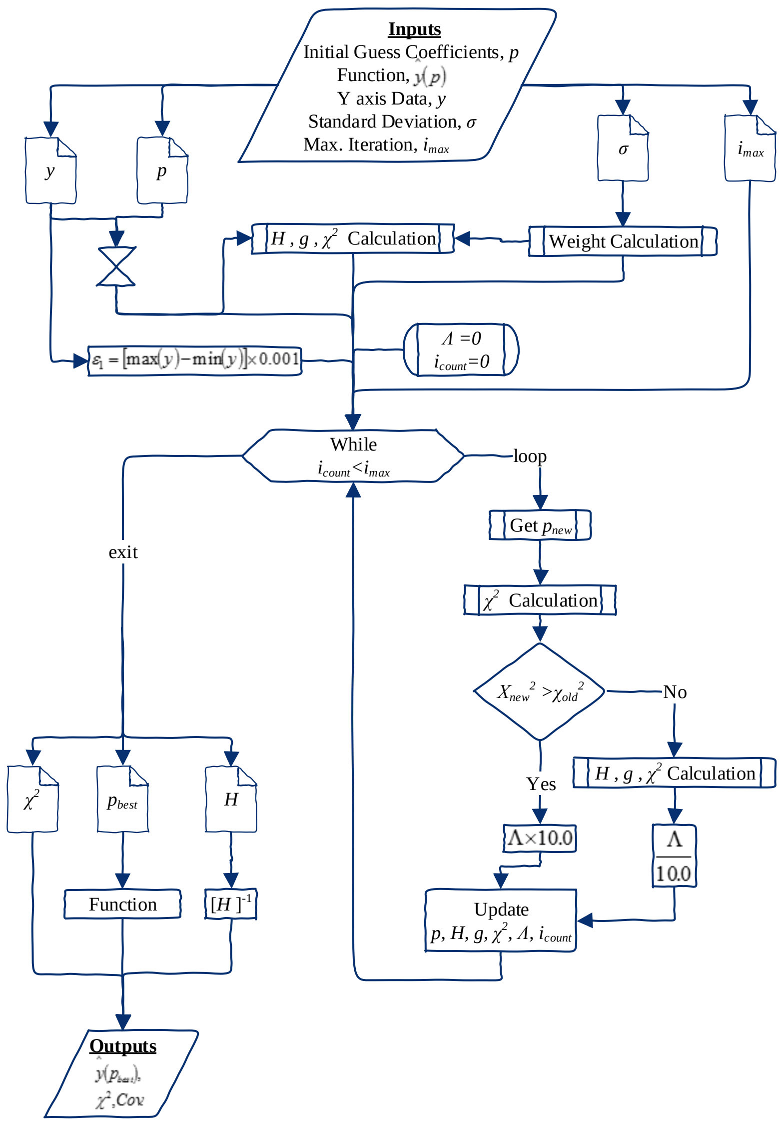

Figure 3.2: Implementation Scheme of the Levenberg-Marquardt Algorithm

Fig.3.2 illustrates the implementation of this algorithm. This algorithm takes initial guess coefficients, p, fitting fuction reference, $\hat{y}(p)$, Drop signal as dependent variable - considered as y axis data, y, standard deviation, σ and maximum iteration number, i_{max}. σ facilitates the computation of *weight* as shown in Fig. 3.3.

Implementation of Lev-Mar Algorithm

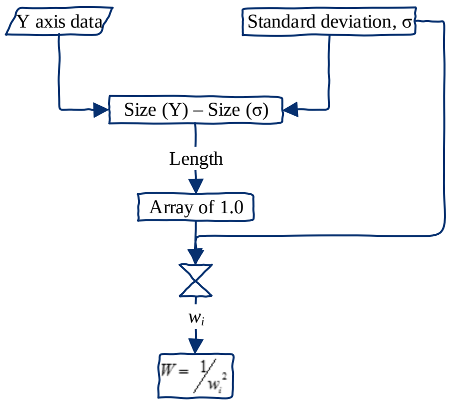

Figure 3.3: Weight Calculation Scheme from Standard Deviation

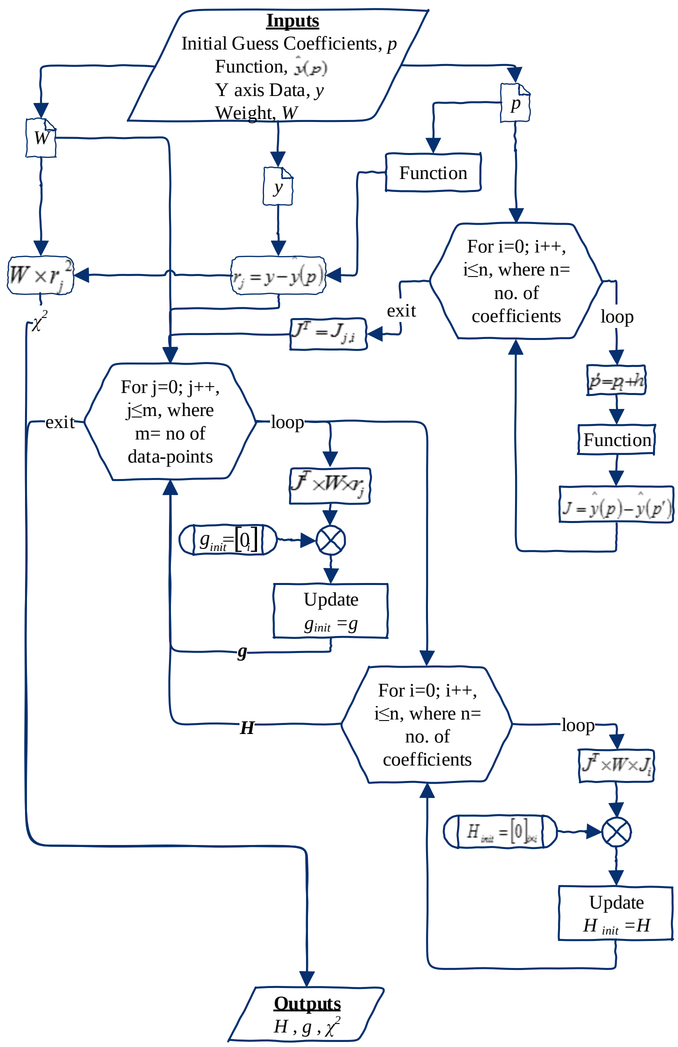

Figure 3.4: Calculation Scheme for the Hessian, Gradient and Chi-squared

First, the size of y and the size of point by point standard deviation is compared and the difference in length between these two is filled up with unity value. Since there are two methods of calculating σ that result in a size of either n or $(n-1)$ datapoints, equating the size of the σ array with 1 ensures that each y data point has a corresponding *weight factor*, w_i. The inverse

Weight calculation

of the squared value of w_i is considered as *weight*. If no σ is provided, then the *weight* is an unity array. This *weight*, p, and y acts as inputs for the calculation of Hessian, H, Gradient, g, and χ^2 on the basis of the initial guess parameters provided. These values along with y, p and update parameters λ and ϵ_1 undergo an iterative process either till it reaches the convergence or i_{max}. During the iteration process, it selects a new set of parameters on basis of H, and J and calculates the corresponding χ^2 value. If this new value of χ^2 is greater than the previously determined χ^2, it searches for a better set of parameters by increasing λ by a factor 10. Oppositely, it calculates a new set of H, g, and χ^2 values, decreases λ by a factor of 4 and keep looking for a more optimum set of parameters. ϵ_1 is the convergence value that determines whether or not the convergence is achieved. If any of the above mentioned reasons for the termination of the iteration process takes place, the iteration outputs the corresponding χ^2, $p_{optimum}$ and H. This optimum parameter values, $p_{optimum}$ gives the fitted model y data, and along with χ^2 and covariance as the inverse of H[49], make up the outputs of this algorithm.

Calculation of Hessian, Gradient and Chi-squared

Fig.3.4 shows the calculation of the Hessian, Gradient and chi-squared - values, which are used frequently in Fig. 3.2. Taking p, y, reference path for $\hat{y}(p)$ and W as inputs, residual, r_j is calculated from the difference between y and $\hat{y}(p)$, squared value of which is multiplied with W to get the value of χ^2. For the calculation of Jacobian, J, a small perturbation, h is added with each parameter and corresponding $\hat{y}(p')$ is calculated. The difference between $\hat{y}(p)$ and $\hat{y}(p')$ arises for the addition of h to the original parameter and subsequently called the Jacobian of $\hat{y}(p)$. Since we only require the transposed value of J for the calculation of the Hessian and the Gradient, the calculated Jacobian is then transposed to get J^T and multiplied with W. The product of this multiplication, when multiplied element-wise with r_j, gives the Gradient g. For each g, the Hessian H corresponds to the product of the element-wise Jacobian multiplied with this product. Combining the values of g and H with χ^2 completes the set of outputs.

FSR Calculation

Determining Free Spectral Range (FSR) in real-time is a tricky job. It requires the presence of two peaks within the detection range simultaneously - at least for once, so that the difference between their relative positions can be calculated. Fig. 3.5 shows the flow chart for determining the FSR. The calculation starts with a decision on the presence of multiple peaks. If more than one peak is present, two ranges are calculated from the difference of Left and Right Lower Range and Left and Right Upper Range. The data points of y and λ which fall within these ranges are considered for further operations whereas the rest of data are discarded. In each range, the difference between $max(y)$ and $min(y)$ is compared for clear distinguishability. If this property is present within the data range, the value of λ corresponding to $max(y)$ is selected as the peak wavelength of the respective range. The difference between these two peak wavelengths is recorded as FSR. Here, for all negative response to the decision steps, a predetermined value is recorded as FSR.

Peak Offset Calculation

Finally, Fig. 3.6 gives an overview of the calculation scheme of the Peak Offset (PO) and the determination of the peak position. Similar to FSR calculation, this scheme also starts with the decision on the presence of multiple peak. If single peak is present, PO is set to the default value of 0 and peak is the summation of PO and Final Peak position (FPP). As seen in Fig. 3.1, FPP is the outcome of the decision operation on the left and right peak determined from respective fitting operation. On the other hand, if multiple peaks are present, PO and peak is determined on the basis of the mode number. Mode number, m indicates whether the peak movement is anti-clockwise - denoting -1, clockwise - denoting 1 or static - denoting 0. When there is no movement associated with the peak, the value of PO and peak are calculated in the

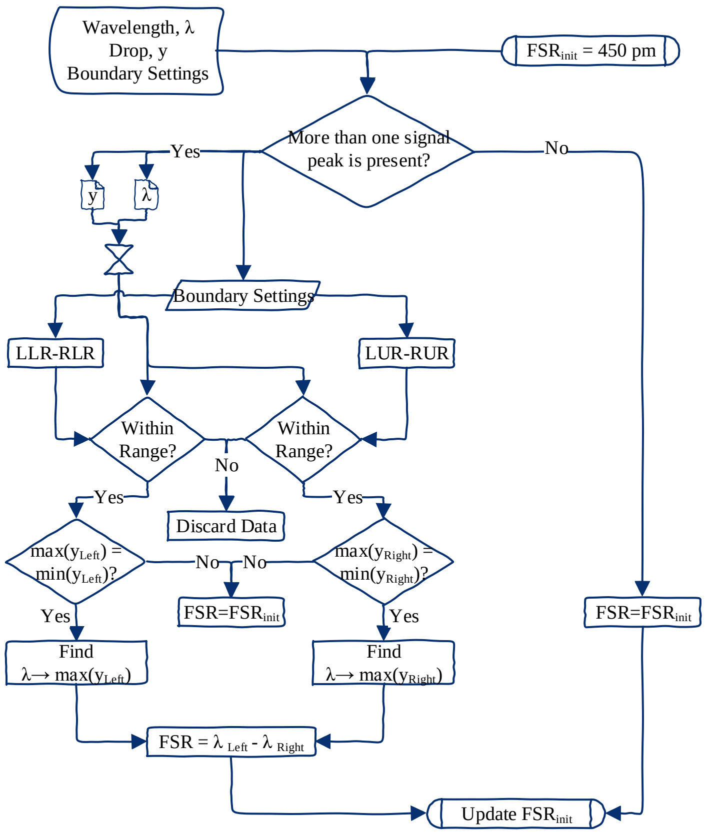

Figure 3.5: Calculation Scheme for the Free Spectral range (FSR)

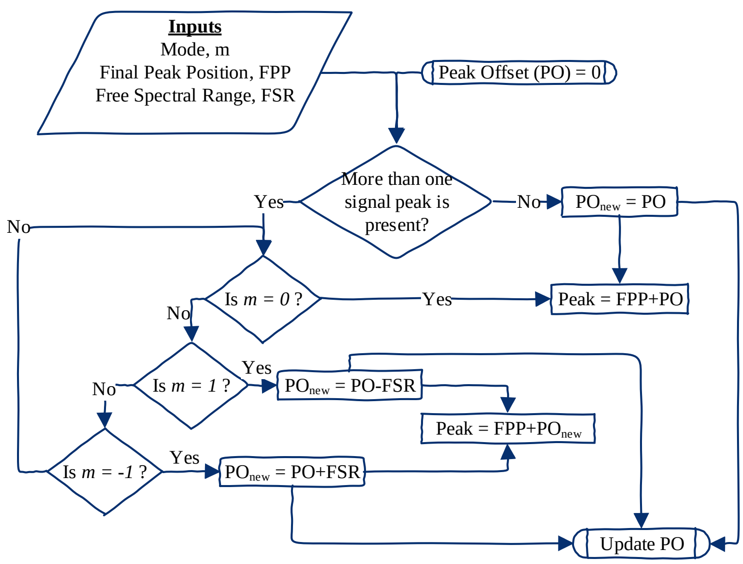

Figure 3.6: Calculation Scheme for Peak Offset (PO) and Determination of Peak

previous manner. If there is movement, PO is either the difference between, or the summation of PO and FSR. Peak, in all the cases, is the summation of FPP and PO.

CHANNEL NAME	CHANNEL NUMBER
VCSEL Current	1
VCSEL Voltage	14
Drop	2, 4, 6, 8
Through	3, 5, 7, 9
VCSEL Temperature	10
VCSEL Setpoint	12
External Temperature	11
External Setpoint	13
Total number of channels	14

Table 3.1: Channel Assignment

3.3 FUNCTION INTER-DEPENDENCY OPTIMIZATION

There is always electronic bottleneck present while converting signal from optical regime to electronic domain. Thus, the number of channels to read has significant effect on data acquisition and monitoring. For instance, Fig. 3.7 shows this effect on VCSEL temperature monitoring. Table. 3.1 lists the channel number and the corresponding variable they are used for whereas Table. 3.2 shows the switched off channel number at different alphabetical timestamps used in Fig.3.7.

VI interdependency

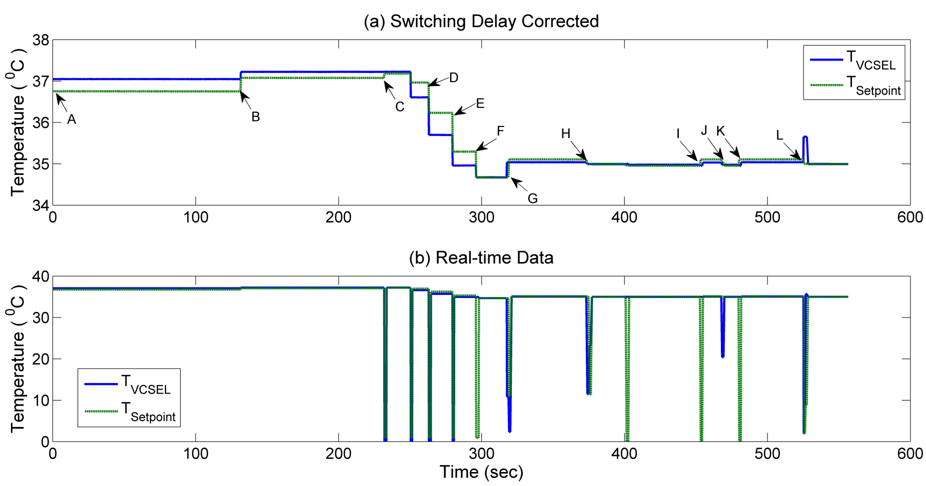

Figure 3.7: Effect of channel switching on VCSEL temperature monitoring

The experiment starts with all the available 14 channels in ON state. The setpoint temperature of VCSEL was kept at 35^{0}C. But with all channels on, the setpoint is approximately 36.75^{0}C. At point B, voltage measurement channel was switched off, which further increases the temperature to 37^{0}C. This is the only channel that increases the overall temperature when switched off. In case of others, switching off channels corresponds to decreased temperature up to 34.95^{0}C which is seen from step C till G. Up to point G, a set of channels were switched off and their switching delay more or less forces the monitored value close to zero. At point G, only three very basic channels are kept ON, namely Channel 1, 10 and 12. Here, setpoint temperature is 35.11^{0}C and the VCSEL temperature is 0.07^{0}C less than that of setpoint. This allows a room for the PID controller to have complete control over VCSEL temperature. To find the optimum channel settings, steps from H till K were introduced. At point H, only one Drop channel along with the channels in G is ON . A complete set of response channel combining

TIMESTAMPS USED IN FIG. 3.7	CHANNEL NUMBER													
	1	2	3	4	5	6	7	8	9	10	11	12	13	14
A	ON	ON	ON	ON	ON	ON	ON	ON	ON	ON	ON	ON	ON	ON
B	ON	ON	ON	ON	ON	ON	ON	ON	ON	ON	ON	ON	ON	OFF
C	ON	ON	ON	ON	ON	ON	OFF	ON	OFF	ON	ON	ON	ON	OFF
D	ON	ON	ON	ON	ON	OFF	OFF	OFF	OFF	ON	ON	ON	ON	OFF
E	ON	ON	ON	ON	ON	OFF	OFF	OFF	OFF	ON	OFF	ON	OFF	OFF
F	ON	OFF	ON	OFF	ON	OFF	OFF	OFF	OFF	ON	OFF	ON	OFF	OFF
G	ON	OFF	OFF	OFF	OFF	OFF	OFF	OFF	OFF	ON	OFF	ON	OFF	OFF
H	ON	ON	OFF	OFF	OFF	OFF	OFF	OFF	OFF	ON	OFF	ON	OFF	OFF
I	ON	ON	ON	OFF	OFF	OFF	OFF	OFF	OFF	ON	OFF	ON	OFF	OFF
J	ON	ON	OFF	OFF	OFF	OFF	OFF	OFF	OFF	ON	OFF	ON	OFF	OFF
K	ON	ON	OFF	ON	OFF	OFF	OFF	OFF	OFF	ON	OFF	ON	OFF	OFF
L	OFF	OFF	OFF	OFF	OFF	OFF	OFF	OFF	OFF	ON	OFF	ON	OFF	OFF

Table 3.2: Channel Switching Timestamps. *Red* denotes OFF whereas *green* denotes ON status

Channel number 2 and 3, shown as I, produces similar effect as G. Since, the interest is in Drop channel only, having two drop channel ON, shown as K, instead of a complete set as I produces similar effect as G. Finally, all the channels were switched off keeping channel number 10 and 12 in ON state. Only at this point, L, both the setpoint and the VCSEL temperature are 35^0C. Thus it can be concluded that for current chip readout scheme, keeping two drop channels ON is the optimum choice.

However, the reason behind these abrupt changes in VCSEL temperature controller while switching channel lies within the DAQ card. In the context of the above experiment, there are two phases while a change in channel is implemented. At first, the selection is made regarding a chosen channel for switching between ON and OFF state. Secondly, this value change in the channel state has to be updated manually by clicking the update button. The input and output configuration of the DAQ is discussed in Section 4.4. It is observed that when any change is made in the input or output configuration of the DAQ, it takes it into it memory buffer. Unless the memory buffer is cleared by pressing the update button, the DAQ operation is momentarily switched off. This is seen as the sharp cut off to zero in Fig. 3.7. Sharp cutoffs arising from channel switching were also observed in the case of real time shift calculation. Thus, in between the time a change is made and is updated, the DAQ read-out appears to be off. However, in case of VCSEL temperature oven presented above, a cut off means that the temperature is not controlled at that instance and after the update, it starts to control the temperature again. As discussed in Section. 2.5, this effectively changes the error term of the TEC. Therefore, the changes in the channel status shows a variation in the controlled as well as measured temperature.

Calculation of relative shift

It is often desirable to observe the *relative shift* if a reference ring is present. If a ring is passivated for a certain medium and the other ring is selective, i.e. a growth of selective layer on top of the ring, the shift of the selective ring relative to the passivated one is defined as *relative shift*. Fig. 3.8 demonstrates the implementation of the relative shift calculation. It takes

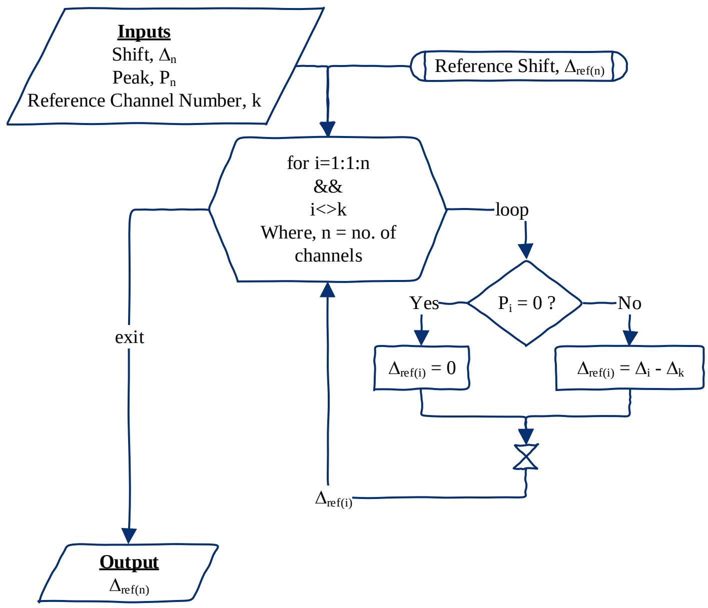

Figure 3.8: Implementation Scheme of Shift Calculation on the basis of the Reference Ring

shift, Δ_n, peak value, P_n and reference channel number, k set by the user as inputs and initiates a variable $\Delta_{ref(n)}$ for the calculation of the relative shift. For all the channels except k, it checks whether there are any peaks detected by the peak detection algorithm. If positive, it calculates $\Delta_{ref(i)}$ as the difference between the minuend Δ_i and the subtrahend Δ_k. On the contrary, it considers the corresponding channel is off if P_i is zero and sets the corresponding $\Delta_{ref(i)}$ to zero. After the iteration finishes, the output is the Δ_{ref} of all the channels. This algorithm was implemented and used in the measurements described in Chapter 5.

3.4 SUMMARY

This chapter discusses the design schemes and the parameter evaluations required for the logical system to determine the peak position optimally. It lays out the overview of the detection scheme first and then plots out the implementation scheme of the Lev-Mar algorithm along with FSR, peak offset and relative shift calculation. Next, the function interdependencies are discussed in terms of channel switching effect by monitoring VCSEL temperature. Based on this discussion, optimum channel setting parameters are proposed as well.

4

PHYSICAL SYSTEM CALIBRATION

4.1 INTRODUCTION

The accuracy of the detection system not only depends on an efficient detection algorithm but also relies on well calibrated equipments. The knowledge of calibration, when applied meticulously, can significantly reduce the non-linearities that arise from the natural processes (e.g. noise). Therefore, it becomes a requirement to be aware of the characteristic behaviour of the equipments used as well as the limitations that comes along. In the context of this work, the VCSEL, the VCSEL oven, the photodiodes , the DAQ card and the chip environment constitutes the *physical system*. The chapter starts with characterizing the laser in order to attain a sophisticated linear approximation for the current to wavelength conversion. This is presented in section 4.2. Next, the limiting factors - in terms of sensitivity, from the perspective of the photodiodes, and drift, from the viewpoint of VCSEL temperature control, are determined in section 4.3. Section 4.4 discusses the data processing limitations found in the DAQ card. Finally, two factors, namely temperature and evaporation of liquid measurand at a certain temperature, concerning the chip environment are investigated in section 4.5. The chapter ends with a short overview that sums up the works presented here.

4.2 VCSEL CHARACTERIZATION

There are two VCSELs from different manufacturers which were characterized for the purpose of this work. Ando AQ6317 Optical Spectrum Analyser (OSA) was used throughout the characterization process. $SS85-7U001P2$ is a $850nm$ polarized single-mode VCSEL chip manufactured by Optowell Co. Ltd. These chips were pigtailed locally after purchase and installed in the majority of the OSROMs. For this VCSEL, two step characterization was performed. Table. 4.1 presents a comparative view towards the settings used for characterizing both the laser at distinct charaterization processes. To begin with, the VCSEL was characterized over a broad range of temperature from 25^0C to 40^0C. Since the previous characterization provide us with the information on how the VCSEL behaves at 20^0C, this bulk characterization was a search for better operating temperature at the same step size of $0.2mA$ but at higher OSA resolution limit of $0.01nm$.

Characterization of $SS85-7U001P2$

Fig. 4.1 depicts the results of this bulk characterization. The spectrum can be divided into three regimes. Below the *threshold current*, $I_{threshold}$ of $2.0mA$, the spectrum declines gradually and levels out to a constant value. Since this regime does not contribute to the coherent lasing of the VCSELs, this regime was omitted for the linearization approximation. For $I_{threshold} > 2.0mA$, a steady climb till $4.5mA$ is observed for the entire spectrum of the temperature. Undoubtedly, this is the suitable regime for the linear approximation of current to

DEVICE	PARAMETERS		OPTOWELL			ULM
			PREVIOUS	CURRENT		
				BULK	SINGLE	
OSA	Resolution (nm)		0.5	0.01	0.01	0.01
	Averaging No.		10	10	1000	1000
	Span (nm)		1.0	0.5	0.5	1.0
VCSEL	Current(mA)	Range	$1.5-5.0$	$1.0-5.0$	$1.4-6.0$	$1.5-6.0$
		Step size	0.2	0.2	0.1	0.1
	Temperature(^0C)	Range	20	$25-40$	35	$25-40$
		Step size	0	1	0	5
Optical Fiber	Model No.		–	SM800G80	780HP	780HP
	Attenuation (dB/km)		–	< 5	< 3.5	< 3.5

Table 4.1: Specifications of VCSEL Characterization

wavelength and termed as *fit region*.When the current value is greater than $4.5mA$, the spectrum experiences a sharp rise for all temperatures. The change of wavelength corresponds to the change in driving current. As more current is injected in the active region, the cavity resonance changes. Since the VCSEL emission wavelength depends on the cavity resonance, a shift in the emission wavelength is observed for changing current. However, at higher currents, the abruptness is visible due to the internal heating of the VCSEL. Also, as temperature increases, the cavity resonator effective refractive index changes. Therefore, the resonance conditions is also changed and an increase of wavelength with increasing temperature is observed.

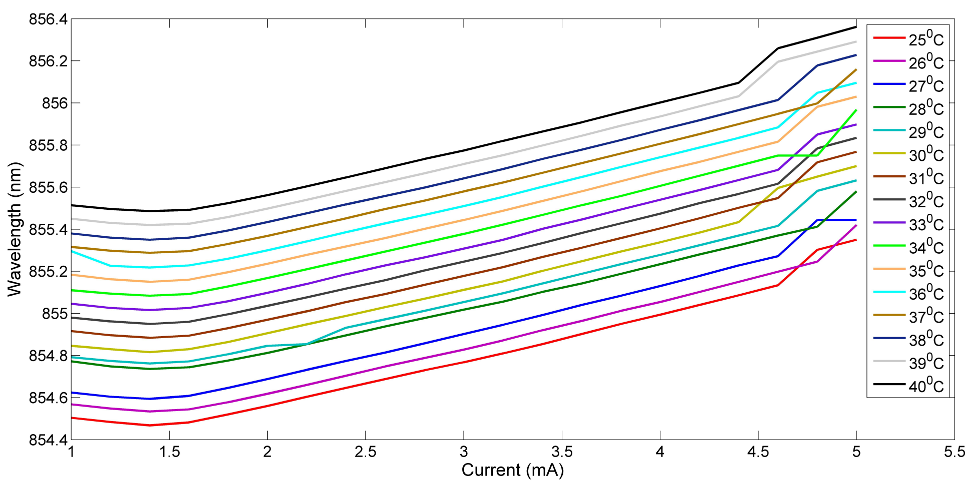

Figure 4.1: Measured Spectrum of $SS85-7U001P2$

Fig. 4.2 (a) shows the emitted power behaviour at $850nm$ for 25^0C, 30^0C, and 35^0C. The power was measured with Thorlabs PM100 USB power meter. It is noticeable that the output power of the laser, P_o decreases with increasing temperature and tends to level out after $5.0mA$. This is in well agreement with the theory as the characteristic roll-over for higher currents is observed. The maximum attainable power is below $350\mu W$, whereas the specification indicate a typical output power of $700\ \mu W$. The low output power arises from the imperfect pigtailing of VCSELs in terms of light coupling and polarization. Fig. 4.2 (b) plots the side mode suppression ratio (SMSR) values at 20^0C and 25^0C. Over the spectrum of the temperature, the variation of SMSR is within 10dB and appears to be randomly distributed. Due to the short optical cavity, the beam emission is not completely single modal and the randomness of SMSR thus arises. For some current, SMSR is found to be almost 0dB, whereas it is as high as 10dB at some

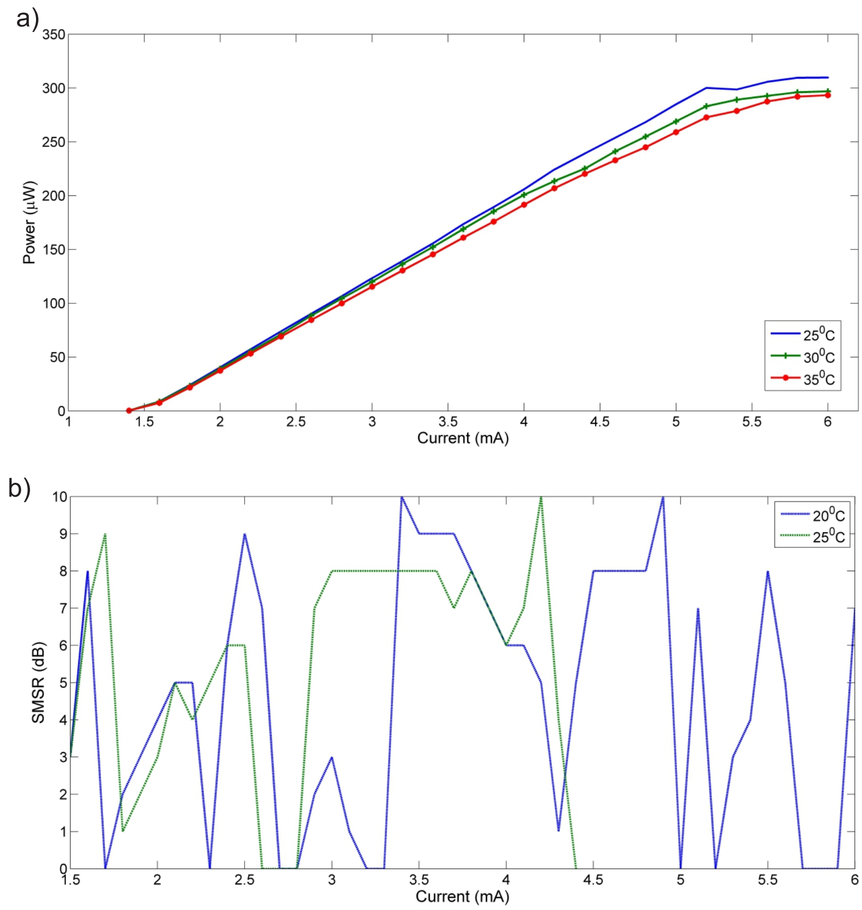

Figure 4.2: Measured power and SMSR of $SS85-7U001P2$ at different temperatures. a) Emitted power behaviour, b) SMSR

other points keeping good agreement with the datasheet specifications. At 35^0C, the scanning range ($2\,\mathrm{mA} - 4.4\,\mathrm{mA}$) of this VCSEL is found to be 532 pm which corresponds to a sampling resolution of 0.05 pm.

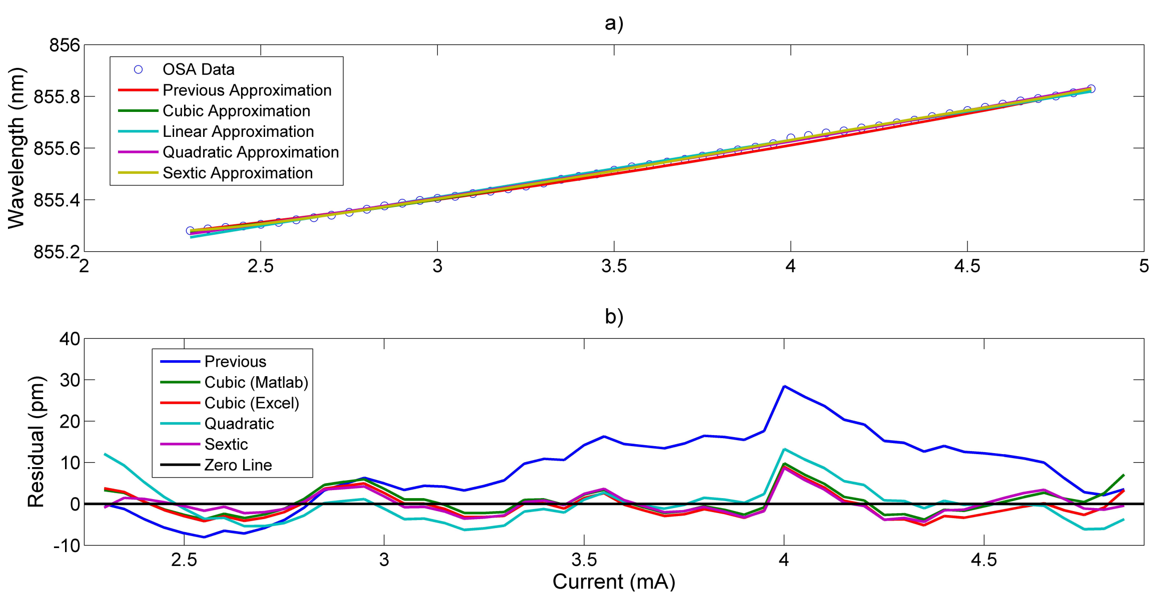

Figure 4.3: Current to wavelength linearization on the basis of polynomial equations. a) Multiple polynomial equations fitted to the OSA data, b) Residuals of the fit equations.

POLYNOMIAL ORDER	RMSE	R-SQUARED
Linear ($p = 1$)	0.00801	0.9978
Quadratic ($p = 2$)	0.004688	0.9993
Cubic ($p = 3$)	0.003087	0.9997
Sextic ($p = 6$)	0.002769	0.9998

Table 4.2: Regression analysis of the $I \iff \lambda$ linearization for $SS85-7U001P2$

Selection of optimum temperature setpoint

Following these analysis, 35^0C was selected as the VCSEL driving temperature considering two reasons. Firstly, the response of VCSEL in terms of power and wavelength appears relatively stable at this temperature as found from the characterization data. Secondly, since the system temperature will be normally higher than the temperature of the surrounding, the excess heat can always dissipate away easily i.e. the surrounding acts as a passive heat sink.

Current to wavelength linearization

Now, for better precision of the fit procedure, the second step of the characterization of the Optowell VCSEL was carried out. Here, the VCSEL was characterized for a single temperature (35^0C) at a finer step size than that of the former characterization settings. Fig. 4.3 (a) illustrates the fitting procedure on the later characterization data. On top of the data, different fit estimations are plotted. The red curve indicates the linear estimation of current to wavelength on the basis of the previously characterized data. Due to the non-linearities arising from the multimodal behaviour of the VCSEL, a linear function cannot estimate the data variation completely. It should be noted that the approximation of the linearization is an empirical equation that is derived from the observed data, not from the physics of the device itself.

Polynomial functions are the optimum option in this context and thus, polynomial functions of order 2, 3, and 6 were investigated. The residuals of these fit functions are plotted in Fig. 4.3 (b). Here, the residuals of cubic approximations determined using Matlab and MS Excel is plotted along with the residuals of the remaining functions of Fig. 4.3 (a). These two programs use different algorithms to perform the fit procedure. It can be observed that the robust trust region Lev-Mar algorithm of Matlab predicts the approximation much better than the QR decomposition method used in excel. For third order polynomial and above, the root mean-squared error (RMSE) value does not improve significantly. Table. 4.2 lists the regression analysis result of these fit parameters. Apart from RMSE, the fit equation itself cannot explain much about the uncertainty of the data for $p \geqslant 3$ which is observable in the R-square column. Therefore, considering the required computation time of the mother application, Cubic approximation was selected for the current to wavelength linearization.

This cubic approximation is then implemented in the mother application. To get a feeling on the non-linearities present in the $I \iff \lambda$ linearization equation, the output of an asymmetric MZI was recorded and analysed. Like MRR, the MZI was connected to the OSROM and the external thermotable was not used. In Fig. 4.4(a), this output data is plotted with the characteristic equation of the MZI, termed as y_{ideal}. Ideally, the output response of a MZI is sinusoidal. However, the response curve is not perfectly sinusoidal when current to wavelength linearization is not linear, i.e. the amplitude and the frequency of the MZI response is not constant over the scanning range and the phase relationship with time is nonlinear. Thus, the nonlinearities present in the current to wavelength approximation can be observed by comparing the characteristic response with the recorded response of a MZI. The MZI output differs from the ideal output noticeably in the beginning where the VCSEL current is close to $I_{threshold}$. Further-

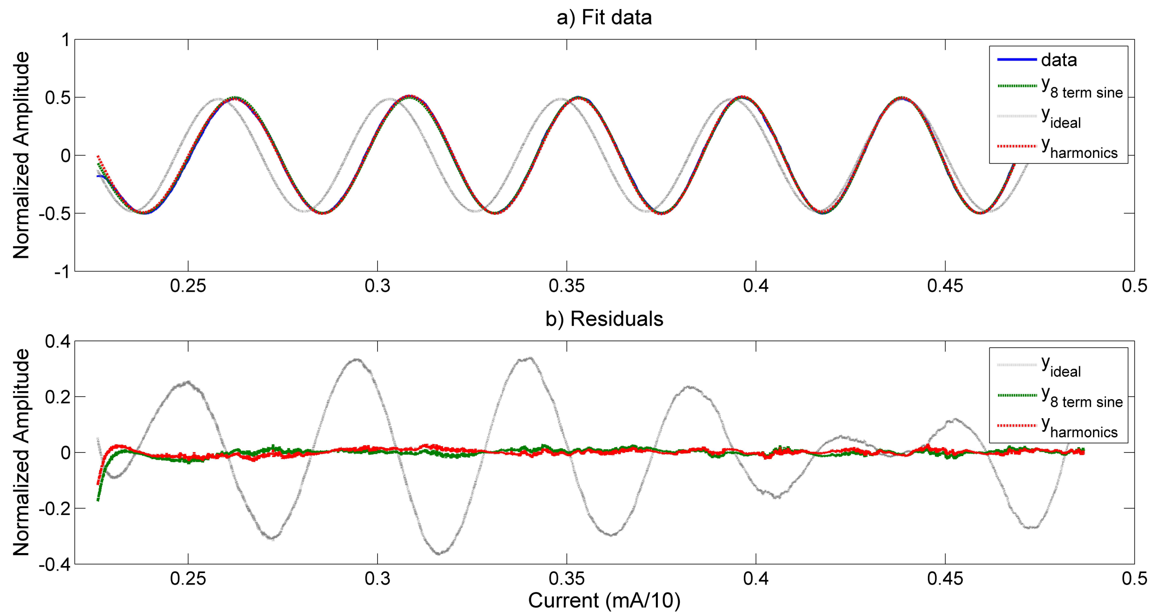

Figure 4.4: Fit approximation of asymmetric MZI output data. a) Fitted plot, b) Residuals

more, two fit equations were implemented on the output data. One is a sum of 8 term sine function. This is simply a combination of eight separate sine equations which would mean that the output signal is not a single signal rather a sum of eight separate sinusoidal signals. The problem that comes along with this equation then is that it fails to provide any insight on the non-linearities present in the $I \iff \lambda$ linearization. Nevertheless, it can explain 99.82% data. Another equation is based on the harmonics. Harmonics are the frequencies that are integer multiple of the fundamental frequency. Considering the frequency i.e. $\frac{c}{\lambda}$ has harmonic components up to fifth order, a single sine equation is derived. This equation has better RMSE of 0.0117 compared with the RMSE of 0.0151 of the former approximation. Although the R-squared value increases slightly by 0.07% for the later estimation, it gives an insight on the non linearities present, and is realized as the integer multiple of the fundamental frequency.

Verification of nonlinearities by MZI

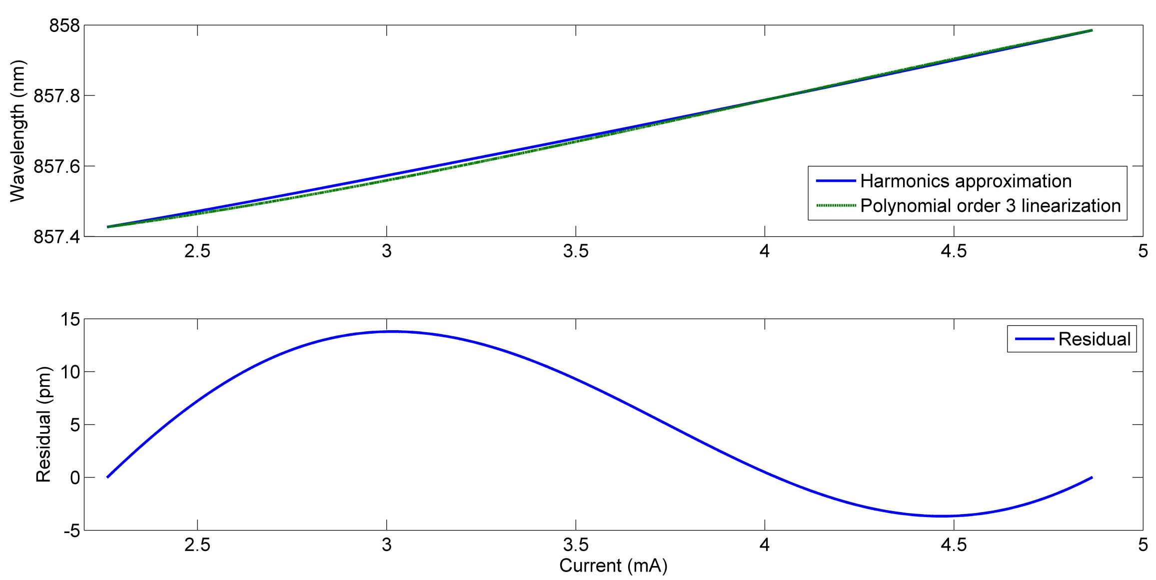

Figure 4.5: Comparison between Cubic $I \iff \lambda$ approximation and Harmonics approximation. Top - Fit equations, Bottom - Residuals

The knowledge of the presence of harmonics provides us with an equation, which is then compared with the implemented I $\iff$ λ linearization. Fig. 4.5 shows the relative comparison between these two equations. There exists a similarity in the trend of the residual values of Fig. 4.4 and 4.5. The deviation of data from the ideal equation is higher for the current values smaller than 4mA, lower for the rest and is almost zero around 4mA. Similar analogy can be deduced for the residuals of Fig. 4.5. Thus the implemented I $\iff$ λ linearization was updated as per the harmonic approximation. It should be noted that this new approximation is merely a correction on top of the cubic linearization.

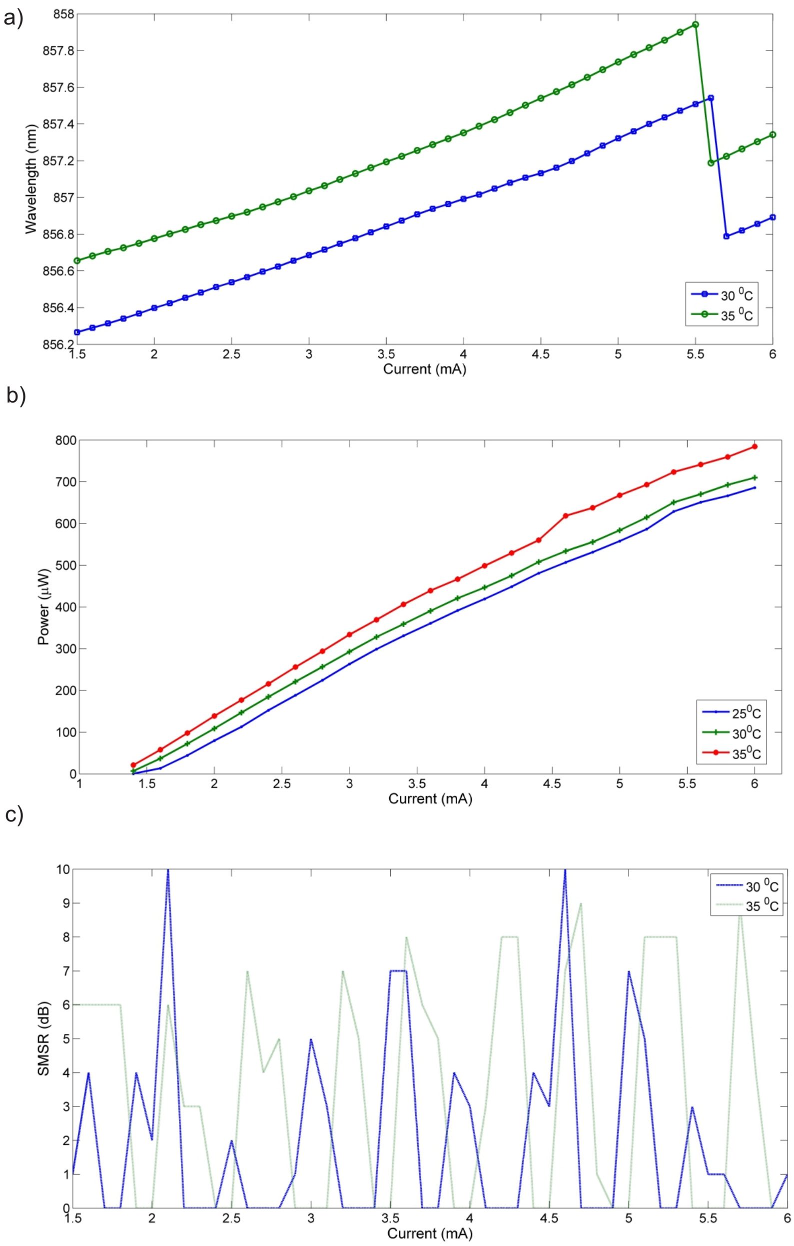

Figure 4.6: Characterization data of ULM850 — B2 — PL — S0101U. a) Measured spectrum, b)Emitted power behaviour, c) SMSR

Characterization of ULM850 — B2 — PL — S0101U

For characterizing the ULM850 — B2 — PL — S0101U, an automated data collection procedure was implemented for the ease of characterization as discussed in Appendix A.3. Fig. 4.6 illustrates the complete characterization of the ULM VCSEL. Two out of four spectrum are pre-

TEMPERATURE	POLYNOMIAL ORDER	RMSE	R-SQUARED
30^0C	Cubic $(p = 3)$	0.007136	0.9996
	Sextic $(p = 6)$	0.003007	0.9999
35^0C	Cubic $(p = 3)$	0.002894	0.9999
	Sextic $(p = 6)$	0.002519	1.0

Table 4.3: Regression analysis of the $I \iff \lambda$ linearization for $ULM850 - B2 - PL - S0101U$

sented here. For this VCSEL also, the focus temperature was 35^0C. The spectrum, for all the temperatures up to 35^0C, has a steady rise till $5.5mA$, falls sharply with a slope of $7.54nm/mA$, and continues to climb again gradually. This makes the VCSEL one of the ideal candidates for linearization. Fig. 4.6(b) shows the L-I curve. The emitted power behaviour of the ULM VCSEL

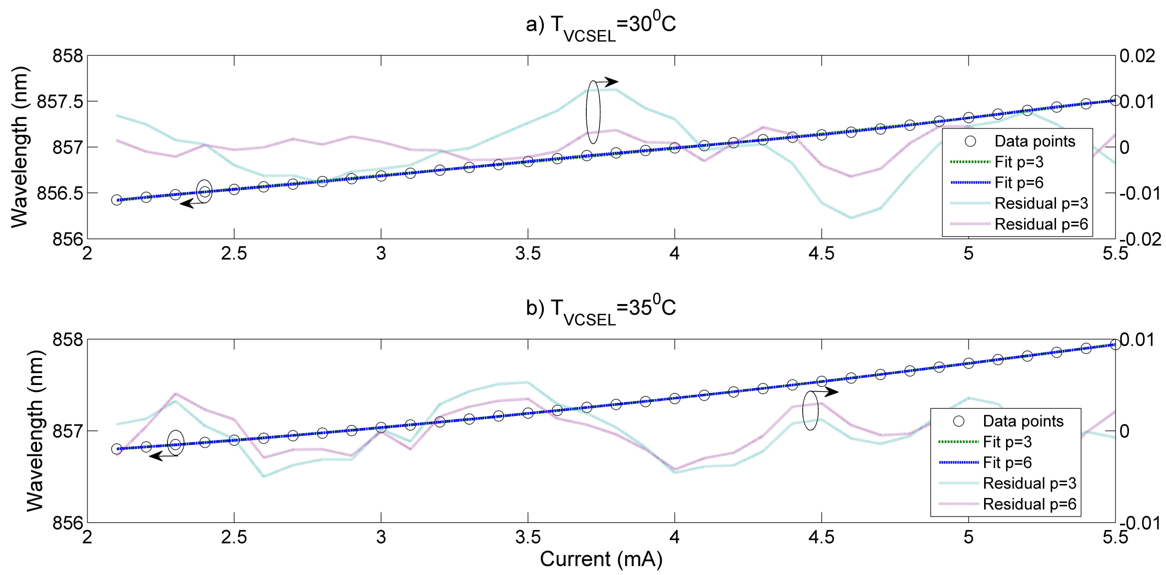

Figure 4.7: Comparison between 35^0C $I \iff \lambda$ linearization applied at different VCSEL temperature, a) $T_{VCSEL} = 30^0$C, b)$T_{VCSEL} = 35^0$C

is completely opposite to the Optowell VCSEL. Instead of decreasing power with increasing temperature, the former shows distinct power increment at different temperature. The maximum attainable power at $6mA$ is $783.91\mu W$ and does not show any tendency to level out like Optowell. Maximum SMSR at 35^0C is $8dB$ which is $2dB$ lower than the previously measured spectrum's SMSR. At 35^0C, the scanning range $(2\ \text{mA} - 5.4\ \text{mA})$ of this VCSEL is found to be 1124 pm which corresponds to a sampling resolution of 0.11 pm.

Like the Optowell VCSEL, the characterization data were analysed for $I \iff \lambda$ approximation and fitted with cubic and sextic approximation of the current to wavelength which is depicted in Fig. 4.7. This time we applied the $I \iff \lambda$ approximation of one temperature to the data of another temperature and performed regression analysis, the data of which is listed in Table. 4.3. It is promising that the sextic approximation for ULM VCSEL can explain the variation in data with absolute certainty at 35^0C and similar high certainty is observable at 30^0C also. Comparing the RMSE values, the chosen approximation for ULM VCSEL was Sextic $I \iff \lambda$ linearization.

Current to wavelength approximation for ULM laser

4.3 DRIFT AND SENSITIVITY LIMITATION

The effect of VCSEL temperature stability on the detected signal was considered as *Drift* in the context of this work. All components, capacitors, inductors and transformers, and semiconductor devices and circuits have maximum operating temperatures specified by manufacturer. Component reliability decreases with increasing temperature. There is an approximate rule of thumb that the semiconductor failure rate doubles for every $10^0C - 15^0C$ increase in temperature above 50^0C. For the purpose of the VCSEL temperature control, it is placed in a well isolated thermoelectric cooler (TEC), referred to as *oven*. It should be noted that the oven does not measure the VCSEL temperature directly. As discussed in Section. 2.5, the oven uses the temperature of its cooling plate for the control feedback loop. Thus, in the detection system, the VCSEL temperature does not imply the temperature of the VCSEL directly, rather the temperature of the TEC's cooling plate on which the VCSEL is placed.

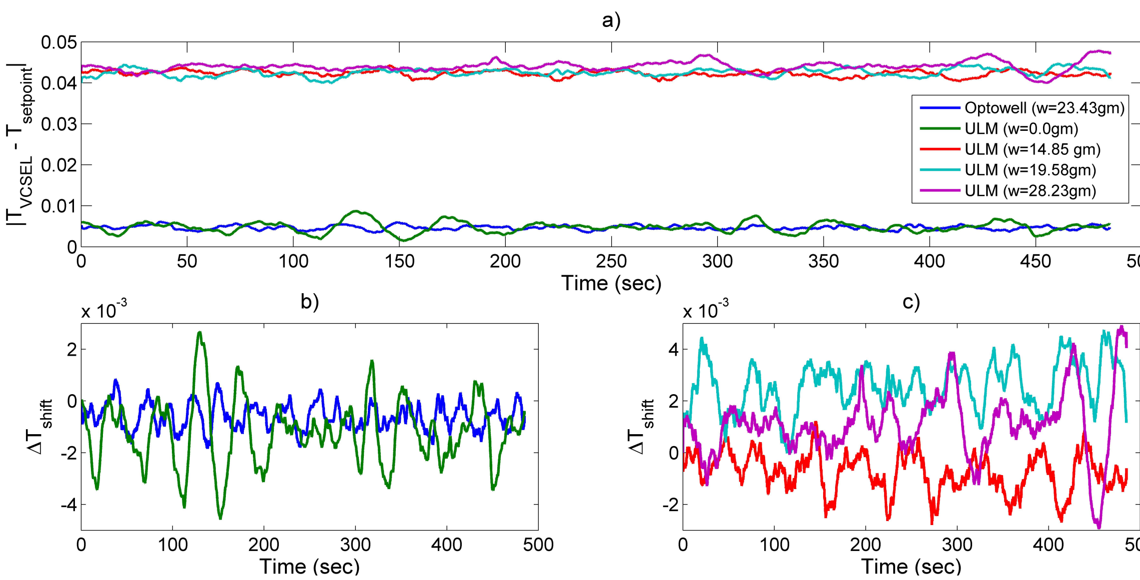

Figure 4.8: Effect of placing a heat sink on the cooling plate of TEC. a) differential temperature graph of varying weight heat sink, b) & c) Relative shift in the temperature fluctuation observed in (a)

VCSEL temperature instability from oven

After the selection of ULM VCSEL, installing it inside the OSROM gave rise to an issue with VCSEL temperature instability. The Optowell VCSEL is purchased as a bare die which required soldering of electrical terminals as well as pigtailing of optical fiber. A custom made holder was provided by the manufacturer for placing the VCSEL inside the oven. This holder is made of brass and designed as such that it effectively transfers the heat from the VCSEL to the surface of the cooling plate uniformly. On the contrary, the ULM VCSELs were already soldered and pigtailed upon receiving, and housed in a rectangular metal casing with a transparent glass top. Placing the VCSEL directly inside the oven produces noticeable temperature fluctuation as illustrated in Fig. 4.8. The standard deviation, σ_{ULM0} is 0.0013^0C which is relatively high compared with $\sigma_{optowell}$ of 0.0005^0C. The $\frac{\Delta\lambda}{\Delta T}$ is calculated to be 67.2 pm/^{0}C and 95.2 pm/^{0}C for Optowell and ULM VCSEL respectively, which corresponds to a change of 1 pm shift in the peak wavelength for 0.015^0C and 0.011^0C respectively in case of Optowell and ULM VCSEL. If oven response of Optowell is considered optimum, the uncertainty in the lasing peak wavelength is $0.33\dot{3}$ pm whereas, for ULM VCSEL, it is 1.182 pm. It will introduce similar amount of measurement error during characterization steps as well as in future sensing application. Therefore, to minimize σ_{ULM}, the initial guess solution was sandwiching a heat sink, whose weight is equal to that of the holder of Optowell, in between the VCSEL and cooling plate of the TEC.

Since the difference in weight between the Optowell and the ULM VCSEL oven was measured to be 18.28gm, the guess solution was a simple deduction of this investigation. Brass (Cu_3Zn_2) was the choice of heat sink metal in this case which has a density of 8.553 g/cm^3 and specific heat capacity of about 377 $J/(kg.K)$. In the workshop of the university, round coin shaped pieces of three different weights, specifically 14.85 gm, 19.58 gm, and 28.23 gm, were cut and polished from a cylindrical bar of brass ($\Phi = 5\ mm$) to serve the address the weight difference issue as a form of heat sink. At first, heat sink weighing 19.85 gm was installed since it is the closest value in the heat sink sample close the weight difference. $\sigma_{ULM19.85}$ was found to be 0.0009^0C indicating an improve in the situation. Since the heat dissipation is greater for bigger heat sinks as a rule of thumb, heat sink weighing 28.23 gm was placed instead with an attempt to minimize σ_{ULM}. Yet, an increased $\sigma_{ULM28.23}$ of 0.0012^0C was recorded nullifying the rule of thumb assumption. This may sound conflicting. However, the heat sinks used in the context of stabilizing the temperature in this work should be considered as a holder for the VCSEL that, apart from providing a firm base for VCSEL inside the oven, distributes the heat evenly on the surface of the TEC cooling plate. Therefore, the lightest heat sink in the sample will provide smallest heat path to the cooling plate as well as relatively faster heat distribution over the cross sectional area of the heat sink compared with the heavier heat sinks. Also, increasing the mass of brass heat sinks does not change the density of the material but, in the context of this work, increases the height. This results in longer heat path and slower heat dissipation over the entire surface. The aim of this experiment was to find a suitable holder for the VCSEL inside the oven, so that the heat dissipated by the VCSEL distributes evenly on the surface of the cooling plate.

Thus, the lightest heat sink in the sample was introduced and $\sigma_{ULM14.85}$ was calculated to be 0.0007^0C which is a significant improvement to the situation. Also noticeable in Fig. 4.8(a), there is an offset of about 0.04^0C between the graphs of ULM oven with and without heat sink. The source of this offset might be the unequal heat distribution on the cooling plate surface. Investigating the geometry of the custom made holder, it appears that the design channels the heat to the thin round foot of the holder, thus making the heat distribution equal. On the other hand, the ULM VCSEL is a rectangular box mounted on top of a coin shaped heat sink using thermal epoxy. So, the heat transfer follows both convective and radiative path with a Gaussian distribution having maximum intensity at the center of the coin. From operational point of view, the TEC can control the temperature without going into *thermal runaway* for $|T_{VCSEL} - T_{setpoint}| \leqslant 0.05^0$C. This offset is still within the operating range.

Another investigation shows that the VCSEL temperature instability does not solely depend on the TEC. Here, VCSEL temperature was observed explicitly during gas sensing. The MRR chips are designed for liquid sensing, which upon surface modification, can prove to be excellent gas sensors as well. Point to be noted in this case is that the modifications are implemented only on the surface, keeping the design layout intact. Fig. 4.9 depicts the temperature response of the VCSEL during a gas sensing measurement. The sensing window of the MRR chip is coated with a Teflon layer with a thickness of approximately 3μm. This transduction layer reacts selectively to the presence of acetone (C_3H_6O) vapour. The optical effect is due to swelling of the Teflon layer through the absorption of C_3H_6O. In this experiment, a droplet of acetone is put in an empty beaker, after which (at time $t \approx 35s$) the assembled MRR sensor chip is put

VCSEL temperature instability from chip design

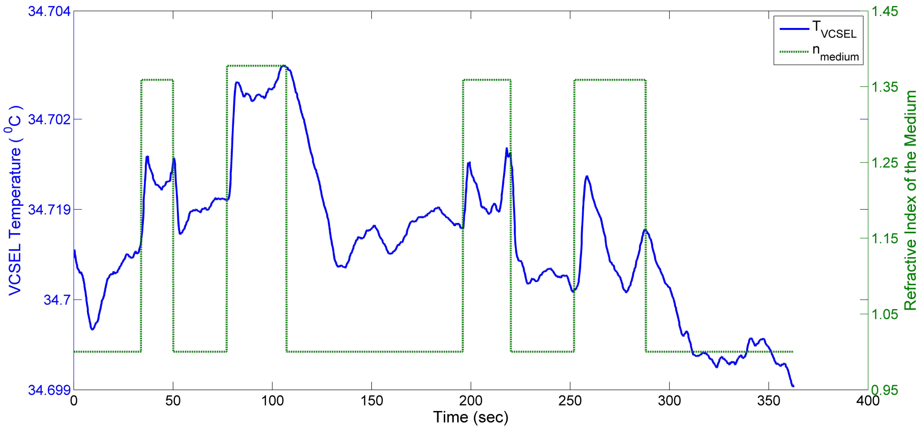

Figure 4.9: VCSEL temperature variation as a result of light being back-reflected from the chip facet to the VCSEL cavity.

nearby. The sharp rise in temperature is clearing visible occurring almost instantly. The sensor is removed at $t \approx 50$s. Following that, the acetone vapour quickly diffuses out of the sensing layer resulting in a sharp fall in temperature. Next, couple of droplets of isopropyl alcohol (C_3H_8O, IPA) is put in an another empty beaker and the chip was exposed to IPA vapour (at $t \approx 75$s). Seemingly, the Teflon membrane experiences a deformation for the diffusion of C_3H_8O and a marked increase in the VCSEL temperature is seen again. When the sensor is taken out (at $t \approx 105$s), it appears that the IPA vapour diffuses out of the sensing layer at a slower rate and a gradual decline in temperature is observed. These two steps were repeated again which is displayed by the green dotted line corresponding to the right y axis. A change in the refractive index of the medium from $n_{air} = 1.000277$ to $n_{C_3H_6O} = 1.359$ showed a temperature variation of 0.008^0C, whereas for $n_{C_3H_8O} = 1.3776$, it is 0.015^0C. Although droplets were not quantified at all, this experiment shows the limitation in peak detection imposed by the chip design layout for gas sensing with an uncertainty of 1 pm. Analogous experiment was performed for the chips designed for liquid sensing. The measurand was changed from solutions to solutions, but the effect seen for the chips for gas sensing is completely absent in case of liquid sensing. Since the design layout has straight input waveguide, the possible explanation for this behaviour is the back-reflection of light from the chip facet to the laser cavity, thus effectively increasing the temperature, due to the deformation in the Teflon membrane in presence of gases.

Sensitivity limitations

Now, let us focus on the sensitivity limitations. The optical inputs of OSROM are Thorlabs FDS02 photodiodes. With an anode and cathode connection, the detector is placed in a $TO-46$, FC/PC connector package. The anode of the photodiode generates a current as a function of the incident wavelength and optical power. Normal measurement conditions facilitate a current production in μA range. From the specifications of the photodiode used, NEP is quoted as 9.29×10^{-15} $W/\sqrt{Hz}$ at 850 nm and the responsivity is given 0.48 A/W for the wavelengths ranging from $400 - 1100$ nm. Considering ≈ 500 μA of input power at 4 mA, the SNR is calculated theoretically to be 214.619 dB. The input amplifiers of the OSROM convert this current to a voltage in the order of magnitude of several volts which is sent to the DAQ subsequently.

The gain level of these amplifiers is adjustable in six levels with a selector switch. These input gain determine the bandwidth of the photodiodes as well as the slew rate of the amplified signal. If the maximum slew rate is exceeded, the input amplifier can no longer keep up with the change in input signal. This gives rise to measurement errors and a limited rise or fall in the amplified signal is observed. Reducing the input gain, the VCSEL modulation frequency,

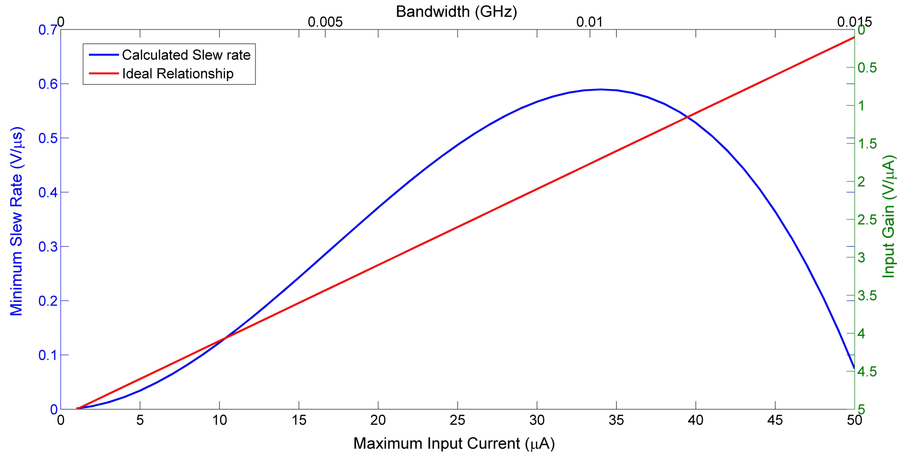

Figure 4.10: Slew rate of the input amplifier as a function of input gain, bandwidth and maximum current input

or the VCSEL current will result in a lower positive slope, i.e. the input signal will rise slowly, and measurement errors can be avoided. Assuming the maximum input current value for each input gain setting, resulting in a 5V output voltage, the provided and calculated minimum slew rates are given in Fig. 4.10. However, there is no automatic detection when the maximum slew rate is exceeded.

4.4 ELECTRONIC BOTTLENECK

The data acquisition card used in OSROM is NI USB 6353, which has channels for analog input (AI) and analog output (AO) along with digital input/output (DIO) and counters. OSROM makes use of the analog channels only. AIs are the channels read by the DAQ while AOs are the control channels. The available number of channels for AI and AO is 32 and 4 respectively. The main blocks featured in the AI circuitry is depicted in Fig. 4.11.

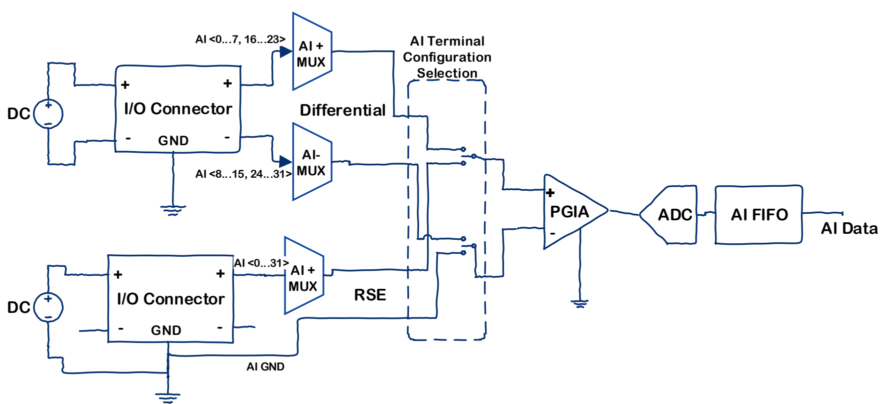

Figure 4.11: NI USB 6353 Analog Input circuitry

Terminal configuration for input connections

There are two types of terminal configurations used for the input connection of this system. For ground-referenced signal sources, *differential* configuration is chosen whereas for floating signal sources, *referenced single-ended*, RSE configuration is used. By definition, a floating signal source has no connection with the default ground system, rather its ground-reference point is isolated. Thereby, all the AIs except those corresponding to the temperature are read as differential input connection. Since thermo-couplers has an isolated output, temperature AIs are considered as RSE connection. Continuous buffered hardware-timed method is used for the data acquisition. The DAQ is equipped with only one analog-to-digital converter (ADC). Therefore, at a time, the multiplexers (MUX) direct one AI channel to the ADC. This routing is done via the programmable-gain instrumentation amplifier (PGIA), which minimizes settling times for all input ranges ensuring the usage of the maximum resolution of the ADC. Through the conversion of the analog voltage into a digital number, the ADC performs the AI signal digitization. Finally, data integrity is safeguarded by a sizeable first-in-first-out (FIFO) buffer. Normally, differential signal connections reduce noise acquisition and increase common-mode noise rejection. On the other hand, the signal connections in the RSE modes experience greater amount of electrostatic and magnetic noise than in differential configurations as a result of differences in the signal path. The common-mode noise in the signal and the ground potential discrepancy between the device ground and the signal source is rejected by the PGIA with this type of connection. Comparing with the AI circuitry, the circuitry for the AO is much simpler. Fig. 4.12 illustrates this circuitry in the context of OSROM. Out of four available AO channels, OSROM makes use of the three channels for controlling VCSEL current, VCSEL temperature and thermotable temperature. Here, Generation of the analog output is facilitated by FIFO, the memory buffer between the computer and the DAQ. The data is subsequently sent to the respective channels after digital to analog conversion.

Terminal configuration for output connections

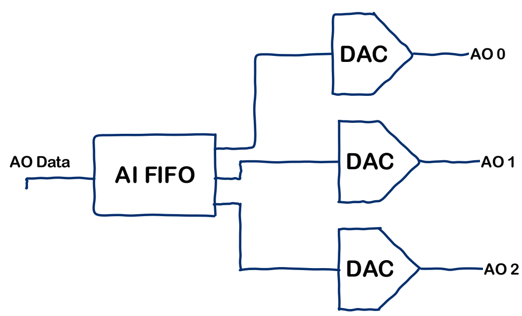

Figure 4.12: NI USB 6353 Analog Output circuitry

In the complete input-output circuitry, bottleneck occurs for the differential amplifier, PGIA and the analog-digital converters. In applications where scanning of multiple channels is required, settling time has an huge impact on the accuracy. Inside the multiplexer, the switching from one AI channel to another initiates new configuration setting for PGIA on the basis of the input range of the new channel. The input signal is then amplified by the differential amplifier with the gain for the new input range. The requisite time in PGIA operation for the input signal amplification to a desired level of accuracy antecedent to ADC sampling is attributed as settling time.

Settling time

There are several factors which can increase the settling time resulting in a decreased measurement accuracy. One of these factors is the switching of a relatively large input range to a smaller one. For an AI channel, the ADC code resolution is influenced by the input range. However, there is a trade-off present between the resolution and variation follow-up for the signal input range. A large input range reduces resolution by following large signal variation, whereas a smaller input range enhances the resolution - turning out badly in following a broad signal variation. The preferred value for the input range was selected $\pm 0.5V$. Considering an ADC of 16 bit, the ostensible voltage resolution with a guess of 5% over range is $16\mu V$ at this range. In the context of this work, the input range can be as high $\pm 5V$. When switching a

PARAMETERS	ANALOG INPUT (AI)		ANALOG OUTPUT (AO)	
No. of channels	32		4	
ADC Resolution	16 bit			
Sampling rate	Single	1.25 MS/s	3 channels	1.54 MS/s
	Aggregate	1.00 MS/s	4 channels	1.25 MS/s
Settling time (±15 ppm of step)	±10V, ±5V, ±2V, ±1V	1.5μs	±10V, ±5V	2μs
	±0.5V	2μs		
	±0.2V, ±0.1V	8μs		
FIFO size	4095 samples		8191 samples	

Table 4.4: NI USB 6353 device parameters

channel from ±5V range to a channel of ±0.5V, the significance is that the unity LSB (0.0015%) settlement of the ±0.5V full-scale range will force the input circuitry to find a resoluteness within 0.1 LSB (0.00015%) of the ±5V range. Considering the settling time for the DAQ from Table.4.4, this requirement will take 150ns for the circuitry. Therefore, the range variation must be kept as minimum as possible.

Sample rate

The datasheet provides two types of sample rates for the DAQ card. NI 6353 devices have a single channel maximum rate of 1.25MS/s and aggregate maximum sample rate of 1MS/s so they can sample one channel at 1.25MS/s or two channels at 500kS/s per channel. This is also the reason for the shift observed in Fig. 3.7. Moreover, the presence of analog-digital converter can give rise to quantization error. Since, one least significant bit (LSB) is generally much smaller comparing to the signal, quantization error becomes uncorrelated with uniform distribution. Each 1-bit change in the quantizer bit number induces a twofold shift in the standard deviation. The potential signal-to-quantization-noise power ratio therefore changes by 4, or $10.\log_{10}(4) = 6.02\ \text{dB}/bit$. Since the quantization error is not independent of the input signal at lower amplitude, dithering appears to be an possible upgrade in noise improvement. Being a hardware function, it is required that the circuitry is present within the DAQ architecture. But NI 6353 does not have external dither circuitry rather claims to generate a noise level from the ADC and PGIA combined, that is equivalent to always having a dither circuit enabled. The number of bits of the ADC, from the datasheet, is $N = 16$. Using Eqn. 2.98, the SNR of the ADC is found to be 98.08 dB..

4.5 EXTERNAL INFLUENCE MINIMIZATION

For studying the effects of the surroundings on the detection system, two parameters were considered namely, ambient temperature and evaporation of liquid measurand at a certain temperature. Since the chip stays out of the OSROM, these two factors affects the detection system most. First the effect of the presence of thermotable on the resonant peak shift of the MRR chips was investigated for four different cases as seen from Fig. 4.13. The upper part of the figure depicts the shift in absence of thermotable. Here, the chip is exposed to the surroundings at room temperature of 23^{0}C. For Fig. 4.13(a), T_{VCSEL} is set to 35^{0}C, whereas the setpoint is 23^{0}C for Fig. 4.13(b). The lower part of the figure plots the shift in presence of the thermotable. The temperature for the thermotable was set to the room temperature of 23^{0}C and VCSEL temperature was varied from 23^{0}C to 35^{0}C. Clearly, keeping the chip in an isolated system improves the shift. Varying the VCSEL temperature, on the other hand, has an interesting trend. It is seen that the VCSEL response is best at 35^{0}C. Obviously, driving the VCSEL at other temperatures will have relatively larger shift, but the effect appears to be minimal when the

Effect of ambient temperature

chip is isolated from the surrounding and produces a shift lower by a factor of 10 compared with being an open system. For all the cases except Fig. 4.8(d), the shift is downward indicating an anti-clockwise movement of the peak. Hence, it is advisory to have a closed system for peak detection whenever possible.

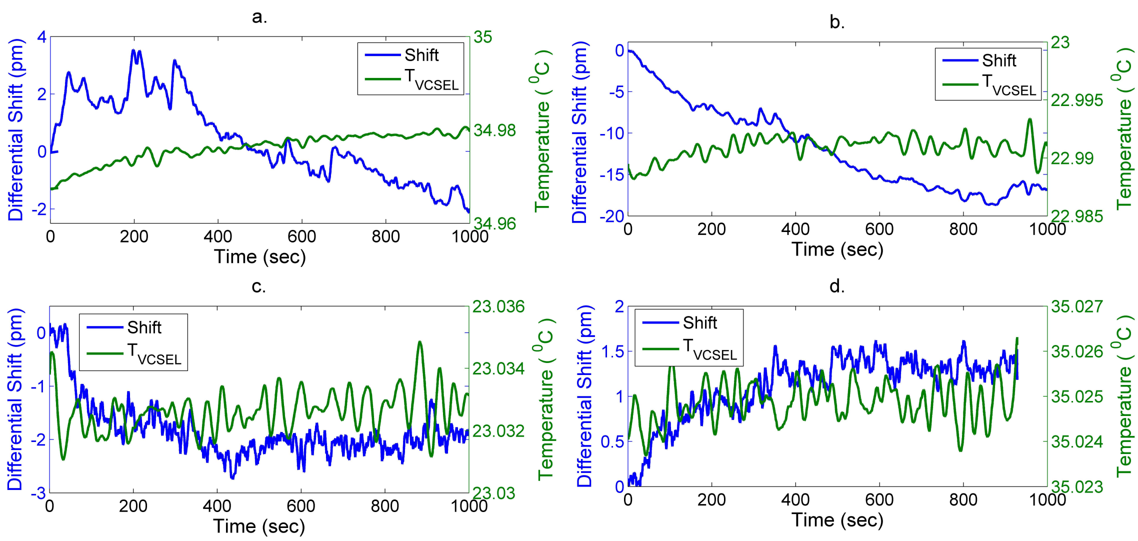

Figure 4.13: Effect of the presence of thermotable on shift. a) & b) plots the shift for the absence of thermotable at $T_{VCSEL} = 35^0$C and $T_{VCSEL} = 23^0$C respectively, whereas c) & d) outlines the presence of thermotable at $T_{VCSEL} = 23^0$C and $T_{VCSEL} = 35^0$C.

Effect of evaporation of liquid measurand

Next, the effect of evaporation of liquid measurand inside a closed system was investigated. The chip temperature, i.e. the temperature of the thermotable, in this case, was 40^0C and T_{VCSEL} was 35^0C. The used chip was exclusively for liquid sensing and the sensing medium was demineralized (DEMI) water. Fig. 4.14 exhibits the results of the investigation. Each of the cuvette of the sensing well can accommodate maximum 10 μL of liquid. In case when no glass-top is used, the water from cuvette 1 (represented by blue line in the figure) evaporates at $t \approx 610$ s, whereas the water from cuvette 2 (represented by green line in the figure) evaporates at $t \approx 634$ s. The small difference of ≈ 24 s for evaporating the same amount of water arises from the geometry of the chip holder inside the thermotable. Nevertheless, the complete amount of water evaporates at an average of $t \approx 622$ s. In case when a thin glass plate was used approximately 200μm above the chip surface to minimize evaporation, the water in cuvette 1 was found to be evaporated completely to the naked eye at the end of the timespan ($t \approx 1222$ s) showed in Fig. 4.14(b). The amount of evaporated water is 1.61×10^{-8} kg/s in case of Fig. 4.14(a) and 8.18×10^{-9} kg/s in case of Fig. 4.14(b). The amount of water evaporated per second can also be calculated from the following empirical equation,[56]

$$g_s = \frac{\theta A \left(x_s - x\right)}{3600} \tag{4.1}$$

where, g_s is the amount of evaporated water in kg/s, θ is the evaporation coefficient in kg/m^{2}s and expressed as $(25 + 19v)$, v is the velocity of air above the water surface in m/s (the units do not match since the equation is empirical in nature[56]), A is the water surface area in m^2, x_s is the humidity ratio in saturated air at the same temperature as the water surface in kg/kg and x is the humidity ratio in the air in kg/kg. Using the psychometric chart, $x_s(max)$ is found to be 0.0498 kg/kg, while x is 0.0185 kg/kg at 40^0C for 39% relative humidity. Each of the two sensing windows of the MRR chip has an area equal to 1.6678×10^{-5} m^2 which was considered as A in the context of the equation. Solving Eqn. 4.1 for the values of g_s found from the experiment with no glass-top and with glass-top, the velocity of air above the water surface is calculated to be $0.00127\,m/s$ and $0.00046\,m/s$ respectively. The glass-top reduces the air velocity by a factor of 2.76, the effect of which can be clearly seen from the zoomed inset in Fig. 4.14. The shift response is zoomed up to $t \approx 500\,sec$. If the chip surface is open, which is normally the case due to the absence of microfluidic system, the shift is twice the time larger than the case when the surface was partially covered by a glass top. So, minimizing evaporation effect significantly increases the detection accuracy. Implicitly, this also emphasizes on the necessity of a microfluidic system for liquid sensing.

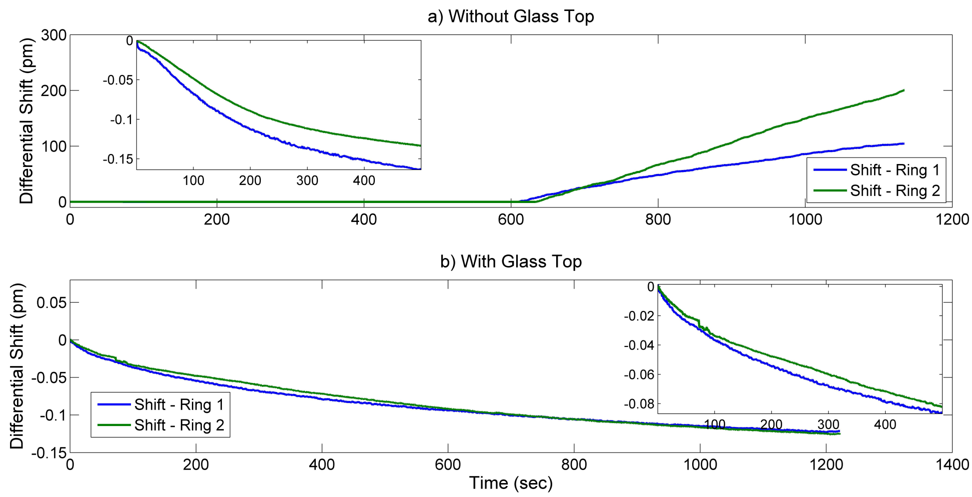

Figure 4.14: Effect of evaporation on shift. Zoomed response up to 500 sec is shown in the inset. a) Chip not covered and b) chip is partially covered.

4.6 SUMMARY

In this chapter, the detailed analysis of the hardware used in the detection system is presented. At first, the VCSEL that was already in use was characterized and an improved $I \iff \lambda$ linearization was implemented. The non-linearities within this approximation was further investigated using an asymmetric MZI and the derived modifications was applied. The fit region of Optowell VCSEL was found to be very close to the free spectral range of the MRR chip, and subsequently, a new VCSEL was characterized. It was found to be a better replacement for the existing one. Next, the instability observed in VCSEL temperature was investigated. Proper choice of heat sink addressed the issue. It was found that uniform heat distribution is required for the TEC to effectively control the temperature where increasing the weight does not appear fruitful. A deeper examination revealed a design flaw in the chip that becomes dominant for gas sensing. Following the drift limitation, a brief discussion on photodiodes and input amplifiers was presented. After that, some of the bottleneck calculations for the DAQ was performed and the limitations that comes along were discussed. Finally, the effect of ambient temperature in terms of isolating system and the corresponding evaporation that follows was studied. It was found that keeping the chip in an isolated system, even at room temperature, will result in reduced shift from thermal drift. Alongside, the necessity of the microfluidic system was pointed out.

5

SYSTEM EVALUATION

5.1 INTRODUCTION

The previous chapters presented the design and calibration aspects related to the detection system architecture. On the basis of these analysis, the peak detection algorithm was developed in MATLAB, the code for which is given in Appendix A.3, and implemented in LabVIEW afterwards. The MATLAB code, along with the fit procedure, measures several performance metrics and evaluate the performance of the system under various circumstances. This provided a means to interpret the performance metrics of the detection algorithm. Section 5.2 presents a detailed discussion on this topic.

The complete detection system will be evaluated in terms of real-time sensing afterwards. First, in Section 5.3, the efficiency of the system for selective biochemical surface reactions before the complete development is evaluated. This scenario will not feature label free biochemical sensing, because the sensitivity resolution of the MRR chips, in this aspect, were already reported[17]. Next, the efficiency of the system for gas detection in ambient atmosphere is assessed. This experiment will consider explicitly for carbon dioxide to test the applicability of the MRR sensor as an environmental gas sensor. Previously in the work of Heideman et al.[17], the possibility of realizing an environmental gas sensor was illustrated, but was not quantified. For the context of this work, a well-quantified experiment was performed, the results of which are discussed in this section. Finally, this chapter closes with some remarks on the executed analysis in Section 5.4.

5.2 PERFORMANCE METRICS OF THE DETECTION ALGORITHM

For ensuring high accuracy and real-time precision, the DAQ is set to the fastest available scan rate of 10Hz. This scan rate corresponds to 10000 datapoints for each channel in $0.1sec$. It provides huge amount of datapoints, which certainly gives an advantage of using larger fit region, while imposes a limit in the processing time. Since larger fit region means, apart from being highly accurate, higher processing time, the performance of the peak detection algorithm is tested in three steps for 35 sample datasets. At first, a single sample data is fitted and checked for convergence with Lorentzian approximation. Upon success, the effect of the number of datapoints, (N) on the integrity of the fitting procedure is analysed. Thirdly, noisy experimental measurements, y_{data} are smoothed by using a median filter of rank r, which determines the suppression of impulse errors with various widths corresponding to N. Analysis of varying r with the fitting procedure completes the list of algorithmic parameters considered in the context of this work.

Convergence with Lorentzian approximation

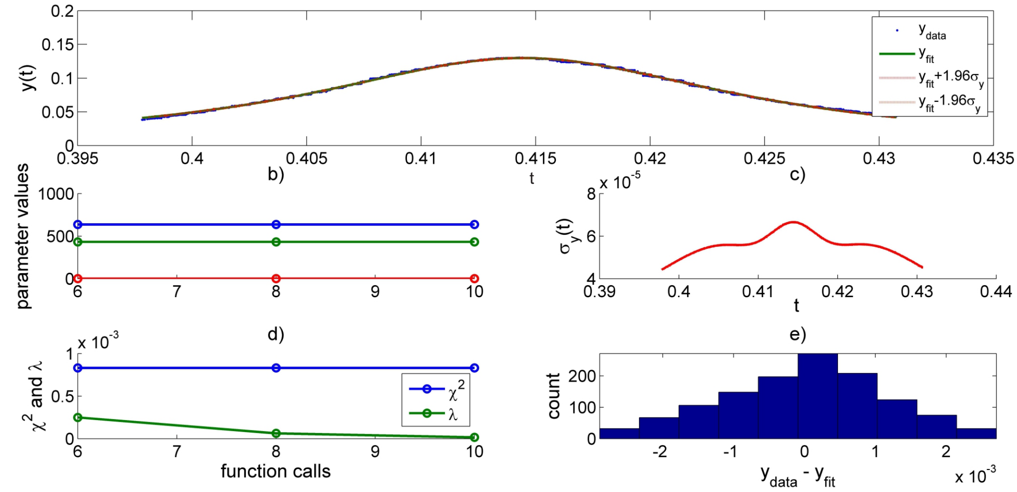

Figure 5.1: Fit analysis for a single iteration with $r = 10$, $N = 200$. a) data y, fitted curve $\hat{y}(t; p_{fit})$, fitted curve with associated error, and without error; b)the convergence of the parameters p_1 (blue), p_2 (green) and p_3 (red) with each iteration; c)standard error of the fit, $\sigma_{\hat{y}}(t)$; d)values of χ^2 and λ each iteration; e)Histogram of the errors between the data and the fit.

p_{init}	p_{true}	p_{fit}	σ_p	$\frac{\sigma_p}{p_{fit}}$
$1.0e+03$ *				
0.6310	7.2080	0.6367	0.0002	0.0000
0.4300	0.4300	0.4322	0.0004	0.0001
0.0001	0.0001	0.0001	0.0000	0.0001

Table 5.1: Function parameter values and standard error

For fitting a single dataset, a set of "true" parameter values $\hat{y}(t; p_{true})$ were predefined. Since the truest parametric values of the sample dataset is unknown due to the uncertainties in the measurement, the parametric values of the complete dataset were selected as $\hat{y}(t; p_{true})$. The fit procedure does not consider the complete dataset, rather the number of datapoints within the dataset that corresponds to the FWHM as discussed in Section 3.2. Then, the parameter convergence from an inaccurate introductory assumption p_{init} to values closer to p_{true} is investigated. In this regard, p_{true} refers to the parameters estimated on the complete dataset and p_{init} corresponds to the selected subset of the sample. For an objective function of Lorentzian distribution, there are three parameter, $(n = 3)$, namely, amplitude of the peak, half width half maximum and location of the peak. In this order, the parameters are used in the program and termed p_1, p_2 and p_3 respectively. Fig. 5.1 illustrates the evolution of the parameter values, χ^2, and λ from iteration to iteration for a rank 10 median filtered $N = 200$ additional data points . The "true" parameters p_{true} along with the initial parameters p_{init}, derived curve-fit parameters p_{fit} and standard errors of the fit parameters σ_p are demonstrated in Table. 5.1.

The R^2 fit criterion is 99.8 percent. Here, the standard parameter errors are all less than 0.005%. The parameter correlation matrix is given in Table. 5.2. All the parameters are correlated with each other. Parameters p_2 and p_3 are most correlated at -72 percent. Parameters p_1 and p_2 are the least correlated at -0.62 percent. Fig. 5.1(a) illustrates the simulation results of the raw data collected from the DAQ, the fitted curve, and its associated 95$-$percent confidence interval. Within the confidence interval $p_{fit} - 1.96\sigma_p \leqslant p_{true} \leqslant p_{fit} + 1.96\sigma_p$, the true parameter values can be found with a confidence level of 95 percent.

	p_1	p_2	p_3
p_1	1.0000	0.0137	−0.0062
p_2	0.0137	1.0000	−0.7211
p_3	−0.0062	−0.7211	1.0000

Table 5.2: Function parameter correlation matrix

Fig. 5.1(c) plots the standard error of the fit, which is, interestingly, higher near the center of the fit domain and is smaller at the edges of the domain. This means that the Lorentzian distribution is still an approximation to the drop port response of the MRR. Yet, it is better approximation than the generalised Gaussian distribution as seen from Fig. 5.2. The Gaussian distribution cannot approximate the fit region in three distinctive portions which is represented by the three peaks in the plot of the standard error of the fit. On the contrary, the Lorentzian distribution can follow the drop response much better but still the uncertainty in the peak is dominant. However, the nonlinear least squared curve-fit algorithm with Lorentzian fit function shows a reduction in the standard error of the fit by a factor of 4 at the peak position.

Comparison between Gaussian and Lorentzian approximation

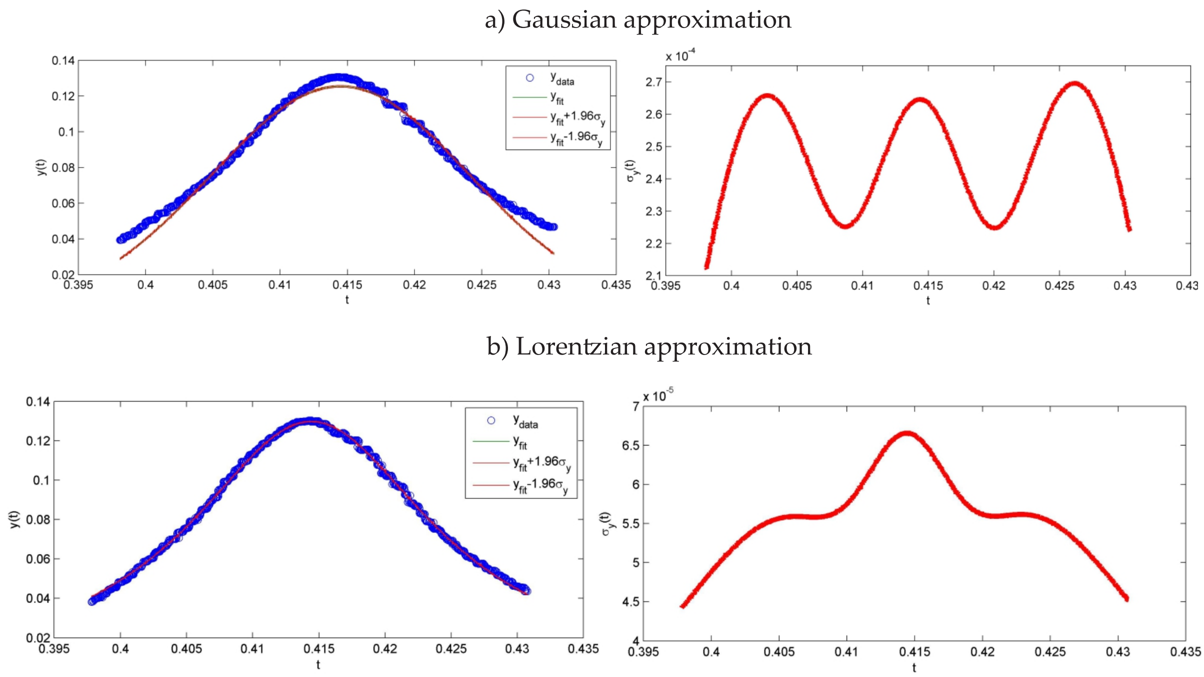

Figure 5.2: Comparative fit analysis of a) Gaussian and b) Lorentzian approximation. Left subplot illustrates data y, fitted curve $\hat{y}(t; p_{fit})$, fitted curve with associated error as well as without error, and the right subplot shows the standard error of the fit, $\sigma_{\hat{y}}(t)$

The parameter convergence and the progression of χ^2 and λ are illustrated in Fig. 5.1(b) and (d) respectively. The parameters converge monotonically to their final values. This suggests that the initial guesstimates of the parameters are very close to the true value. The histogram of the difference between the data values and the curve-fit is shown in Fig. 5.1(e). Ideally these curve-fit errors should be normally distributed, and they appear to be so.

Next, the effect of sample size on the fitting procedure is examined. For several values of p_2 and p_3, the χ^2 error criterion is calculated and plotted as a surface over the $p_2 - p_3$ plane. The objective function is based on a unimodal probability distribution but depending on the number of data points, the quadrature in the parameters may not be apparent and multiple minima

Effect of sample size on the fitting procedure

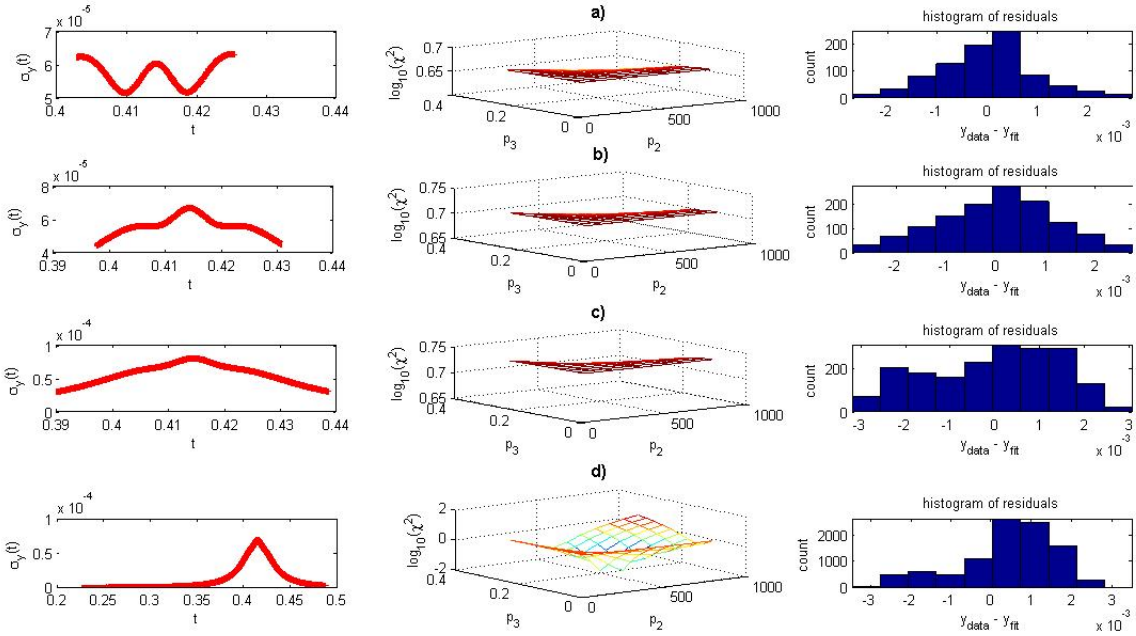

Figure 5.3: Effect of number of datapoints in fit analysis. Leftmost column shows the standard error of the fit, $\sigma_{\hat{y}}(t)$, middle column represents the sum of the squared errors as a function of p_2 and p_3 and the rightmost column charts the histogram of the errors between the data and the fit for a)$N = 0$, b)$N = 200$, c) $N = 500$ and d) all datapoints.

in the objective function may be evident. For minimizing $\chi^2(p)$, the gradient decent method endeavours to move parameter values in a direction sloping downwards. Small step sizes are often a requirement in this regard only when the objective function appears not to be quadratic. On the contrary, quadrature approximation for the Gauss-Newton method is bowl shaped, incorporating in a small number of steps towards the minimum. As a result, when the parameters are adjacent to their optimal values, this method appears to work well. In Fig. 5.3, the standard error in the fit parameters, the shape of χ^2 objective function and histogram of residuals are graphed together for four different sample set size corresponding to the addend number of datapoints on top of FWHM. The bowl-shaped nature of the χ^2 objective function is absent for $N \leqslant 500$ and but conforms to the unimodality of the objective function for complete dataset. It is logical since the smaller sample set does not necessarily corresponds to be quadratic in nature and thus we observe the down hill of gradient descent method. As a consequence, the required computation time for $N = 200$ is found to be $0.12\ sec/dataset$, significantly lower comparing with $0.25\ sec/dataset$ for the complete sample range and $0.15\ sec/dataset$ for $N = 500$. Also, the residuals are normally distributed for $N = 200$ which is not the case for the rest of the examples. Moreover, the smoothness of the objective function is not affected by the presence of measurement noise for $N \geqslant 500$ whereas for lesser number of data points, the asymptotic standard error of the curve fit experiences a significant decrease by a factor of 1.64. Considering the required computation time and the response, the optimum fit region is selected as $FWHM + 200$.

Regression analysis

The last performance metrics for the detection algorithm in the context of this work is the error analysis. Fig. 5.4 presents the regression analysis for the Lorentzian approximation on 35 sample datasets of 10000 datapoints each. The upper portion of the figure charts the regression analysis for different median filter ranks at $N = 200$, whereas the lower part represents the increment of fit region at $r = 10$. From Fig. 5.4(a) and (b), the choice for $r = 10$ is justified. Beyond $r = 6$, the change in R^2 error criteria does not vary noticeably. From this point of view, $r = 6$ appears to be a decent choice. But the overestimation in fitting algorithm is observed from

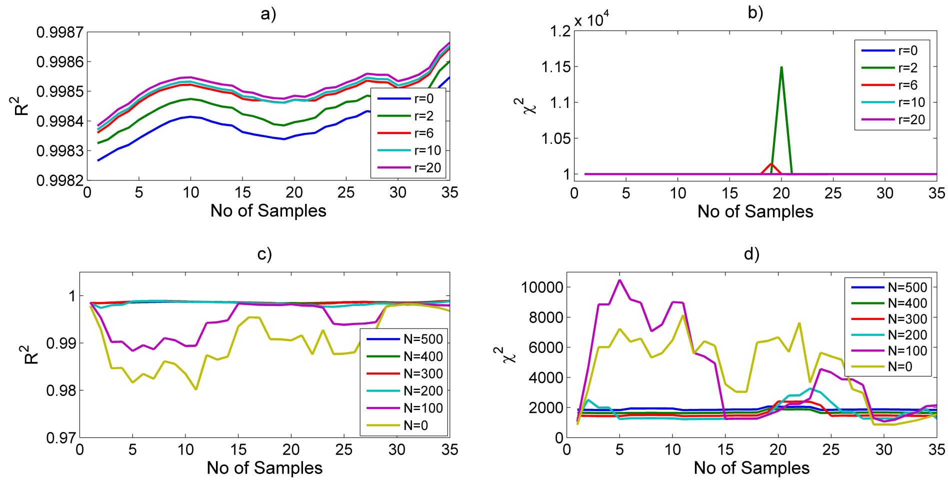

Figure 5.4: Error analysis for Lorentzian approximation on 35 samples. R-squared and chi-squared fit criterion is shown for different rank of median filter (a) & b)) at $N = 200$, and for different number of datapoints (c) & d)) at $r = 10$

Parameters	Value
λ	0.001
λ increment step	10
λ decrement step	4
Maximum number of iteration	200
Tolerance for parameters, ϵ_2	1×10^{-6}
Tolerance for χ^2, ϵ_3	0.001
Median filter rank	FWHM + 200
Data fit range	0.001
Time required (sec/dataset)	≈ 0.117
χ^2	1.7110×10^3
R^2	0.9983

Table 5.3: Algorithmic parameters for Lorentzian distribution

the χ^2 error criteria at this value. For avoiding data loss in the signal due to over smoothing, $r = 20$ was ignored leaving us with a rank 10 medial filtering option as the optimum one. On the other hand, Fig. 5.4(c) and (d) justifies the choice for $N = 200$. For values less than 200, R^2 and χ^2 values substantially fluctuate. Performing a detection in real-time precision requires that the result of the peak must be obtained within one scan range, else, a lag will be visible between the actual and processed response. This makes 200 additional datapoints an optimum choice for the current fit range.

Finally, all the corrections and modifications required for the Lorentzian estimation of the resonance peak were added up and the list of the algorithmic parameters was prepared as depicted in Table. 5.3.

5.3 EFFICACY IN REAL-TIME SENSING

Recent developments in the field of multiple protein biomarkers paved the way for genomic or proteomic diagnostic studies. One particular category of biosensors is the antibody-based biosensor or immunosensor that can detect these biomarkers rapidly. This type of biosensor relies on the ability of an immobilized antibody (Ab) to recognize its associated target, known as antigen (Ag). Immobilized or purified antibodies (Ab), also termed immunoglobulins, are of major importance both for immunochemical techniques in basic research and for diagnostic

Antibody & antigen

applications.The biological function of antibodies is to bind to pathogens and their products, and to facilitate their removal from the body. These molecules have a shape of Y implying three equal portions. A flexible tether adjoins these portions in a sloppy manner. They have two different kinds of polypeptide chain, termed as the heavy chain (H), and the light or L chain due to their molecular weight. These chains provide an antibody molecule two identical antigen-binding sites. Either one of the two variations of light chain, termed lambda (λ) and kappa (κ), is found in antibodies, but do not cause any functional differences. Since no antibodies are completely identical, only the variability of the amino acid sequences of antibodies make them unique. The amino-terminal variable or V domains of the heavy and light chains, labelled as VH and VL respectively, together make up the V region of the antibody, and confer on it the ability to bind specific antigen[57]. The association of the heavy and light chains is such that the VH and VL domains are paired. This variability shapes the antigen binding sites, thus making antibodies exclusively selective for binding ligands whose surfaces are complementary to that of the antibody. However, the species of the *Camelidae* produce a surprising exception to this paradigm. Their serum contains a considerable fraction of heavy chain antibodies that lack the light chain. Hence, the Ag-binding fragment of a classical antibody is reduced to a single variable domain, referred to as *VHH* or *Nanobody*, which can function in antigen binding in the absence of a VL. It has been reported[58] that the VHH, cloned and expressed in bacteria, is a strictly monomeric, single-domain antigen binding entity. The efficacy of the MRR system for liquid sensing will be discussed in the context of specific detection of flagella monomer by VHH antibodies.

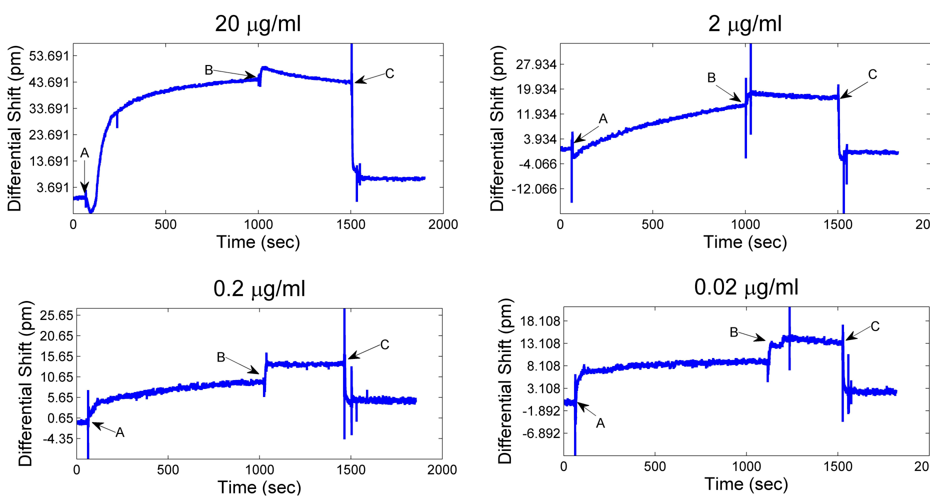

Figure 5.5: Specific detection of flagella monomer with VHH CV90

Fig. 5.5 illustrates parts of the results that were performed in one of the NanoNext Food Diagnostics measurements. These measurements were performed with the optimised Gaussian algorithm developed during the author's internship project. At this instance, the Lorentzian detection scheme was still in the development phase. VHH measurement results are discussed first, so that a comparative view can be provided for the current system performance in real-time detection.

Flagella monomer detection

In this experiment, two different VHH antibody fragments were immobilized on the MRR chips. VHH CV90, specific for *Campylobacter flagella*, was immobilized on the sensing window, whereas VHH M180, specific for Foot and mouth disease virus (FMDV), was immobilized as negative control on the remaining cuvette. The later works as reference signal for the measurement purpose. For the purpose of immobilization, 100 μg/mL VHH was used in 150mM phosphate buffered saline (pH 7.4). HBS-EP buffer (pH 7.4) was used as running buffer and 10 mM HCl in HBS-EP buffer was used as regeneration buffer. The Ag-Ab binding is a reversible non-covalent interaction like electrostatic, hydrophobic and van der Waals forces. Use of high salt concentration, extremes of pH and detergents weakens this electrostatic interactions, or in other words, can regenerate the immobilized antibodies. Flagella monomer, the antigen of VHH CV90, was prepared in a matrix of 0.1% BSA in HBS-EP buffer. For measurements, the MRR chips were 'dipped' in 2 mL of solution for the indicated time span. For checking that immobilization was successful, i.e. the specific binding works, the chip was first blocked with 1% BSA after immobilization and introduced to antigen solutions and maximum 102pm shift was observed for 50μg/ml. The blocking of Abs with BSA ensured that non specific binding did not take place and the shift recorded is indeed for Ag-Ab binding. Next, to mimic non-specific binding, antigen (flagella monomer) was measured in a matrix of 0.1% BSA. These results are shown in Fig. 5.5 in the form of differential shift between the cuvettes. The corresponding subplot heading specifies the amount of antigen concentration measured. In all four subplots, point A denotes the injection of antigen in the running buffer, point B indicates that the MRR chip was then put back in the buffer solution only, and point C marks the disrupted Ag-Ab binding following the insertion in the regeneration buffer for 30 sec. The antigen showed specific binding to VHH CV90 and only background binding to VHH M180, which most likely resulted from unspecific adsorption of BSA. Clearly, the system can detect up to 0.02 μg/ml producing a total shift of 14.2 pm. But scaling down from 20 μg/ml to 0.02 μg/ml, does not give a linear relationship. It can be explained as the effect of non-specific binding getting stronger at lower concentration of the antigen. The sharp spikes at the measurand changing points are due to the dipping of the chip from one solution to another. From the algorithmic point of view, such spikes can drive the system towards adding or subtracting a fixed offset value resulting from the inability of the detection system to follow up with the signal. In Fig. 5.5(b), such a case is observable where the end point has a visible yet small amount of offset from the baseline. This might also result from the fact that the weak regeneration buffer could not completely wash of the BSA and the antigen from the chip surface. The conclusion that can be drawn from this measurement is the specific detection of flagella monomer with VHH CV90 could be observed using the MRR device along with the possibility of repeated antigen binding and regeneration of the chip. But the minimum detectable shift for the concentration change of the measurand was $\approx$ 15 pm and the problem with the baseline correction was dominant.

It was reported in the work of Heideman et al.[17] that the MRR chips can be realized for gas sensing in ambient atmosphere. Keeping this in mind, we tried to develop a gas sensor sensitive exclusively for CO_2. A specific chemical compound received from one of the partner organisation, termed *ionic liquid*, was said to serve the purpose of CO_2 testing in ambient atmosphere. The resolution limit of interest was to detect 2% CO_2. Upon receiving, an ionic fluid layer of approximately 3 μm was applied in the MRR sensing window. Initial results were not very promising since the layer appeared to be sensitive for CO_2, acetone and isopropyl alcohol (IPA) and the difference in shift of resonant peak was not significant enough to draw a definite conclusion. However, this liquid has a interesting response towards this gases comparing with Teflon layer. It was observed that Teflon is sensitive to the above mentioned gases too. As seen from Fig. 5.6, while the Teflon layer produces a positive shift, the ionic liquid layer shows a negative shift. Since the amount of shift respective to each other is not equal, the concept of reference ring can be applied in this situation. The implementation of reference ring calculation in the software is already discussed in Section. 3.2. Now a splitted MRR chip is functionalized

CO_2 *testing in ambient atmosphere*

with approximately 3μm thick ionic liquid layer in one sensing window and an equal thickness Teflon layer in the other window. For precise quantification of the concentration of gases, the chip was placed in an air-tight chamber integrated with two flow rate controllers. While one controller continuously provides a constant flow of either nitrogen or medical air, the other controls the measurand gas flow rate so that a desired amount of measurand gas concentration can be supplied in the chamber atmosphere.

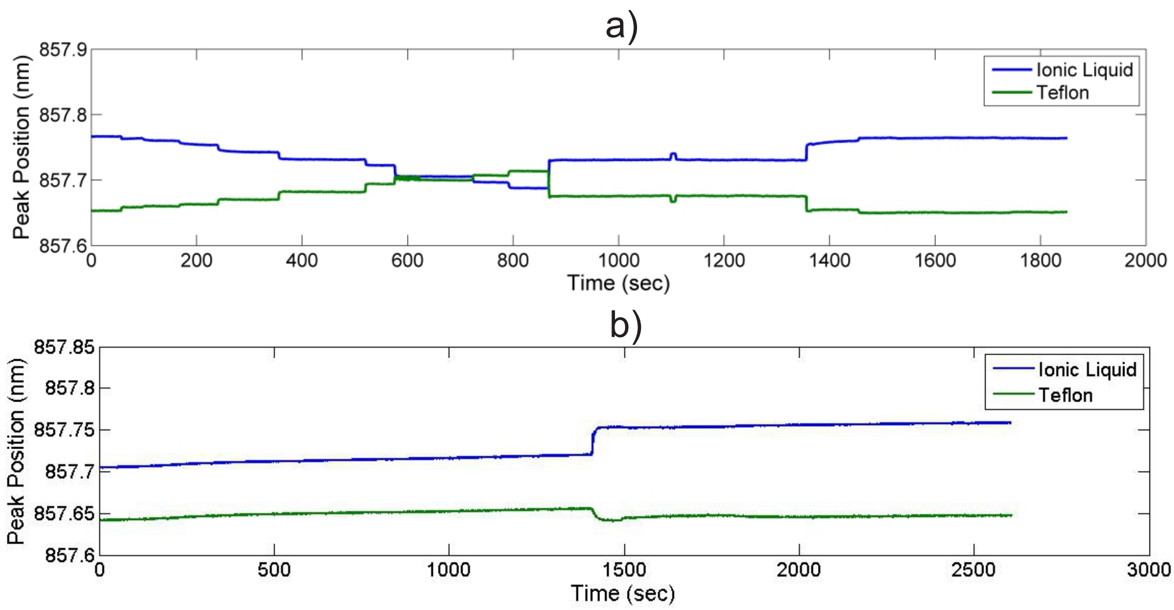

Figure 5.6: Resonance peak response of CO_2 sensor in presence of different concentration of gases - a) $N_2 - CO_2$ gas mixture; b) $N_2 - C_3H_6O$gas mixture

The result of this experiment is summarized in three plots in Fig. 5.7. Increasing the CO_2 concentration in $N_2 - CO_2$ gas mixture gives a downward staircase response till it reaches its minima for 100% CO_2. From there, the concentration was decreased straight to 44% and the curve experiences a sharp rise of 81.18 pm. After stabilizing, the N_2 flow rate was decreased from 4 ltr/min to 3 ltr/min keeping the concentration constant at 44%. The flow rate has no visible effect on the overall shift. Then concentration of CO_2 was gradually decreased to zero percent and the shift reaches its initial position. For a concentration change of zero to hundred percent, the shift changes by a factor of 1.397 per percentage concentration, approximated for a linear relationship between the concentration and resonance peak position. Switching the concentration value between zero to one percent of CO_2 produced 1.1, 1.1 and 1.5 pm respectively which is within ±15% of the estimated value. To compare the sensitivity of this sensor for acetone and isopropyl alcohol, experiments depicted in Fig. 5.7(b) and (c) were performed respectively. This sensor appears to be flow rate dependent for acetone among these three gases. For both CO_2 and isopropyl alcohol, shift was not dependent on flow rate. However, changing the flow rate from 0.2 ltr/min to 0.5 ltr/min produces a 2.4 pm upward shift exceeding the 0 ppm starting baseline. This phenomenon is associated with the two facts. First, the linear relationship between the differential pressure (ΔP), volumetric flow rate (Q) and absolute viscosity (η) is given by[59]

$$Q = K\frac{\Delta P}{\eta} \tag{5.1}$$

where, K is related to the geometry of restriction and is a constant factor. The viscosity of the gases are extremely low than liquids[60]. From the nomograph coefficients[60], the viscosity for IPA and 35% acetone at room temperature was calculated to be 2 and 1.6 centipoise (cP) respectively. Assuming same geometry of restriction on both cuvets and equal amount of flow rate, the differential pressure is higher for IPA than acetone. However, Teflon is known to be highly sensitive for acetone[17]. The differential pressure may induce a deformation in the Teflon tranducing layer, thus the refractive index change induced by the Teflon layer for acetone is higher than that of IPA. It can be observed from Fig. 5.6(b), although the shift in the Teflon layer is almost nullified by the opposite shift of ionic fluid but not completely; thereby resulting in a difference of 2.4 pm. Since, Teflon is not as sensitive for IPA as acetone, the opposite shifts induced in the two cuvets cancel out each other; whereas, for CO_2, no differential pressure arises from the change in volumetric flow rate and the MRR chip response is unaffected. As expected, the sensor is least sensitive for isopropyl alcohol. Producing a maximum shift of 6pm from the starting baseline, the sensor response is indifferent for concentrations less than 10 ppm. A 100 ppm concentration change in isopropyl alcohol corresponds to a shift of 2.1 pm whereas for acetone, equal amount of concentration change gives a shift of 3.51 pm.

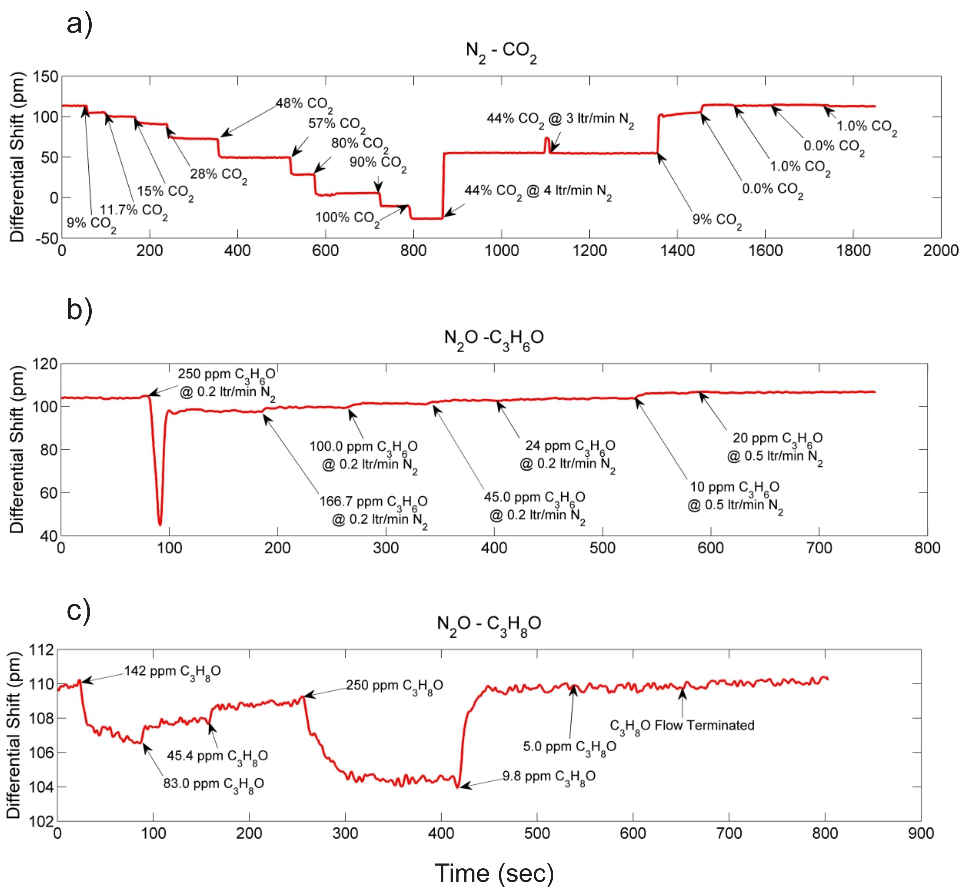

Figure 5.7: Results of gas sensing

Comparing with the results of VHH measurements, the signal read-out is improved significantly. The baseline problem is not visible for the CO_2 test. Also, the enhancement in the resolution limit with the implemented detection scheme allows to observe a shift as low as 1 pm.

5.4 SUMMARY

In this chapter, the evaluation of the system was done on the basis of the fit algorithm performance metrics and real-time sensing performance. In terms of performance metrics, the resolution limit of the detection algorithm improved from $\approx 0.1\mathrm{pm}$ as reported by Heideman et al.[17] to $\approx 0.04\,\mathrm{pm}$ by means of applying a better estimation to the drop response of the MRR chip. From the real-time sensing data, the system could differentiate between antigen concentration up to $0.02\,\mu\mathrm{g/ml}$. In terms of gas sensing, it is shown that the application of reference ring can be of great use for precision measurement. Detection of $\geqslant 1\,\mathrm{pm}$ shift for a change in CO_2 concentration from zero to one percent was possible. The comparative analysis with acetone and isopropyl alcohol showed clear distinction in response between the three gases.

6

CONCLUSION

This chapter concludes this thesis. First, an overview of the results is provided in Section 6.1 to succinctly summarise the findings and the system which has been developed in this research. Next, Section 6.2 provides the findings on the research question presented at the start of the thesis. Section 6.3 points out opportunities for future work. Finally, Section 6.4 finishes with general recommendations applicable to the MRR detection system architecture.

6.1 OVERVIEW OF RESULTS

After discussing the relevant theories, Chapter. 3 started with a design approach for the detection algorithm, and, subsequently, redundancies present in the mother application was optimized. New algorithms were proposed for the calculation of FSR, peak offset, and relative shift based on a reference channel response. A dramatic improvement in the FSR calculation has been observed. From a previous minimum of $40\,nm$ uncertainty in FSR calculation, the new algorithm shows a standard deviance of $1.299\,nm$ for the 35 sample calculations. The maximum resolution limit was observed for the oxide coated MRR chip.

Overview of Chapter. 3

Next, in Chapter. 4, the characterization data of two $850nm$ single mode VCSELs was presented. Alongside more precise characterization of $SS85-7U001P2$, linearization approximation was verified comparing the output of an asymmetric MZI and a further improvised linearization model was implemented. A better alternative for this VCSEL was found after the characterization of $ULM850-B2-PL-S0101U$, the sextic polynomial current to wavelength linearization of which was introduced in the mother application. The investigations on temperature stability issue not only resulted in a better understanding of the temperature control scheme, but also pointed out a possible defect in the MRR chip design. An attempt was made to quantify the effect of ambient temperature and evaporation of the liquid measurand from the chip surface. A reduction in shift by a factor of 10 and 2 was observed for closed system in terms of temperature and evaporation respectively.

Overview of Chapter. 4

Finally, in Chapter. 5, the parametric statistics of the fit is presented along with the detection efficacy of the MRR system both in liquid and gaseous medium. The asymptotic standard error of the fit is found to be $\sigma_y \leqslant 7 \times 10^{-5}$ for the application of median filter of rank 10 and fit range increment of 200 datapoints in addition to the FWHM estimation. The estimated computation time is $\approx 0.11 sec$ which is not less than the scan rate of $10Hz$, however, in practice, no lag between the measured data and fit data was observed. Comparing analogously with the result of the VHH measurement where the system could detect the presence of flagella monomer in a concentration as low as $0.02\,\mu g/ml$, the efficacy of the detection system for gas sensing in

Overview of Chapter. 5

ambient environment was measured for a chip with a special layer sensitive to the presence of carbon dioxide explicitly. An average shift of 1.1 pm was detected for a concentration of 1% CO_2.

To draw a conclusion, this system, now, allows for a measurement resolution limit of ≈ 0.04 pm, scanning resolution of 0.11 pm and a signal drift of ≈ 1 pm/h under temperature stabilized conditions.

6.2 FINDINGS ON RESEARCH QUESTION

This thesis centers around the primary research question which is given below.

> *Research Question (RQ): How to optimize the resonance peak detection limit of a micro ring resonator in terms of accuracy and precision utilizing mathematical programming without compromising cost and time?*

To find the answer to the question, fulfilling the meaning of the word *optimize* was kept in focus. In one hand, the most effective use of the resources was tried, while at the other, some of the parts of the software was rearranged and rewritten to improve the efficiency of the data processing. It was found that, at the current budget and scan rate, optimization of the system can be maximized by the application of an effective and robust fitting algorithm. For providing the algorithm with the closest approximant of the function parameters, physical system should be calibrated to provide the most stable operation. To summarize, the findings can be listed as follows:

PRIMARY FINDING
: A simple but robust, fast but computationally efficient numerical solution, with a stable convergence for minimizing a nonlinear function and suitable for handling the size of the data, can show a drastic accuracy improvement.

SECONDARY FINDING
: Ensuring the wavelength stability of the VCSEL results in an extended precision range of measurements.

TERTIARY FINDING
: Alongside nonlinear smoothers, a closed system approach significantly reduces the variance observed in data.

6.3 FUTURE WORK

Since the area of micro ring resonator detection system is still new, a lot of opportunities exist. The work of this thesis opens up a magnitude of new possibilities for improvement.

1. Alongside the real-time VCSEL current monitoring, the corresponding voltage measurement is implemented. Controlling the VCSEL temperature on basis of this driving voltage can ensure more precise control.

2. The fit function for the detection algorithm does not represent the characteristic behaviour of the MRR rather it is one of the best approximation. Implementation of fit function for the Lev-Mar optimization algorithm on basis of the drop port power transfer function will guarantee a more stable and accurate detection.

3. Micro ring resonators have a very small footprint of 100×100 micron. On chip integration of VCSEL will add an unique feature towards the realization of implantable chip.

4. A theoretical framework on basis of a suitable noise model was reported very recently[61], within which the detection limits of a spherical micro resonator based biosensor have been formally optimized. Integrating the noise model of their work with the existing algorithm for the purpose of denoising the signal can be explored.

5. It has been observed, in case of liquid sensing, that the change from one liquid medium to another introduces sharp fluctuations which can result in a complete wrong interpretation of the result and further compromising the accuracy and precision of the detection system. A microfluidics system can address this problem.

6.4 RECOMMENDATION

- For preventing the back reflection of light during gas sensing measurements, an angled input waveguide should be incorporated in lieu of the current straight input waveguide.
- In the light of complexities, it is recommended to avoid the use of DAQ internal amplification whenever possible. Amplification of a weak signal should be performed using the internal gain amplifiers of the corresponding channels.
- Currently OSROM implements selector switches that uses break before make strategy of switching which results in a deadtime in the detection system. The selection switches should be used prior to measurement, however, this problem can be addressed by implementing the strategy of make before break.

A

APPENDIX

A.1 COMPANY PROFILE - LIONIX B.V.

LioniX is a leading provider in co-development of products and manufacturing of components based on cutting-edge micro/nano technology for its (OEM) customers. LioniX offers design for manufacturing and horizontal integration by partnering with foundries, suppliers of complementary technologies and R&D institutes. Therefore, LioniX is able to offer complete solutions, and to control the process of development into production as well as the manufacturing of the final product. LioniX is being oriented towards emerging product-market combinations like optical components in Datacom, Telecom and instruments in Life Sciences, Industrial Process Control and Space. The combination of the core technology competences in integrated optics, micro/nano-fluidics and surface (nano)chemistry gives LioniX an unrivalled competence in the area of Lab-on-a-Chip applications, whereas the proprietary TriPleX^{TM} platform has a unique added value in Planar Lightwave Circuits which can also be combined with fluidics (optofluidics). LioniX distinguishes itself on an international scale in projects for multinationals, innovative SME's and start-up companies, as well as for universities/institutes and leading end-users.

- Integrated Optics: devices are based on the proprietary TriPleX^{TM} (Si_3N_4/SiO_2) technology, which enables UV-VIS-(N)IR transparent waveguides for data/ telecom applications, optical detectors, sensors and signal processing.
- Microfluidics: components and system engineering for (bio)sensor, Lab-on-a-Chip and flow chemistry Technology applications, including integrated optics.
- Optofluidics: the unique combination between the TriPleX^{TM} and microfluidics technology enables a further integration of sensors in Lab-on-a-chip and flow chemistry.
- Surface Functionalization: the rational design of functional surfaces, i.e. for immobilization of receptors and catalysts, supported by innovative mesoscale modelling techniques.
- Micro/Nano Technology / MEMS: thin films, structures and components based on numerous process steps developed in the MESA+ NanoLab, including LioniX's specialities such as DRIE of glasses, Fused Silica wafer bonding and Chemical-Mechanical Polishing (CMP).

LioniX is a private company, founded in 2001 and located at the Business and Science Park in Enschede, the Netherlands. It employs over 25 highly educated people, and its management has experience in the micro/nano technology for decades.

A.2 AUTOMATION IN VCSEL CHARACTERIZATION

It is worthy of mentioning that the acquisition of the characterization data of SS85 − 7U001P2 took almost 80 hours. Apart from being time-consuming, the process is exhaustive and prone to systematic error. For the characterization of ULM850 − B2 − PL − S0101U, an automated system was designed and implemented to characterize the laser after initiation. Fig.A.1 represents the schematics of such system. Using the datasheet of OSA, a driver was written for it and implemented inside the mother program. The GPIB port of the OSA was connected to the PC via a GPIB-USB cable making it a VISA instrument. On the contrary, a DAQ, connected to the PC via USB as well, drives the OSROM, thus VCSEL, and is detected as DAQmx instrument. Since there is no conflict in driving both these instruments simultaneously, an automated system is viable. The specifications of this characterization process can be found in Table. 4.1. At these set values, it took the system, to sweep four complete spectrum and save the data, approximately 36 hours.

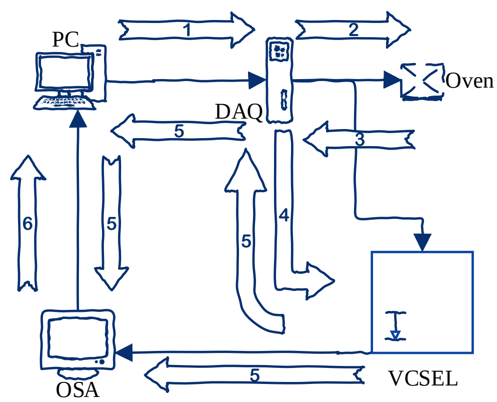

Figure A.1: Schematic representation of the automated system for VCSEL characterization. End to end straight arrows represent physical connections, whereas the notched arrows denote the process flow.

A.3 MATLAB CODES

```
% Levenberg-Marquardt test For MicroRing Resonator

%   Hasib Mustafa, M-EE, Universiteit Twente for LioniX BV as part of
%   Master Thesis

clear all; close all; clc;
hold off

%randn('seed',0); % specify a particular random sequence for msmnt error

%epsPlots = 0;  formatPlot(epsPlots);   % 1: make .eps plots, 0: don't


global  function_number

function_number = 1;        % which function to run.
                                  %#1-Lorentzian
                                  %#2-Gaussian
                                  %#3-Characteristic

consts = [ ];                         % optional vector of constants

% for j=1:1:4

Npnt = 10000;         % number of data points
factor=200;%[0 200 500];
selection=1;
%{
if j==4
    selection=0;
end
%}
%
filename2read='C:\Users\Reckoner\Documents\Study\Master Thesis\Measurements\Algorithm
    check\35c_v11_samples.xlsx';
sheet4sample='3';
sheet2write='1';
sheet4response='1';
start_range_all=2;
% datapoints2read=9999;
end_range_all=10001;
num_data_set=1;
y_offset=0;                   % Offset Y

%
%%Current to Wavelength Linearization
Irange_all=['A' num2str(start_range_all) ':A' num2str(end_range_all) ''];
I_all=xlsread(filename2read, sheet4sample, Irange_all);
% X=0.0227.*I.^2+0.0514.*I+850.824+(20*0.1078);               %OLD Current-wavelength
    Fit
```

```
% X_all=-0.0104.*I_all.^3+0.1244.*I_all.^2-0.2585.*I_all+855.34+20*0.1078;     %NEW
    Current-wavelength Fit
%}
Yrange_all=['B' num2str(start_range_all) ':AJ' num2str(end_range_all) ''];
Y_all=xlsread(filename2read, sheet4sample, Yrange_all);

%{
for i=1:1:num_data_set

    %Individual data set range
    strng=start_range_all+((i-1)*Npnt);
    endrng=(start_range_all+(i*Npnt))-2;

    %Boundary
    llt=strng;      %Left Lower Threshold
    rut=endrng;     %Right Upper Threshold
    twort=endrng;     %2 Right Threshold
    lur=llt+6526;   %Left Upper Range
    lut=llt+6248;   %Left Upper Threshold
    rlr=llt+3469;   %Right Lower Range
    rlt=llt+3711;   %Right Lower Threshold

    X_data=X_all(strng:endrng);
    Y_data=Y_all(strng:endrng);

    X_dataleft=X_all(llt:lur);
    X_dataright=X_all(rlr:rut);
    Y_dataleft=Y_all(llt:lur);
    Y_dataright=Y_all(rlr:rut);

    C=abs(find(Y_data>=0.48*max(Y_data) & Y_data<=0.52*max(Y_data)));
    ind11=median(C(1:length(C)/2));
    ind22=find(Y_data==max(Y_data));
    fwhm=2*abs(ind22-ind11);


end
%}
%
my_data=load('sample35');
t_column=1;
y_column=2:1:36;
%

for i=1:1:1
y_data = my_data.sample35(:,y_column(i));
% y_data=Y_all(:,y_column(i));
y_dat = y_data(:);
y_dat=medfilt1(y_dat,10);
i_init=my_data.sample35(:, t_column);
% i_init=I_all;
t_init=-0.0104.*i_init.^3+0.1244.*i_init.^2-0.2585.*i_init+855.34+20*0.1078;     %Poly 3
     fit for OPTOWELL
t_init=t_init(:);
```

```
if function_number==1 || 2
    t = my_data.sample35(:, t_column);
%     t = i_init;
    t = t*ones(1, length(y_column));
    t = t(:);
end
if function_number==3
     y_dat_ht=hilbert(y_dat);
%      THETA=atan2(y_dat_ht, y_dat);
     t=unwrap(angle(y_dat_ht));
     t=t(:);
end

%{
for i=1:1:35
   y_dat1=y_data(:,i);
    C=abs(find(y_dat1>=0.48*max(y_data(:,i)) & y_dat1<=0.52*max(y_data(:,i))));
    ind11(i)=median(C(1:length(C)/2));
    ind22(i)=find(y_dat1(i)==max(y_dat1(i)));
    fwhm(i)=2*abs(ind22(i)-ind11(i));
    max_ydat(i)=max(y_dat1);
end
%}
%{
param1=mean(ind22);
param2=mean(fwhm)/2;
param3=mean(max_ydat);
%}
C=abs(find(y_dat>=0.48*max(y_dat) & y_dat<=0.52*max(y_dat)));
    ind11=round(median(C(1:length(C)/2)));
    ind22=find(y_dat==max(y_dat));
    fwhm=2*abs(ind22-ind11);

if function_number==1
    param1=find(y_dat==max(y_dat));
    param2=fwhm/2;
    param3=max(y_dat);

        if selection==1
            y_dat=y_dat(param1(1)-(param2(1)+factor):param1(1)+(param2(1)+factor)-1);
            t=t(param1(1)-(param2(1)+factor):param1(1)+(param2(1)+factor)-1);
            param1_init=find(y_dat==max(y_dat));
            param2_init=fwhm/2;
            param3_init=max(y_dat);
        end
        if selection==0
            param1_init=param1;
            param2_init=param2;
            param3_init=param3;
        end
end

if function_number==2
    param1=max(y_dat);
```

```
    param2=find(y_dat==max(y_dat));
    param3=fwhm;

        if selection==1
            y_dat=y_dat(param2(1)-(param3(1)/2+factor):param2(1)+(param3(1)/2+factor)-1);
            t=t(param2(1)-(param3(1)/2+factor):param2(1)+(param3(1)/2+factor)-1);
            param1_init=max(y_dat);
            param2_init=find(y_dat==max(y_dat));
            param3_init=fwhm/2;
        end
        if selection==0
            param1_init=param1;
            param2_init=param2;
            param3_init=param3;
        end
end

if function_number==3
    lambda_0=850;  %vaccum wavelength in nm
    lambda_fwhm=2*abs(i_init(ind22)-i_init(ind11)); %fwhm in nm
    fsr=0.450;  %Free spectral range in nm
    param1=max(y_dat);
    param2=1/(sin((pi*lambda_fwhm(1))/(2*fsr)));
%     param2=(2*fsr/(pi*lambda_fwhm(1)));
        if selection==1
            side_ext=fwhm/2;
            max_ind=find(y_dat==max(y_dat));
            y_dat=y_dat(max_ind(1)-(side_ext(1)+factor):max_ind(1)+(side_ext(1)+factor)-1);
            t=t(max_ind(1)-(side_ext(1)+factor):max_ind(1)+(side_ext(1)+factor)-1);
            param1_init=y_dat(y_dat==max(y_dat));
            param2_init=param2;
        end
        if selection==0
            param1_init=param1;
            param2_init=param2;
        end
end
% % Y_all=Y_all(:);
% t_all=X_all*ones(1,35); %length(y_column)=35
%
% % y_dat1 = reshape(Y_data.',1,[]);
% % t1 = reshape(X_data.',1,[]);
%
%
%
% y_dat=y_dat1(ind22-(fwhm/2):ind22+(fwhm/2)-1);
% t=t_all(ind22-(fwhm/2):ind22+(fwhm/2)-1);
%
% y_dat=y_dat(:);
% t=t(:);
```

```
% param1=find(y_dat==max(y_dat));
% param2=fwhm/2;
% param3=max(y_dat);
% t = [1:Npnt]';          % independent variable
% true value of parameters ...
if function_number == 1, p_true  = [ param1(1)   param2(1) param3(1)]'; end % param1=x_c
    ; param2=gamma; param3=I
if function_number == 2, p_true  = [ param1(1)   param2(1) param3(1) ]'; end           %
     param1=peak amp; param2=peak position; param3=fwhm
if function_number == 3, p_true  = [  param1(1)   param2(1) ]'; end          %param1=H;
    param2=F_c

% Y_data = lm_func(t,p_true,consts);

%{
% x2=zeros(fwhm/2);
% range of values for basic paramter search
p1 = 0.1*p_true(1):0.2*p_true(1):2*p_true(1);
p2 = 0.1*p_true(2):0.2*p_true(2):2*p_true(2);
p3 = 0.1*p_true(3):0.2*p_true(3):2*p_true(3);
% p4 = 0.1*p_true(4):0.2*p_true(4):2*p_true(4);
%
% parameter search
for ip2 = 1:length(p2);
            for ip3 = 1:length(p3);
                pt = [ p_true(1)  p2(ip2) p3(ip3) ];
                delta_y = ( y_dat - lm_func(t,pt,consts) );
                X2(ip2,ip3)= (delta_y' * delta_y)/2;

            end

end
%
figure(1); % ------------ plot shape of Chi-squared objective function
 clf
 mesh(p2,p3,log10(X2))
  xlabel('p_2')
  ylabel('p_3')
  zlabel('log_{10}(\chi^2)')
%}
% initial guess parameters  ...
if function_number == 1, p_init  = [ param1_init(1)   param2_init(1)  param3_init(1) ]';
      end
if function_number == 2, p_init  = [  param1_init(1)   param2_init(1)  param3_init(1)
    ]';  end
if function_number == 3, p_init  = [ param1_init(1)   param2_init(1) ]';  end

weight = Npnt/sqrt(y_dat'*y_dat);   % sqrt of sum of data squared
% weight =1;
if function_number == 1
p_min = [ param1_init(1)-50 param2_init(1)-100 0.5*param3_init(1)];
p_max =  [ param1_init(1)+50 param2_init(1)+100 1.2*param3_init(1)];
end
```

```
if function_number == 2
p_min = [ 0.5*param1_init(1) param2_init(1)-50 param3_init(1)-100 ];
p_max = [ 1.2*param1_init(1) param2_init(1)+50 param3_init(1)+100 ];
end
if function_number == 3
p_min = [ 0.5*param1_init(1) param2_init(1)-1000 ];
p_max = [ 1.2*param1_init(1) param2_init(1)+1000 ];
end
% Algorithmic Parameters
%         prnt MaxIter  eps1  eps2  epx3  eps4  lam0  lamUP lamDN UpdateType
   opts = [  3,    200, 1e-3, 1e-6, 1e-4, 1e-2, 1e-3,    10,    4,        1 ];

[p_fit,Chi_sq,sigma_p,sigma_y,corr,R2,cvg_hst] = lm('lm_func',p_init,t,y_dat,1,-0.01,
    p_min,p_max,consts,opts);
%
y_fit = lm_func(t,p_fit,consts);
%
disp('    initial    true       fit        sigma_p percent')
disp(' -------------------------------------------------------')
disp ([ p_init  p_true  p_fit sigma_p 100*abs(sigma_p./p_fit) ])
%
n = length(p_fit);

lm_plots ( n, t, y_dat, y_fit, sigma_y, cvg_hst );
%}
%Data saving in Excel
%{
range1=['k' num2str(i)];
range2=['l' num2str(i)];
xlswrite(filename2read, Chi_sq, sheet2write, range1)
xlswrite(filename2read, R2, sheet2write, range2)
%}
end

%{
y_dat = y_dat(:);
y_fit = y_fit(:);
figure(1); % ------------ plot shape of Chi-squared objective function

 if j==1; k=[1 2 3]; end
 if j==2; k=[4 5 6]; end
 if j==3; k=[7 8 9]; end
 if j==4; k=[10 11 12]; end

 subplot(4,3,k(1))
  hold on
   semilogy(t,sigma_y,'-r','linewidth',4);
    xlabel('t'); ylabel('\sigma_y(t)')
 subplot(4,3,k(2))
 mesh(p2,p3,log10(X2))
  xlabel('p_2')
  ylabel('p_3')
  zlabel('log_{10}(\chi^2)')
subplot(4,3,k(3))
```

```
hist(y_dat - y_fit)
  title('histogram of residuals')
  axis('tight'); xlabel('y_{data} - y_{fit}'); ylabel('count')
%}

 %{
  if j==2;
 subplot(434)
  hold on
   semilogy(t,sigma_y,'-r','linewidth',4);
    xlabel('t'); ylabel('\sigma_y(t)')
 subplot(435)
 mesh(p2,p3,log10(X2))
  xlabel('p_2')
  ylabel('p_3')
  zlabel('log_{10}(\chi^2)')
subplot(436)
hist(y_dat - y_fit)
  title('histogram of residuals')
  axis('tight'); xlabel('y_{data} - y_{fit}'); ylabel('count')
  end

   if j==3;
 subplot(437)
  hold on
   semilogy(t,sigma_y,'-r','linewidth',4);
    xlabel('t'); ylabel('\sigma_y(t)')
 subplot(438)
 mesh(p2,p3,log10(X2))
  xlabel('p_2')
  ylabel('p_3')
  zlabel('log_{10}(\chi^2)')
subplot(439)
hist(y_dat - y_fit)
  title('histogram of residuals')
  axis('tight'); xlabel('y_{data} - y_{fit}'); ylabel('count')
   end
 %
    if j==4;
 subplot(4,3,10)
  hold on
   semilogy(t,sigma_y,'-r','linewidth',4);
    xlabel('t'); ylabel('\sigma_y(t)')
 subplot(4,3,11)
 mesh(p2,p3,log10(X2))
  xlabel('p_2')
  ylabel('p_3')
  zlabel('log_{10}(\chi^2)')
subplot(4,3,12)
hist(y_dat - y_fit)
  title('histogram of residuals')
  axis('tight'); xlabel('y_{data} - y_{fit}'); ylabel('count')
    end
   %}
```

```
% end

function y_hat = lm_func(t,p,c)
% y_hat = lm_func(t,p,c)
%
% -------- INPUT VARIABLES ---------
%  t     = m-vector of independent variable values (assumed to be error-free)
%  p     = n-vector of parameter values , n = 4 in these examples
%  c     = optional vector of other constants
%
% ---------- OUTPUT VARIABLES -------
% y_hat  = m-vector of the curve-fit function evaluated at points t and
%          with parameters p


global function_number

%  Lorentzian
if function_number == 1
    a=1:1:length(t);
    a=a(:);
    y_hat = p(3).*(1./(((a-p(1))./p(2)).^2+1));
end

%  Gaussian
if function_number == 2
    a=1:1:length(t);
    a=a(:);
   y_hat = p(1).*exp(-((a-p(2))./p(3)).^2);
end

% Characteristic
if function_number == 3
   y_hat = p(1)./(1+(p(2).*(sin(t./2)).^2));
end

% LM_FUNC ------------------------------------

function [p,X2,sigma_p,sigma_y,corr,R_sq,cvg_hst] = lm(func,p,t,y_dat,weight,dp,p_min,p_max,c,opts)
% [p,X2,sigma_p,sigma_y,corr,R_sq,cvg_hst] = lm(func,p,t,y_dat,weight,dp,p_min,p_max,c,opts)
%
% Levenberg Marquardt curve-fitting: minimize sum of weighted squared residuals
% ----------  INPUT  VARIABLES  -----------
% func   = function of n independent variables, 't', and m parameters, 'p',
%          returning the simulated model: y_hat = func(t,p,c)
% p      = n-vector of initial guess of parameter values
% t      = m-vectors or matrix of independent variables (used as arg to func)
% y_dat  = m-vectors or matrix of data to be fit by func(t,p)
% weight = weighting vector for least squares fit ( weight >= 0 ) ...
%          inverse of the standard measurement errors
%          Default:  sqrt(d.o.f. / ( y_dat' * y_dat ))
% dp     = fractional increment of 'p' for numerical derivatives
```

```
%          dp(j)>0 central differences calculated
%          dp(j)<0 one sided 'backwards' differences calculated
%          dp(j)=0 sets corresponding partials to zero; i.e. holds p(j) fixed
%          Default:  0.001;
% p_min  = n-vector of lower bounds for parameter values
% p_max  = n-vector of upper bounds for parameter values
% c      = an optional matrix of values passed to func(t,p,c)
% opts   = vector of algorithmic parameters
%             parameter    defaults    meaning
% opts(1)  =  prnt            3        >1 intermediate results; >2 plots
% opts(2)  =  MaxIter      10*Npar     maximum number of iterations
% opts(3)  =  epsilon_1       1e-3     convergence tolerance for gradient
% opts(4)  =  epsilon_2       1e-3     convergence tolerance for parameters
% opts(5)  =  epsilon_3       1e-3     convergence tolerance for Chi-square
% opts(6)  =  epsilon_4       1e-2     determines acceptance of a L-M step
% opts(7)  =  lambda_0        1e-2     initial value of L-M paramter
% opts(8)  =  lambda_UP_fac   11       factor for increasing lambda
% opts(9)  =  lambda_DN_fac    9       factor for decreasing lambda
% opts(10) =  Update_Type      1       1: Levenberg-Marquardt lambda update
%                                      2: Quadratic update
%                                      3: Nielsen's lambda update equations
%
% ----------  OUTPUT  VARIABLES  -----------
% p       = least-squares optimal estimate of the parameter values
% X2      = Chi squared criteria
% sigma_p = asymptotic standard error of the parameters
% sigma_y = asymptotic standard error of the curve-fit
% corr    = correlation matrix of the parameters
% R_sq    = R-squared cofficient of multiple determination
% cvg_hst = convergence history

%   modified from: "The Levenberg-Marquardt method for nonlinear least
%   squares curve-fitting problems"
%   by Henri Gavin, Dept. Civil & Environ. Engineering, Duke Univ. November 2005
```

A.4 PHYSICAL CONSTANTS

NAME	SYMBOL	VALUE	UNIT
Number π	π	3.14159265358979323846	
Number e	e	2.71828182845904523536	
Euler's constant	$\gamma = \lim_{n\to\infty}\left(\sum_{k=1}^{n} 1/k - \ln(n)\right) = 0.5772156649$		
Elementary charge	e	$1.60217733 \cdot 10^{-19}$	C
Speed of light in vacuum	c	$2.99792458 \cdot 10^{8}$	m/s (def)
Permittivity of the vacuum	ε_0	$8.854187 \cdot 10^{-12}$	F/m
Permeability of the vacuum	μ_0	$4\pi \cdot 10^{-7}$	H/m
$(4\pi\varepsilon_0)^{-1}$		$8.9876 \cdot 10^{9}$	Nm^2C^{-2}
Planck's constant	h	$6.6260755 \cdot 10^{-34}$	Js
Dirac's constant	$\hbar = h/2\pi$	$1.0545727 \cdot 10^{-34}$	Js
Stefan-Boltzmann's constant	σ	$5.67032 \cdot 10^{-8}$	$Wm^{-2}K^{-4}$
Wien's constant	k_W	$2.8978 \cdot 10^{-3}$	mK
Molar gas constant	R	8.31441	$J \cdot mol^{-1} \cdot K^{-1}$
Avogadro's constant	N_A	$6.0221367 \cdot 10^{23}$	mol^{-1}
Boltzmann's constant	$k = R/N_A$	$1.380658 \cdot 10^{-23}$	J/K
Electron mass	m_e	$9.1093897 \cdot 10^{-31}$	kg

BIBLIOGRAPHY

1. Ramaier Narayanaswamy and Otto S Wolfbeis. *Optical sensors: industrial, environmental and diagnostic applications*, volume 1. Springer, 2004.

2. Colette McDonagh, Conor S Burke, and Brian D MacCraith. Optical chemical sensors. *Chemical reviews*, 108(2):400–422, 2008.

3. Xudong Fan, Ian M White, Siyka I Shopova, Hongying Zhu, Jonathan D Suter, and Yuze Sun. Sensitive optical biosensors for unlabeled targets: A review. *analytica chimica acta*, 620 (1):8–26, 2008.

4. M Granada P André P Antunes, F Domingues. Mechanical properties of optical fibers. *Selected Topics on Optical Fiber Technology*, 2011.

5. H. J. W. M. Hoekstra P.V. Lambeck. *Optical chemical sensors*, volume 224, chapter Planar Waveguiding Systems for Optical Sensing, pages 261–280. Springer, 2006.

6. Conor S Burke, Ondrej Stránik, Helen M McEvoy, and Brian D MacCraith. Planar optical sensors and evanescent wave effects. In *Optical Chemical Sensors*, pages 193–215. Springer, 2006.

7. L Lechuga D Duval. 2012 breakthroughs in lab-on-a-chip & optical biosensors. *IEEE Photonics Journal*, 2013.

8. Paul V Lambeck, Hugo JWM Hoekstra, Joris Van Lith, and Gijs Van Elzakker. Two novel integrated optical sensor types for measuring chemical concentrations, based on chemically induced changes of modal field profiles. *Journal of Nonlinear Optical Physics & Materials*, 13 (02):209–227, 2004.

9. Paul V Lambeck, Joris Van Lith, and Hugo JWM Hoekstra. Three novel integrated optical sensing structures for the chemical domain. *Sensors and Actuators B: Chemical*, 113(2):718–729, 2006.

10. RG Heideman, RPH Kooyman, and J Greve. Performance of a highly sensitive optical waveguide mach-zehnder interferometer immunosensor. *Sensors and Actuators B: Chemical*, 10(3):209–217, 1993.

11. Mikhail L Gorodetsky, Anatoly A Savchenkov, and Vladimir S Ilchenko. Ultimate q of optical microsphere resonators. *Optics Letters*, 21(7):453–455, 1996.

12. E Krioukov, DJW Klunder, A Driessen, J Greve, and C Otto. Sensor based on an integrated optical microcavity. *Optics letters*, 27(7):512–514, 2002.

13. Jacob T Robinson, Long Chen, and Michal Lipson. On-chip gas detection in silicon optical microcavities. *Optics Express*, 16(6):4296–4301, 2008.

14. Yuze Sun and Xudong Fan. Optical ring resonators for biochemical and chemical sensing. *Analytical and bioanalytical chemistry*, 399(1):205–211, 2011.

15. Mario Iodice, Luca De Stefano, Giuseppe Coppola, Vito Mocella, Ilaria Rea, Edoardo De Tommasi, Emanuele Orabona, and Ivo Rendina. Label-free biosensing by means of optical micro-ring resonator. In *SPIE Europe Optics+ Optoelectronics*, pages 735603–735603. International Society for Optics and Photonics, 2009.

16. Ayca Yalcin, Ketul C Popat, John C Aldridge, Tejal A Desai, John Hryniewicz, Nabil Chbouki, Brent E Little, Oliver King, Vien Van, Sai Chu, et al. Optical sensing of biomolecules using microring resonators. *Selected Topics in Quantum Electronics, IEEE Journal of*, 12(1):148–155, 2006.

17. Rene Heideman, Marcel Hoekman, and Erik Schreuder. Triplex-based integrated optical ring resonators for lab-on-a-chip and environmental detection. *Selected Topics in Quantum Electronics, IEEE Journal of*, 18(5):1583–1596, 2012.

18. Xiaoguang Tu, Junfeng Song, Tsung-Yang Liow, Mi Kyoung Park, Jessie Quah Yiying, Jack Sheng Kee, Mingbin Yu, and Guo-Qiang Lo. Thermal independent silicon-nitride slot waveguide biosensor with high sensitivity. *Optics express*, 20(3):2640–2648, 2012.

19. H. Hoekstra P. V. Lambeck. Integrated optical sensors. In *Lasers and Electro-Optics Society, 2003. LEOS 2003. The 16th Annual Meeting of the IEEE*, volume 2, pages 967–968, 2003.

20. RG Heideman and PV Lambeck. Remote opto-chemical sensing with extreme sensitivity: design, fabrication and performance of a pigtailed integrated optical phase-modulated mach–zehnder interferometer system. *Sensors and Actuators B: Chemical*, 61(1):100–127, 1999.

21. Jose MF Moura. What is signal processing?[president's message]. *Signal Processing Magazine, IEEE*, 26(6):6–6, 2009.

22. Louis L Scharf. *Statistical signal processing*, volume 98. Addison-Wesley Reading, MA, 1991.

23. Edwin Jan Klein. *Densely integrated microring-resonator based components for fiber-to-the-home applications*. PhD thesis, University of Twente, 2007.

24. Tom Claes, Wim Bogaerts, and Peter Bienstman. Experimental characterization of a silicon photonic biosensor consisting of two cascaded ring resonators based on the vernier-effect and introduction of a curve fitting method for an improved detection limit. *Optics express*, 18(22):22747–22761, 2010.

25. Tom Claes, Wim Bogaerts, and Peter Bienstman. Vernier-cascade silicon photonic label-free biosensor with very large sensitivity and low-cost interrogation. In *SPIE NanoScience+ Engineering*, pages 80990R–80990R. International Society for Optics and Photonics, 2011.

26. Gordon K Smyth. Nonlinear regression. *Encyclopedia of environmetrics*, 2002.

27. Henri P. Gavin. The levenberg-marquardt method for nonlinear least squares curve-fitting problems. Technical report, Duke University, September, 24 2013.

28. Morris L Marx and Richard J Larsen. *Introduction to mathematical statistics and its applications*. Pearson/Prentice Hall, 2006.

29. Ananth Ranganathan. The levenberg-marquardt algorithm, 2004.

30. Hao Yu and BM Wilamowski. Levenberg-marquardt training. *The Industrial Electronics Handbook*, 5:1–15, 2011.

31. Steven C Chapra and Raymond P Canale. *Numerical methods for engineers*. McGraw-Hill Higher Education New York, 2010.

32. MR Osborne. Fisher's method of scoring. *International Statistical Review*, pages 99–117, 1992.

33. Mircea Petrache. Meaning of the hessian of a function in a critical point. Technical report, ETH Zurich, February 2012.

34. Donald W Marquardt. An algorithm for least-squares estimation of nonlinear parameters. *Journal of the Society for Industrial & Applied Mathematics*, 11(2):431–441, 1963.

35. Richard Poisel. *Electronic warfare target location methods*. Artech House, 2012.

36. Anders Larsson. Advances in vcsels for communication and sensing. *Selected Topics in Quantum Electronics, IEEE Journal of*, 17(6):1552–1567, 2011.

37. Rainer Michalzik and Karl Joachim Ebeling. Operating principles of vcsels. In *Vertical-Cavity Surface-Emitting Laser Devices*, pages 53–98. Springer, 2003.

38. Rongqing Hui and Maurice O'Sullivan. *Fiber optic measurement techniques*. Academic Press, 2009.

39. Akihiro Takagi, Kaname Jinguji, and Masao Kawachi. Silica-based waveguide-type wavelength-insensitive couplers (winc's) with series-tapered coupling structure. *Lightwave Technology, Journal of*, 10(12):1814–1824, 1992.

40. Dominik G Rabus. Ring resonators: Theory and modeling. *Integrated Ring Resonators: The Compendium*, pages 3–40, 2007.

41. BEA Saleh MC Teich. *Fundamentals of photonics*. Wiley Interscience, 1991.

42. André Delâge, Dan-Xia Xu, Ross W McKinnon, Edith Post, Philip Waldron, Jean Lapointe, Craig Storey, Adam Densmore, Siegfried Janz, Boris Lamontagne, et al. Wavelength-dependent model of a ring resonator sensor excited by a directional coupler. *Journal of Lightwave Technology*, 27(9):1172–1180, 2009.

43. Lorenzo Pavesi and David J Lockwood. *Silicon photonics*, volume 1. Springer, 2004.

44. Rüdiger Paschotta. *Encyclopedia of laser physics and technology*, volume 1. Wiley-vch Berlin, 2008.

45. Horst Zimmermann. *Integrated silicon optoelectronics*, volume 3. Springer, 2000.

46. Jacob Millman and Christos C Halkias. *Electronic devices and circuits*. McGraw-Hill, 1967.

47. John W Webb and Ronald A Reis. *Programmable logic controllers: principles and applications*. Prentice Hall PTR, 1998.

48. Philip R Bevington and D Keith Robinson. *Data reduction and error analysis for the physical sciences*, volume 336. McGraw-Hill New York, 1969.

49. GAF Seber and CJ Wild. *Nonlinear regression*. Wiley, New York, 1989.

50. Andrew R Barron. *Self-Organizing Methods in Modeling: GMDH Type Algorithms*, chapter Predicted squared error: a criterion for automatic model selection, pages 87–103. Marcel Dekker, 1984.

51. Graham Clifford Goodwin, Stefan F Graebe, and Mario E Salgado. *Control system design*, volume 240. Prentice Hall New Jersey, 2001.

52. George Ellis. *Control system design guide: using your computer to understand and diagnose feedback controllers*. Butterworth-Heinemann, 2012.

53. Gonzalo R Arce. *Nonlinear signal processing: a statistical approach*. John Wiley & Sons, 2005.

54. Labview system design software. Website, last accessed, December 2013. URL `http://www.ni.com/labview/`.

55. Hasib Mustafa. Development of the peak detection algorithm of micro ring resonators. Internship report, Universiteit Twente, 2013.

56. The engineering toolbox. Website, Last accessed, February 2014. URL `http://www.engineeringtoolbox.com/`.

57. Charles A Janeway, Paul Travers, Mark Walport, and J Donald Capra. *Immunobiology: the immune system in health and disease*, volume 2. Churchill Livingstone, 2001.

58. Dirk Saerens, Lieven Huang, Kristien Bonroy, and Serge Muyldermans. Antibody fragments as probe in biosensor development. *Sensors*, 8(8):4669–4686, 2008.

59. *Agilent Precision Gas Flow Meter*. Agilent Technologies, 2 edition, November 2009.

60. Roger Gilmont. Liquid viscosity correlations for flowmeter calculations. *Chemical engineering progress*, 98(10):36–41, 2002.

61. Matthew R Foreman, Wei-Liang Jin, and Frank Vollmer. Optimizing detection limits in whispering gallery mode biosensing. *Optics express*, 22(5):5491–5511, 2014.